ENVIRONMENTALLY RELEVANT ADSORPTION ON CARBONACEOUS SURFACES STUDIED BY OPTICAL DIFFERENTIAL REFLECTANCE AND TEMPERATURE PROGRAMMED DESORPTION

by

SeokJoon Kwon

B.S. in Civil Engineering, Hanyang University, 1996

M.S. in Civil and Environmental Engineering, University of Pittsburgh, 1999

Submitted to the Graduate Faculty of

School of Engineering in partial fulfillment

of the requirements for the degree of

Doctor of Philosophy

University of Pittsburgh

2002

UNIVERSITY OF PITTSBURGH

SCHOOL OF ENGINEERING

This dissertation was presented

by

Seokjoon Kwon

It was defended on

May 9, 2002

and approved by

Eric Borguet, Assistant Professor, Department of Chemistry

Leonard W. Casson, Associate Professor, Department of Civil and Environmental Engineering

J. Karl Johnson, Associate Professor, Department of Chemical Engineering

Ronald D. Neufeld, Professor, Department of Civil and Environmental Engineering

Dissertation Director: Radisav D. Vidic, Associate Professor, Department of Civil and Environmental Engineering

ABSTRACT

ENVIRONMENTALLY RELEVANT ADSORPTION ON CARBONACEOUS SURFACES STUDIED BY OPTICAL DIFFERENTIAL REFLECTANCE AND TEMPERATURE PROGRAMMED DESORPTION

Seokjoon Kwon, Ph.D.

University of Pittsburgh, 2002

This study evaluated the application of a versatile optical technique to study the adsorption and desorption of model adsorbates representative of volatile polar (acetone) and non-polar (propane) organic compounds on a model carbonaceous surface under ultra high vacuum (UHV) conditions. The results showed the strong correlation between optical differential reflectance (ODR) and adsorbate coverage determined by temperature programmed desorption (TPD). The ODR technique was found to be a powerful tool to investigate surface adsorption and desorption from UHV to high pressure conditions.

The effects of chemical functionality and surface morphology on the adsorption/desorption behavior of acetone, propane and mercury were investigated for two model carbonaceous surfaces, namely air-cleaved highly oriented pyrolytic graphite (HOPG) and plasma-oxidized HOPG. Oxygen-containing functional groups exist on both air-cleaved and plasma-oxidized HOPG. They can be removed by thermal treatment (> 500 K). The presence of these groups almost completely suppresses propane adsorption at 90 K and removal of these groups leads to a dramatic increase in adsorption capacity. The amount of acetone adsorbed is independent of surface heat treatment and depends only on total exposure. The effect of

morphological heterogeneity is evident for plasma-oxidized HOPG as this substrate provides greater surface area, as well as higher energy binding sites. Mercury adsorption at 100 K on HOPG surfaces with and without chemical functionalities and topological heterogeneity created by plasma oxidation occurs through physisorption. The removal of chemical functionalities from HOPG surface enhances mercury physisorption. Plasma oxidation of HOPG provides additional surface area for mercury adsorption. Mercury adsorption by activated carbon at atmospheric pressure occurs through two distinct mechanisms, physisorption below 348 K and chemisorption above 348 K. No significant impact of oxygen functionalities was observed in the chemisorption region.

The key findings of this study open the possibility to apply scientific information obtained from studies with simple surfaces like HOPG under ideal conditions (UHV) to industrial sorbents under realistic process conditions. HOPG surfaces can be modified chemically and topologically by plasma oxidation to simulate key features of activated carbon adsorbents.

DESCRIPTORS

Activated carbon	HOPG
Adsorption	Morphological heterogeneity
AFM	ODR
Chemical functional group	Plasma oxidation
Desorption	TPD
Fixed bed adsorption	UHV

ACKNOWLEDGEMENTS

First, I am especially grateful to my research advisor, Dr. Radisav D. Vidic, for his guidance and support throughout the course of this study. His unparalleled dedication and insight were instrumental to the progress of the research. My experience working for him was very enlightening and rewarding.

I express appreciation to Ph.D research co-advisor, Dr. Eric Borguet, for his aid and encouragement throughout the course of this study. He has been supportive of my professional development and has encouraged me beyond the perceived limits of my capability.

I am thankful to Dr J. Karl Johnson for the collaboration he and his group kindly provided, in particular the insight of molecular simulations and useful discussions.

Appreciation is acknowledged to the members of the oral examination committee members, Dr. Ronald D. Neufeld, and Dr. Leonard W. Casson, for their comments and help in preparation of the final draft.

I would like to express a special acknowledgement to Dr. John T. Yates, Jr. and his group, especially JeaGook Lee, for lending UHV equipment and the benefit of their experiences in surface science. Thanks also go to the master machinists and craftmen, Ken, Dennis and Tom, in the mechanical shop in the Department of Chemistry for manufacturing the UHV chamber and other useful materials for my research.

Many thanks go to my colleagues in the Department of Civil and Environmental Engineering and the Department of Chemistry at the University of Pittsburgh, Dora, Vasili, Tao, Nicole, and John, especially to Dr. Yufan He for helping with atomic force microscopy.

I would like to thank the Department of Civil and Environmental Engineering at the University of Pittsburgh for providing partial financial support. The research was made possible by generous financial support from the U.S. Department of Energy.

I am sincerely thankful to family, my parents, parents-in-law, brothers and brothers-in-law, supporting me throughout the study, without whose support and love this work would not have been possible.

Finally, this work is dedicated to the love of my wife, Naseon. She has inspired me to be a better person and provided me with the courage and passion that has been missing from my life for too long.

TABLE OF CONTENTS

ABSTRACT iii

ACKNOWLEDGEMENTS ii

TABLE OF CONTENTS iv

LIST OF FIGURES vii

1.0 INTRODUCTION 1

2.0 LITERATURE REVIEW 5

2.1 Mercury Emission and Control Technologies 5

2.2 Chemical and Morphological Heterogeneity of the Carbon Surface 9

2.3 Optical Surface Probes 13

2.4 Temperature Programmed Desorption (TPD) 16

2.5 Kinetics of Adsorption and Desorption on Solid Surfaces 18

2.5.1 Langmuir Adsorption Kinetics 18

2.5.2 Desorption Kinetics 19

2.6 Research Objectives and Outline 21

3.0 MATERIALS AND METHODS 24

3.1 Ultra High Vacuum Apparatus 24

3.2 Sample Preparation and Adsorbates 26

3.2.1 Highly Oriented Pyrolytic Graphite (HOPG) 26

3.2.2 O_2 Plasma Treated HOPG 27

3.2.3 Adsorbates 28

3.3 Temperature Programmed Desorption (TPD) Experiment 28

3.4 Optical Differential Reflectance (ODR) Experiment 29

3.5 Atomic Force Microscope (AFM) Imaging 31
3.6 Activated Carbon Based Fixed-Bed Adsorption 33
3.6.1 Activated Carbon 33
3.6.2 Fixed-bed Adsorption Experiments for Gas Phase Mercury Uptake 33
3.6.3 AAS Calibration 36
4.0 RESULTS AND DISCUSSION 39
4.1 A combined Study Using TPD and ODR Techniques: Acetone Adsorption and Desorption on HOPG Surface 39
4.1.1 Temperature Programmed Desorption (TPD) 39
4.1.2 Optical Differential Reflectance (ODR) 42
4.2 ODR Investigation of Reversible and Irreversible Adsorption and Desorption: Propane Adsorption and Desorption on HOPG 46
4.3 The Effects of Surface Functional Groups on Adsorption and Desorption of Acetone on Carbonaceous Surfaces 52
4.4 The Effects of Surface Functional Groups and Topological Heterogeneity on Propane Adsorption and Desorption on Carbonaceous Surface 59
4.4.1 Adsorption /Desorption on Air-Cleaved HOPG (a-HOPG) 60
4.4.2 Adsorption/Desorption on Plasma-oxidized HOPG (p-HOPG) 62
4.5 Adsorption and Desorption of Mercury on Model (HOPG) and Real (activated carbon) Carbonaceous Surfaces 66
4.5.1 UHV studies with HOPG 66
4.5.2 Fixed-bed Adsorption Studies with Activated Carbon 70
5.0 SUMMARY AND CONCLUSIONS 74
Task 1 75
Task 2 76
Task 3 76
Task 4 77
Task 5 78
5.1 Significance of the Study 80
APPENDIX 88

A1. Propane Heat of Vaporization (at 100 K) Calculation 88
A2. Acetone Heat of Sublimation (at 130 K) Calculation 89
A3. Mercury Heat of Sublimation (at 200 K) Calculation 90
A4. Properties of Adsorbates 91

BIBLIOGRAPHY 93

FIGURES 104

LIST OF FIGURES

Figure 2-1. Normalized difference in p-polarized reflectivity for a 5 Å layer of acetone on HOPG ($\varepsilon_3 = 5.04+i8.4$) and Cu ($\varepsilon_3 = -13.33+i1.24$) as a function of the angle of incidence at $\lambda = 655$ nm. The lines are prediction from equation 4-2. 105

Figure 2-2. Coordinate system describing the polarization state of light. 106

Figure 2-3. Schematic view of various carbon materials..... 107

Figure 3-1.Schematic of the UHV chamber and gas handling unit 108

Figure 3-2 Schematic of the dual sample mount : (a) side view and (b) front view..... 109

Figure 3-3. Structure of HOPG. HOPG is a relatively new form of high purity carbon consisting of planes of well-defined honeycomb structure. 110

Figure 3-4. Schematic of O_2 plasma system 111

Figure 3-5. Experimental procedure for TPD experiments 112

Figure 3-6. Optical differential reflectance (ODR) System..... 113

Figure 3-7. Schematic view of AFM imaging 114

Figure 3-8. AFM images for (a) virgin HOPG, (b) and (c) O2 plasma oxidized HOPG for 20 min (d) for 90 min. Graphs under the images show cross sectional in height 115

Figure 3-9. Setup of the fixed-bed adsorber 116

Figure 3-10. Experimental system for fixed-bed breakthrough tests..... 117

Figure 4-1. TPD spectra for acetone on HOPG at 91 K (temperature ramp at 2.5 K/sec) 118

Figure 4-2. Integrated area of monolayer and bilayer of TPD features. The dotted lines are model fits assuming that adsorption follows Langmuir kinetics 119

Figure 4-3. Schematic of the proposed growth model (Volmer- Weber) of acetone on graphite at 91 K..... 120

Figure 4-4. Intensity of s and p-polarized light reflected from HOPG as a function of exposure induced by acetone adsorption at 1.2×10^{-7} torr and 91 K 121

Figure 4-5. ODR signal as a function of acetone exposure at 91 K..... 122

Figure 4-6. Correlation between ODR and TPD experiments for acetone adsorption on graphite. The solid line is a linear fit of experimental data (R^2=0.995)..... 123

Figure 4-7. (a) Background ODR signal for a clean surface (b) ODR signal during thermal desorption for a surface containing pre-adsorbed acetone..... 124

Figure 4-8. d(ODR)/dT and TPD spectra as a function of temperature for graphite initially exposed acetone at 19L. 125

Figure 4-9. Schematic view of the three layer model. Each layer is described by its dielectric constant (ε_i). d is the adsorbate overlayer thickness, ϕ is the angle of incidence 126

Figure 4-10. ODR signal and TPD area resulting from adsorption of propane on graphite at 100 K as a function of exposure (a) and the correlation between ODR and TPD (b). 127

Figure 4-11. Propane adsorption on graphite at 90 K : ODR as a function of propane pressure 128

Figure 4-12. Propane adsorption on graphite at (a) 90 and (b) 95, 100 and 105 K determined from ODR and molecular simulation as a function of propane pressure[112] 129

Figure 4-13. TPD of propane adsorption on HOPG at 90 K (temperature ramp at 2.5 K/sec) .. 130

Figure 4-14. Plots of the ln P versus 1/T. This approach reveals that the bilayer heat of adsorption of propane on graphite is 23 ± 2 kJ/mol..... 131

Figure 4-15. Evolution of masses 16, 18, 28 and 44 amu during initial heat treatment of air-cleaved HOPG to different temperatures. Data for 16, 18 and 44 amu in the 1323 K scan are multiplied by 10 to aid in viewing 132

Figure 4-16. TPD spectra of acetone on HOPG after heat treatment at various temperatures. Note that identical vertical scales are used for all figures except for 473 K. 133

Figure 4-17. Area of each individual TPD peak. Areas were obtained by the deconvolution of TPD spectra for 25 L exposure. 134

Figure 4-18. Total area of TPD spectra for 25 L and 5 L exposure as a function of heat treatment temperature. 135

Figure 4-19. Experimental (symbols) and simulated (lines) TPD of acetone monolayer. The insert (a) shows the fitting using conventional pre-exponential factor (10^{13} sec^{-1}) for 7 L exposure and insert (b) shows a fitting trial with zero order for 3 L exposure. 136

Figure 4-20. Acetone TPD for 7L exposure at different heating rates. The insert shows a graph of $\ln(\beta/Tp^2)$ versus $1/Tp$ 137

Figure 4-21. TPD spectra at 29 m/e (propane) for air-cleaved HOPG after heat treatment at various temperatures. Note that identical vertical scales are used for all figures. Data for 473 K are multiplied by 10 to aid in viewing. 138

Figure 4-22. TPD areas for propane at 25 L exposure as a function of heat treatment temperature for air-cleaved and plasma-oxidized HOPG. 139

Figure 4-23. Evolution of masses 16, 18, 28 and 44 amu during initial heat treatment of plasma oxidized HOPG to different temperatures. Data for 16, 18 and 44 amu in the 1323 K scan are multiplied by 10 to aid in viewing 140

Figure 4-24. TPD spectra for propane after 1173 K heat treatment for (a) air-cleaved HOPG (b) O_2 plasma-oxidized HOPG. The same arbitrary units are used in both figures to facilitate comparison. 141

Figure 4-25. TPD area of propane for air-cleaved and plasma-oxidized HOPG after 1173 K heat treatment. 142

Figure 4-26. Quantitative analysis of high temperature TPD peak of propane from plasma oxidized HOPG. (a) Coverage dependant first order simulation and (b) average heat of adsorption for both low and high temperature peak 143

Figure 4-27. TPD spectra of mercury on air cleaved HOPG that was previously heated at (a) 473 K and (b) 1273 K 144

Figure 4-28. Modeling of TPD spectrum of mercury at 20 L exposure using coverage dependent first order desorption kinetics(α=0.003) 145

Figure 4-29. TPD area as a function of mercury exposure for air-cleaved HOPG 146

Figure 4-30. TPD spectra of mercury on (a) plasma-oxidized HOPG for 20 min and (b) plasma-oxidized HOPG for 90 min. Note that both HOPG samples were pretreated at 1273 K and that identical scales are used for both figures. 147

Figure 4-31. TPD area as a function of mercury exposure for air-cleaved and 20 min (p-20-HOPG) and 90 min (p-90-HOPG) sample after 1273 K heat treatment 148

Figure 4-32. Impact of temperature on mercury breakthrough from a fixed bed adsorber at influent mercury concentrations of (a) 70 $\mu g/m^3$ and (b) 1120 $\mu g/m^3$ 149

Figure 4-33. Mercury uptake capacity as a function of equilibrium pressure, P_e at different adsorption temperatures (lines represent linear regression fit to experimental data) 150

Figure 4-34. Equilibrium pressure at 200 μgHg/gAC as a function of 1/T. Line (a) represents a linear fit to adsorption data collected below 348 K and line (b) is a linear fit to adsorption data collected above 348 K 151

Figure 4-35. Impact of sample pretreatment on elemental mercury breakthrough from a fixed bed adsorber operated at (a) 293 K and (b) 423 K with influent mercury concentration of 70 $\mu g/m^3$ 152

1.0 INTRODUCTION

Environmental control agencies, researchers and the general public are concerned about the increasing mobilization and release of trace elements to the environment from fossil fuel burning and other combustion processes such as municipal waste combustion (MWCs) and hazardous waste incineration due to their impact on human health and the environment in general. Of 189 hazardous air pollutants listed in Title III of the Clean Air Act Amendments (CAAA) of 1990, mercury is a trace element of special concern because of its high volatility that allows transfer into the flue gas stream during coal combustion. Existing pollution control technologies, such as wet scrubbers and fabric filters, are not capable of adequately controlling gas-phase mercury emissions. Once emitted to the environment, mercury can be deposited locally or globally to create a long-term contamination problem.[1-4] There is a lot of evidence in the literature about the high toxicity of mercury to plants and animals through bioaccumulation and food chain transport. Thus, strict control of mercury emissions from municipal waste combustors (MWCs) and Coal-Fired Power Plants (CFPPs) is required.[4, 5]

Mercury adsorption on carbonaceous surfaces, such as activated carbon, is the most common approach for mercury removal from various sources. It can be implemented as fixed-bed granular activated carbon (GAC) adsorbers or powdered activated carbon (PAC) injection systems.

However, although the carbon-based adsorption technology has been used for air pollution control and has attracted much experimental and theoretical interest in the past decades as well as more recently (consideration of adsorption on carbon surfaces has been extended to new carbonaceous materials, such as carbon nanotubes), there is still a lack of fundamental

understanding of the physics and chemistry of carbonaceous surfaces related to adsorption/desorption kinetics, sorbent capacity, and interference of other components in the gas mixture.

While various factors can influence mercury adsorption and removal, the most important factor is probably the sorbent type and its associated properties. It should be noted that sorbent properties, that allow a given sorbent to effectively adsorb mercury, are not well understood. Specific functional groups present on the good mercury sorbents have not been identified. In addition, the mercury adsorption mechanisms on activated carbon are not well understood. Also, variations in the physical properties of a given sorbent such as size, shape, effective surface area, and porosity can affect adsorption effectiveness.

High surface area nanoporous carbon materials, such as activated carbon, are characterized by high chemical and morphological heterogeneity. These characteristics affect their adsorption capacity, kinetics, and catalytic activity.[6, 7] Therefore, understanding the chemistry and physics of carbonaceous surfaces may enable optimization of their function and usefulness.[8] For example, oxidation of activated carbon by nitric acid creates acidic groups on the surface, thereby hindering alkane adsorption.[9] It is also well known that activated carbon surfaces chemisorb oxygen at low temperature, forming oxygen-containing functional groups.[10] The oxygen-containing functional groups, removed by outgassing above 500 K, can either enhance or reduce the adsorption capacity of microporous carbon depending on the specific adsorbate[11, 12] The presence of functional groups also modifies other carbon properties. For example, when activated carbon is used as a support for Pt catalysts, the dispersion of Pt increases as the concentration of oxygen functional groups on the carbon surface increases[13] because of electrostatic interactions.[14, 15] The high surface area provided by morphological

heterogeneity is one feature that makes carbonaceous materials useful for adsorption purposes. In general, higher surface area provides more adsorption sites leading to higher adsorption capacity.[16] However, the role of the morphological heterogeneity of carbon surfaces is not clearly understood and is still a subject of intense study.[17-20]

Environmental engineers are faced with the lack of fundamental understanding of molecular interactions in complex mixtures and at the mineral, organic, and biological interfaces that characterize environmental systems. This is particularly troubling because many of the techniques and associated methods for data interpretation have been developed to study well defined systems, e.g., single crystals under ideal conditions (ultra high vacuum). However, the application of these tools to environmental samples is very challenging due to their amorphous, complex, and multiple natures. Therefore, the objectives of this study are to investigate chemical functional groups and topological heterogeneity related issues on adsorption through fundamental studies of adsorption and desorption of a model adsorbent representative of volatile polar (acetone), non-polar (propane) organic compounds and vapor phase elemental mercury on a model carbonaceous surface (HOPG, highly oriented pyrolytic graphite), in an ultra high vacuum (UHV) apparatus.

Many environmental phenomena involving carbonaceous surfaces occur under conditions where standard UHV surface science techniques cannot be applied, e.g., atmospheric pressure. Therefore, the optical differential reflectance (ODR) technique was investigated as an in-situ, real time surface analysis approach. It was assessed by comparison of its sensitivity to adsorption and desorption from carbonaceous surfaces with temperature programmed desorption (TPD). The results showed that the strong correlation between ODR, determined in real time, and relative surface coverage determined a posteriori by TPD for metal systems could be extended to

carbonaceous surfaces. By combining these techniques, a new experimental methodology was developed with a potential to be used for many environmental phenomena involving carbonaceous and other adsorptive surfaces.

This study also describes the effects of surface functional groups and topological heterogeneity on adsorption and desorption using air cleaved HOPG and O_2 plasma treated HOPG as model surfaces. The study suggests an integrated approach that may provide a better understanding of adsorption processes and reveal approaches for sorbent optimization. A long-term goal of the study is to design more efficient and cost-effective sorbents for mercury control through the basic understanding of the mercury adsorption process.

2.0 LITERATURE REVIEW

2.1 Mercury Emission and Control Technologies

Mercury emission sources are commonly categorized into natural and anthropogenic sources. Total vapor phase mercury emitted from combined natural sources, such as oceans, can be as high as 2000 ton/year.[21] Lindberg et al.[22] estimated that the total global anthropogenic mercury emissions range from 2000 to 4000 tons/year which represents 30 to 55 % of global mercury emissions. While most other trace elements emitted from human sources (e.g., Co, Fe, and Se) can likely be removed by common air control devices such as electrostatic precipitator (ESP) or fabric filters (bag house)[23], mercury remains mostly in the gaseous form and easily escapes into the air through these control devices.

Combustion of fossil fuels to produce electricity and heat is one of the major anthropogenic sources of mercury emissions. While the US electric utility industry uses three major fossil fuels, normally coal, fuel oil and natural gas, 35 % of the global atmospheric emission of mercury occurs from coal combustion.[24] Chu and Porcella have estimated that 89 tons/year of mercury is emitted to the atmosphere from US coal-fired power plants (CFPPs) in 1990.[25] US EPA estimated that about 300 ton/year of mercury was emitted from anthropogenic sources in the U.S. in 1990, with 30 % of total mercury emissions coming from coal fired power plants (CFPPs).[26]

Hospital/medical/infectious waste incineration is a common unit operation used for medical waste disposal in the United States and worldwide. The US EPA reported that about 2,300 medical waste incinerators (annual operation rate: 37.6×10^5 ton/year) were in operation

and more than 65 ton/year of mercury was emitted from those incinerators in 1995 in the United States. [27, 28]

Although coal fired power plants represent the main combustion source of mercury listed by the US EPA,[29] mercury concentrations in flue gases from municipal waste combustors are much higher than those from CFPPs. Several studies reported that the flue gases from municipal waste combustors have 1 to 3 orders of magnitude higher mercury concentrations than those from CFPPs.[30-32] One of the major mercury containing products burned in municipal waste combustors (MWCs) are household batteries. Based of 1989 estimates, approximately 600 tons of mercury in household batteries was added to municipal solid waste and their separation would result in 80% reduction of mercury emissions.[33] Other significant mercury inputs into MWCs are paper industry, ferrous food cans, and electronic devices including mercury lamps.[33]

Cement manufacturing and smelting and refining of metals belong among minor sources of mercury emission.[33-36] Pai et al.[28] estimated that cement production industries emitted about 5 ton/year of mercury during 1990.

While studies to control trace elements have focused largely on the destruction and removal efficiency of incinerators for hazardous organic compounds and on the particulate removal efficiencies of air pollution control systems, attention has recently focused on the potential risks related to stack emissions of carcinogenic compounds and toxic metals. As part of these efforts, many countries have set limits for the emission of hazardous air pollutants. The EEC (European Economic Community) is restricting mercury emissions from municipal waste combustors to 50 $\mu g/m^3$.[37] In the United States, most states have limits for mercury emissions in a range of 100 – 130 $\mu g/m^3$.[37] However, the regulations governing mercury emission will probably require lower limits than current regulation.

Activated carbon adsorption has been the most common approach for mercury removal from air. It can be implemented as fixed-bed granular activated carbon (GAC) adsorbers or powdered activated carbon (PAC) injection systems. There are numerous studies in the literature and field works on the capacity of activated carbon to adsorb mercury from flue gas streams under a variety of process conditions.[37-39] In this study, the adsorption capacity of activated carbon was found to depend on its surface area, temperature, mercury concentration and speciation, etc. Generally, a high portion of oxidized mercury, high sorbent surface area and low temperature represent favorable conditions for high mercury removal.[37-39] Other flue gas components, such as sulfur dioxide, water vapor[37], oxygen and HCl [40], can also affect the saturation capacity and the time needed to reach the saturation capacity for gas-phase elemental mercury. However, mercury removal by virgin activated carbon adsorption showed limited success especially in the case of very high temperatures and short contact times.[41-43]

In recent years, chemically modified novel activated carbon sorbents have been developed for mercury removal. While the mechanisms of mercury uptake for these sorbents are not fully understood, orders of magnitude increases in mercury adsorption capacities compared to virgin activated carbons were exhibited.[44]

Numerous studies tested the effect of sulfur impregnation on activated carbon on mercury removal capacity using fixed bed system.[16, 44-46] It was found that the removal capacity drastically increased with sulfur impregnation because of mercury chemisorption as compared to physisorption mechanisms that predominate for virgin carbons and lower temperatures. However, a high concentration of sulfur on activated carbon does not always guarantee higher mercury removal efficiency. Otani *et al*.[16] reported that if impregnated sulfur blocked accessible pores, resulting in significant reduction of the surface area of activated carbon, mercury

adsorption efficiency could decrease even at higher sulfur content. Kwon and Vidic [46] and Liu *et al*.[40] also discovered that the uniform distribution of short linear chains of sulfur alloptropes (S_2 and S_4) on activated carbon obtained from elemental sulfur at high temperature (600 ^oC) showed much higher mercury adsorption capacity compared to those produced by H_2S oxidation at lower temperature (150 ^oC). These studies concluded that the sulfur impregnation temperature, which dictates the predominant sulfur alloptropes on carbon, the sorbent surface area remaining after impregnation, and the pore size distribution strongly affected mercury removal efficiency by impregnated sorbents.

Karatza *et al*.[47] studied adsorption of mercuric chloride on activated carbon and on Na_2S impregnated carbon. This study showed that impregnation with Na_2S enhanced the adsorption capacity of activated carbon for $HgCl_2$, especially at 150 ^oC. It was also suggested that 18.7% Na_2S on activated carbon doubled in mercury chloride adsorption capacity compared to activated carbon impregnated with 7.8% Na_2S. However, the adsorption isotherm data indicated that adsorption on Na_2S impregnated activated carbon did not occur via a chemical reaction of $HgCl_2$ with Na_2S, but that impregnation with Na_2S increased the number of active sites.

Powdered sorbent e.g., powdered activated carbon (PAC)) injection systems have been developed as a cost effective means of mercury removal from flue gas since they can be combined with existing particulate control facilities. The PAC injection technique involves the injection of PAC into the flue gas stream after which mercury loaded sorbent particles are collected in downstream particulate control devices, such as ESPs and baghouses. The efficiency of activated carbon injection in capturing vapor phase mercury is dependent on activated carbon properties, flue gas composition, temperature, type of fuel used, and sorbent injection rate.[42, 45] However, these studies show numerous discrepancies in the results, which suggests that factors

influencing mercury removal are very complex. A fundamental understanding of the adsorption mechanisms under well defined conditions is essential in order to elucidate the role of each factor and advance the future of this control technology.

2.2 Chemical and Morphological Heterogeneity of the Carbon Surface

High surface area nanoporous carbon materials (e.g., activated carbon) are characterized by a great degree of chemical and morphological heterogeneity. These characteristics affect their adsorption capacity, kinetics, and catalytic activity.[6, 7]

It has long been known that oxygen-containing functional groups, that normally exist on a variety of carbon surfaces, play important roles in the adsorption of organic and inorganic compounds or catalytic reactions occurring on the carbon surface. It is also well known that activated carbon chemisorbs oxygen at low temperatures (e.g., at room temperature and atmospheric pressure), thereby forming oxygen-containing functional groups.[10] It has been suggested that the major oxygen-containing compounds on activated carbon surface are carbonyl-, phenolic-, lactonic- or carboxyl type functionalities.[48] In spite of the importance of carbonaceous materials, the understanding of the role of the chemical and morphological characteristics for the carbon surface in terms of surface related properties (e.g., adsorption, catalysis) is less developed compared to the understanding of other materials.

There are numerous studies in the literature on the impact of surface chemical functional groups, both naturally occurring or artificially introduced, on the capacity of carbon surfaces to adsorb organic or inorganic adsorbates under a variety of process conditions. The oxygen-containing functional groups, that can be removed by outgassing above 500 K, can either

enhance or reduce the adsorption capacity of microporous carbon depending on the specific adsorbate.[11, 12] Mangun et al.[49] concluded that the activated carbon fiber (ACF) adsorption capacity for sulfur dioxide (SO_2), the principal cause of acid rain, is highly dependant on the amount of nitrogen containing functional groups. The introduction of nitrogen containing functionalities by ammonia treatment of ACF significantly enhanced the amount of SO_2 adsorption by suppressing the catalytic reaction between oxygen chemisorbed on the surface and SO_2. Swiatkowski and Goworek[50] treated activated carbon with O_3, H_2O_2 and H_2SO_4 and showed that the formation of oxygen functional groups on the activated carbon surface enhanced the adsorption capacity of activated carbon for volatile organic compounds (C_6H_6).

The existence of chemical functional groups can also have negative impact on the adsorption capacity of carbon-based sorbents. Bandosz et al. found that oxidation of activated carbon by nitric acid creates acidic groups on the surface and hinders alkane adsorption.[9] The negative impact of functional groups was reported in the study of xenon adsorption in single walled carbon nanotubes (SWNTs).[51, 52] Thermal treatment above 600 K leads to desorption of oxygen- and hydrogen- containing functional groups, which are believed to block the entry ports of the nanotubes without changing the basic tubular structure of the nanotubes. The removal of these functional groups enhances the capacity of carbon nanotubes for xenon adsorption as well as the uptake efficiency.[53]

Chemical functional groups on carbon surfaces also affect the adsorptive efficiency of inorganic adsorbates. Jia and Thomas[54] introduced various types of oxygen containing functional groups onto coconut shell-based activated carbon via nitric acid oxidation and tested its adsorptive capacity for cadmium ions. Although some phenol and quinone groups were formed by nitric acid treatment, carboxylic acid groups were the main compounds created by this

treatment. Cadmium adsorption was enhanced by the introduction of these functional groups. Removal of these acidic functional groups by thermal treatment resulted in significant deterioration in adsorptive capacity for Cd^{2+}.

Toles et al.[48] quantified surface functional groups on a nutshell-based granular activated carbon by titration with bases of different ionization potentials after air oxidation and showed that copper (Cu^{2+}) uptake appears to be directly correlated with the amount of oxygen containing functional groups in liquid phase. The correlation of the amount of oxygen containing functional groups with copper uptake was especially true for carbonyl groups as well as ionizable groups such as carboxylic acids and lactones.

The high surface area provided by morphological heterogeneity is one of the major features that makes carbonaceous materials useful for adsorption purposes. In general, higher surface area provides more adsorption sites leading to higher adsorption capacity for both organic and inorganic adsorbates.[16] Chiang et al.[55] investigated the effects of carbon treatment with inorganic salts, for example by $Mg(NO_3)_2$, on physical characteristics and adsorption efficiency for acetic acid. Significant variation in pore volume and diameter was observed when the initial pore diameter was less than 7 Å because activation with $Mg(NO_3)_2$ reduced both the surface area and pore diameter of activated carbon. As a result, the adsorption capacity for acetic acid was lowered. However, regeneration of activated carbon at 400 ^{o}C restored high acetic acid adsorption capacity by opening the micropores and increasing the surface area.

Morphological heterogeneity of carbon surfaces also affects the adsorptive efficiency for inorganic adsorbates. In the fixed-bed study with six activated carbons, Krishnan et al.[37] observed an increase in gas phase elemental mercury adsorption with an increase in surface area and suggested that the total sorbent surface area is directly related to the adsorption capacity. Hsi

et al.[56] suggested that the higher percentage of micropores leads to more effective elemental mercury uptake by activated carbon if other chemical and structural parameters are the same.

However, there are numerous conflicting reports in the literature on the effect of chemical and morphological characteristics of carbon surface on adsorption.[17-20, 57, 58] Several studies argued that oxygen containing functional groups introduced by nitric acid oxidation weakened the capacity of activated carbon for SO_2 uptake,[59] while others suggested that the treatment of activated carbon with nitric acid enhanced SO_2 adsorption and its oxidation to SO_3.[12, 60] It was reported that there is no strong correlation between SO_2 adsorption capacity and activated char surface area.[57] However, Davini suggested that surface area is the key physical parameter determining adsorptive capacity of activated carbon for SO_2,[19] while Daley et al. reported that the pore size and volume are more important than surface area.[20] There are also conflicting arguments on the effect of pore size distribution (importance of micropores versus the transport pores) on SO_2 adsorption capacity of carbon.[17, 18] Therefore, the role of the morphological heterogeneity of carbon surfaces is not clearly understood and is still an object of intense study. It should be an important subject to study.

Unequivocal characterization of the chemical properties of carbon surfaces lags behind that of other surfaces due to the complexity of carbon surfaces compared to many other materials. Understanding the chemistry and physics of carbonaceous surfaces may enable optimization of their function and usefulness.[8]

2.3 Optical Surface Probes

It is known that when molecules adsorb on metal surfaces this changes the optical response of the surface.[61] These changes can be utilized to investigate molecule-surface processes, e.g., adsorption. In the study of surfaces, there are a number of advantages of optical techniques compared with conventional surface probes, such as ion and electron spectroscopy and temperature programmed desorption spectroscopy (TDS). Optical techniques are surface sensitive, *in-situ*, and non-destructive methods to investigate surface processes.[62] Optical techniques are useful over a wide range of ambient conditions, can be extremely sensitive and offer real-time detection.[63-65]

A number of different optical techniques have been developed to study surfaces. For example, infrared (IR) spectroscopy is widely applied to investigate adsorbates on both metal and semiconductor surfaces.[66] However, it is not typically resistive to metal adsorbates such as mercury.

Adsorbate induced non-resonant reflectivity changes can probe adsorbate coverage on metal surfaces quantitatively. Optical differential reflectance (ODR) is an optical technique that has been applied to investigate adsorption and desorption on surfaces, resulting in estimation of coverage from optically determined film thickness.[65, 67] This technique uses the small change induced in the reflectivity when a molecule adsorbs onto the surface.[68, 69]

ODR has been used to investigate adsorption and desorption kinetics of a chemisorbed species, CO, on a metal surface, Cu(100), at visible wavelengths (632 nm) under ultra high vacuum (UHV) conditions.[61] ODR is sensitive to chemisorption,[61] and, in favorable cases, physisorption on metal surface.[61] Chemisorption causes a much greater ODR signal change due

to adsorbate-induced perturbation of electronic structure of the metal surface. It is also reported that the utilization of ODR technique to study surface kinetics must rely on the correlation of the reflectivity changes with coverage. A good correlation between reflectivity change from adsorbate coverage and relative coverage estimated by temperature programmed desorption was demonstrated.[68]

ODR enabled adsorbate coverage measurements during the adsorption/desorption of physisorbed species on a metal surface.[63] Wong and Zhu[63] investigated the adsorption and desorption of Xe on Ni surface and found that the ODR signal increased almost linearly with the surface coverage of Xe. The ODR signals can be described by a three-layer model with the known dielectric responses of the surface layer.

ODR can be used over a broad spectral range. It has been shown that chemisorption of H on W (100) results in an optical reflectance change attributed to an adsorbate induced electronic resonance in the infrared (IR) region.[70] Subsequent studies have demonstrated the presence of nonresonant reflectivity change in the IR and visible region for other chemisorbed systems, such as CO on Pt(111)[67], and NO on Cu(111).[71]

ODR has been employed to investigate diffusion on metal surfaces.[72] Xiao et at.[72] revealed that diffraction of reflected light is sensitive for the diffusion of adsorbed CO molecules on Ni surface with much higher signal-to-noise ratio than second harmonic generation.[73] In summary, ODR measures the change of light intensity reflected from a surface induced by adsorption and desorption and is a simple and versatile surface sensitive probe.

In this study, ODR was used in order to monitor adsorption and/or desorption of polar and non-polar organics and metals on carbonaceous surfaces. One significance of the ODR study is the ability to observe adsorption and desorption with real time resolution. The details of how

reflectivity changes when a new layer is deposited on a planar surface under UHV condition will be described in Section 4.1.2.

In order to establish the utility of the ODR technique for carbonaceous surfaces, the calculation of the angular dependent sensitivity change for monolayer of acetone adsorbed on two different surfaces is illustrated in Figure 2-1. The conventional three-layer model was applied for this calculation (see Section 4.1.2). The y-axis in Figure 2-1 is the normalized change of surface reflectivity as a function of the angle of incidence of light (x-axis). The light approaching and reflected from surface can be divided into two components, p- (electric field in the plane of incidence) and s-(electric field perpendicular to the plane of incidence) polarized light. (Figure 2-2) As the angle of incidence increases, the reflectivity of p-polarized light for HOPG changes for more than either s-polarized light for HOPG or p-polarized light for copper. The reflectivity change of p-polarized light induced by physisorbed acetone on HOPG (Figure 2-1) is over an order of magnitude higher than for Cu at an incident angle of 75 degrees. Based on the model calculation in Figure 2-1, and given that the noise of the laser source is about 0.0005 in $\Delta R/R$ units, ODR can be applied with sub-monolayer sensitivity (i.e. < 0.01 ML) for physisorption systems on carbonaceous surfaces. In addition, the intensity change from s-polarized light is almost negligible, which suggests that it can be used as a reference signal for the experiments. Therefore, from the prediction of the reflectivity change from HOPG with a model polar organic compound it should be possible to use the ODR technique to study carbonaceous surfaces with greater sensitivity than metal surfaces.

2.4 Temperature Programmed Desorption (TPD)

Temperature programmed desorption (TPD) spectroscopy is one of the most widely used analytical techniques in ultra high vacuum (UHV) surface science.[74] In a typical TPD experiment, gas molecules are adsorbed on the clean surface by backfilling the UHV chamber to a fixed pressure for a fixed time at a known surface temperature.(Fig 3-5) The chamber is then evacuated back to UHV conditions followed by programmed heating of the surface with continuous monitoring of desorbed molecules by a quadrupole mass spectrometer (QMS).

TPD is a simple method to monitor the thermal evolution of the adsorbate layer into the gas phase and to determine the binding energy between adsorbate and surface[75]. The reaction order and sticking coefficient, i.e., the probability that a gas molecule hitting a surface will remain adsorbed, can be deduced from a series of desorption spectra with different initial doses. TPD can also provide information about the kinetics of adsorption and desorption, directly or indirectly. The relative amount of adsorbed molecules is determined by integrating the desorption signal. Computer fitting using proper adsorption models can be used to determine the desorption parameters.[76]

TPD was developed in the late 1940's, and has been extensively used to characterize energetics and surface stoichiometry for adsorbates on various surfaces.[77] For instance, using TPD experiments to study desorption of ethers and alcohols from a-CN_x, amorphous hydrogenated carbon, surfaces as a model for the interaction of perfluoropolyalkyl (PFPE) lubricant with surface of magnetic storage devices, Paserba et al. measured the desorption energy and suggested that the hydrogen bond with a-CN_x increased as a result of fluorination of the adsorbate.[78] TPD has been used to study oxide formation on tungsten surfaces at high

temperature, e.g., > 1200 K.[79, 80] At low coverage on tungsten surface, oxygen mainly desorbed as oxygen atoms with first order kinetics. However, as oxygen coverage increased, oxygen desorbed as the oxide (WO_x). This study also found that the sticking probability of oxygen is highly dependent on surface temperature and coverage.[80]

TPD can be combined with other techniques.[8, 51, 81, 82] With the aid of molecular simulation and FTIR, Kuznetsova et al. described how the adsorption capacity of single walled carbon nanotubes (SWCNs) for Xe increases after removal of chemical functional groups on SWCNs. In this study, TPD revealed that thermal treatment above 500 K leads to desorption of oxygen- and hydrogen- containing functional groups and the removal of these functional groups enhances the capacity of carbon nanotubes for xenon adsorption as well as the uptake efficiency[53]. However, TPD is limited in its ability to identify the microscopic nature of the adsorption site mechanism of Xe on nanotubes. Molecular simulations suggest that Xe molecules adsorb into the tubular structure of the nanotubes by opening the entry ports of the nanotubes that are blocked by chemical functionalities.

Although TPD was developed to study adsorbate-surface interactions in UHV, it also can be utilized in atmospheric pressure if the desorbing species of interest can be detected. Otake and Jenkins[10] applied TPD to estimate the amount of chemical functional groups on activated carbon surfaces. Li et al.[83] performed TPD experiments after adsorption of elemental mercury on activated carbon samples and provided evidence that chemisorption predominates over physisorption for mercury adsorption on moisture-containing activated carbon samples. However, TPD under atmospheric pressure is limited to the estimate of the energetics of adsorption or desorption due to difficulty of initial exposure estimation and high background contribution, etc. Another disadvantage of TPD is that it destroys adsorbed layer. In spite of

numerous limitations, however, a great deal of information can be obtained about surface processes using the TPD technique.

2.5 Kinetics of Adsorption and Desorption on Solid Surfaces

The fundamental description of adsorption and desorption kinetics is presented in this section for the development of specific models used to analyze experimental results in later sections.

2.5.1 Langmuir Adsorption Kinetics

The Langmuir adsorption model provides a simple picture of adsorption at low pressure and is applicable in many situations of gas adsorption on surfaces.[84] Basic assumptions of the Langmuir model are; 1) the adsorption probability depends on the number of available sites; 2) no mechanism exists for lateral transport of impinging gas in a weakly bound state; 3) all molecules bind to identical sites, 4) no multilayer formation, and 5) adsorbate configuration on the surface is completely random.[85] The Langmuir adsorption model is described by the following equation;

$$\theta(L) = \theta_s[1 - EXP(-kL/\theta_s)] \qquad (2\text{-}2)$$

where θ is the surface coverage, L is the exposure in Langmuir (1L is the exposure for 1 sec at 10^{-6} torr), k is the rate constant for adsorption and θ_s is the saturation coverage[85]. The surface coverage is defined by:

$$\theta = \frac{Number\ \ of\ \ occupied\ \ adsorption\ \ sites}{Total\ \ number\ \ of\ \ adsorption\ \ sites} \qquad (2\text{-}3)$$

Relative surface coverage can be extracted by integrating the area of the peaks in a TPD spectrum. The major feature of this model is the coverage dependence the sticking coefficient. The sticking coefficient describes the probability that a gas molecule hitting the surface site will remain adsorbed.

2.5.2 Desorption Kinetics

In a TPD experiment, the partial pressure increase caused by desorbing species during heating of a surface contains a great deal of information about the desorption process, e.g., activation energy, reaction order. The thermal desorption rate can be interpreted by an Arrhenius formula, the so-called Polanyi-Wigner equation, which assumes that the desorption rate constant, k_d, is independent of surface coverage, as follows[75, 77];

$$-\frac{d\theta}{dt} = k_d \theta^n = \nu \theta^n \exp\left(-\frac{E_d(1+\alpha\theta}{RT}\right) \qquad (2\text{-}4)$$

where, $-d\theta/dt$ is the rate of desorption, k_d is the desorption rate constant, θ is the surface coverage, T is the temperature, t is the time, ν is the pre-exponential factor of desorption, and n is the reaction order. α is intermolecular interaction which positives number indicates attractive reaction and negative indicates repulsive reaction. E_d and R are the desorption activation energy and ideal gas law constant, respectively.

A wide variety of different procedures have been developed for the evaluation of the desorption parameters associated with this formula. Leading edge analysis, developed by Habenschaden and Kűpper [86], is frequently used for the interpretation of TPD peaks, especially for zero order desorption (n = 0). Zero order desorption occurs when the desorption rate is independent of coverage, resulting in the same initial desorption rate (leading edge) for different exposures and a sharp drop at the maximum desorption rate [77]. This method uses a plot of Equation 2-4 ($\ln (d\theta/dT)$ versus $1/T$), which yields a straight line with $-E_d/R$ as the slope and $n\ln\theta + \ln\nu$ as the intercept. The activation energy (E_d) can be easily determined from the value of the slope.

In the case when intermolecular interactions are important, the desorption rate parameters will change as a function of coverage. While various approaches are available to determine the desorption reaction order [87, 88], this study uses a simple approximation method developed by Redhead [89] to describe the first order desorption detected by TPD. Redhead developed the relationship between the temperature of maximum desorption rate (T_m) and activation energy from the differentiation of Equation 2-4 when n = 1. The final equation is given as follows:

$$E = RT_p (\ln (\nu T_p/\beta)-3.64) \qquad (2\text{-}5)$$

where, T_p is the temperature at which the maximum desorption rate is achieved and β is the heating rate (dT/dt). A value for ν must be chosen to determine the activation energy value, which is the energy needed to desorb adsorbed species, with the usual choice between 10^{10} and 10^{20}/sec.[90] However, since the deviations in activation energy values are within 1.5% for ν/β in the range between 10^{8} and $10^{13}/K^{-1}$, this approach may be used for the first order desorption.[89] In addition to this simple approach, more sophisticated analysis, e.g., line shape calculation is performed.

2.6 Research Objectives and Outline

The overall goal of this study is to understand the physics and chemistry involved in mercury adsorption on carbonaceous surfaces and to optimize the adsorption process and operating conditions for cost effective mercury uptake. In order to investigate the fundamentals of mercury uptake by carbonaceous surfaces, graphite was employed as a model sorbent and a new sub-monolayer sensitive optical surface probe (ODR) was combined with conventional thermal desorption technique in ultra high vacuum condition. In light of significant interest in mercury adsorption on carbonaceous sorbents, a series of investigations was undertaken. It was necessary to establish that the optical probe is a reasonable tool to study adsorption on carbonaceous surfaces by developing a correlation between the new optical probe (ODR) and a conventional vacuum technique (TPD) for the adsorption/desorption of a model polar organic gas (acetone) on graphite. ODR and TPD experiments and analysis will also elucidate adsorption/desorption kinetics of acetone on graphite, relative surface coverage and adsorbed layer thickness in real time.

One of the advantages of optical techniques over TPD is the practical application under high pressures and reversible reaction conditions. Therefore, a series of ODR experiments was conducted at different surface temperatures to investigate propane adsorption behavior on graphite of pressures ranging from UHV to over 10^{-4} torr. The aim of this part of study was to demonstrate the versatility of the ODR technique under the condition where TPD cannot be used. Furthermore, these tests evaluated the possibility to study mercury adsorption in the gas mixture by documenting the performance of ODR experiments for propane adsorption and desorption on HOPG surface under pressures that are much higher than UHV and approach atmospheric conditions.

The surface of activated carbon is characterized by high morphological heterogeneity and different chemical functionalities. Therefore, the direct extension of adsorption/desorption results obtained for the relatively well-ordered graphite surface with very little chemical functionality to highly non-uniform activated carbon may lead to serious errors in developing practical carbonaceous sorbents. The adsorption and desorption of model adsorbates representative of polar (acetone) and non-polar (propane) organic compounds and metals (elemental mercury) on model carbonaceous surfaces (Air cleaved as well as plasma oxidized HOPG) were performed to elucidate the effects of chemical functional groups and surface morphology on adsorption/desorption behavior. A dynamic mercury adsorption experiments was also conducted with activated carbon (BPL) in fixed-bed reactor in order to compare with the findings of UHV studies.

Figure 2-3 shows a diagram of various carbon materials in terms of chemical and topological heterogeneity. Graphite represents a carbon material which contains very low chemical and topological heterogeneity while activated carbon is very high in chemical and

topological heterogeneity. This study represents an important step in trying to overcome vast differences in chemical and topological heterogeneity between a simple surface like HOPG and a complex industrial sorbent like activated carbon. In order to overcome the differences between HOPG and activated carbon, the mercury breakthough experiments were conducted and the energetics of mercury adsorption from chemically and topologically modified HOPG in the UHV conditions and from activated carbon in atmospheric conditions. Virgin HOPG is assumed to contain no chemical or topological heterogeneity. Creating pits in this homogeneous surface and decorating the edge atoms with typical oxygen functionalities (e.g., carboxyl, carbonyl, etc.) would impart some of the features that are known to exist on activated carbon.[10, 91, 92] On the other hand, there is very little that can be done to alter topological heterogeneity of activated carbon in a controlled fashion. However, outgassing at elevated temperatures would remove most of the oxygen functionalities on this industrial sorbent with minor changes in surface area, pore structure or pore size distribution.[93]

While there is still a significant void space on Figure 2-3, it should be possible to fill it at least partially through careful selection and modification of other carbonaceous surfaces like carbon molecular sieves, activated carbon fibers, carbon nanotubes, etc. This study represents the first steps in filling that space in an effort to understand fundamental aspects of elemental mercury adsorption by carbonaceous sorbents.

3.0 MATERIALS AND METHODS

3.1 Ultra High Vacuum Apparatus

A custom-made stainless steel UHV chamber, shown in Figure 3-1, was used for all the experiments in this study. The UHV conditions are achieved by a 350 L/sec turbo molecular pump (Leybold, Model: Turbovac350, Export, PA) backed by a mechanical pump (Leybold, Model D16-B, Export, PA). The base pressure of 5×10^{-10} torr can be accomplished after over 72 hours of chamber bakeout at around 200 ^{o}C and appropriate degassing of all equipment in the chamber.

The number of molecules with molecular weight M hitting a unit surface area per unit time, denoted as f, is given in practical units (P in torr and T in K) as [89]:

$$f(cm^{-2}\sec^{-1}) = \frac{3.51\times10^{22}P}{\sqrt{TM}} \qquad (3.1)$$

In order to evaluate the base pressure contribution to surface coverage, one can consider a surface in contact with gas at a pressure of 1×10^{-6} torr for one second, which is one Langmuir (L) exposure. If N_2 is used as the adsorbing gas then a 1L exposure means will produce one monolayer assuming 100% sticking probability. However, if the pressure is maintained at 5×10^{-10} torr, about 85 min of exposure with N_2 at room temperature is required to achieve the same conditions assuming a typical surface coverage of 10^{15} cm^{-2} and assuming that each N_2 molecule sticks to the surface. Therefore, 5×10^{-10} torr of base pressure is suitable to study the surface adsorption and desorption.

The chamber was equipped with a Bayard-Alpert type (nude) ion gauge (Kurt J Lesker, Model : G8130) and a quadrupole mass spectrometer (QMS, AccuQuad300, Stanford Research System, Sunnyvale, CA) to measure total and partial pressure in the chamber. While the ion gauge filament is exposed to the chamber space, the QMS probe arm is sealed by a stainless steel shield with 0.1in diameter aperture. The shield opening could be repeatedly located to within < 1mm of the sample and retracted about 20 mm by a movable vice. This configuration ensures the collection of molecules from sample alone and allows for sample rotation and adsorbate exposure.[94, 95] The chamber is equipped with several view ports to allow the laser light access and observation of the sample inside the chamber.

A schematic view of the sample mount is depicted in Figure 3-2. A dual sample holder is mounted on a copper (OFHC) block welded on a stainless steel liquid nitrogen reservoir. The sample holder can be rotated around the z-axis by a sample munipulator (MDC, model RMTG-275, Hayward, CA) for placing the sample to an appropriate position. Two copper supports are fitted on both sides of the block and electronically isolated in order to allow independent heating of each sample. Samples are mounted on the sample holder with Ta support plates to which a thermocouple tip is welded.

The sample can be heated resistively up to 1300 K with a linear ramping control and cooled to 87 K with liquid nitrogen. A bundle of copper wires is attached to the copper supports to provide electric power. The sample temperature is measured by a chromel-alumel (K-type) thermocouple. Adsorbate exposure is accomplished by backfilling the chamber via a leak valve (Duniway Co., Model VLVE-1000, Mountain View, CA) from the gas reservoir attached to the chamber. The gas reservoir, including stainless steel gas lines and connections, is also pumped

by a mechanical pump and baked out to get rid of impurities such as water vapor and previously used gas.

The constant temperature ramping rate, typically 2.5 K/sec, is accomplished by a 40 amp-power supply (Kepco, KS DC power supply, Flushing, NY) controlled by a computer with LabView interface (Version 5.0, National Instruments, Austin, TX). Total and partial pressure, sample temperature and laser signal can be monitored via a computer equipped with an A/D board (PCI1200, National Instruments, Austin, TX) and controlled by a customized LabView program.

3.2 Sample Preparation and Adsorbates

3.2.1 Highly Oriented Pyrolytic Graphite (HOPG)

HOPG is a relatively new form of high purity carbon, consisting of a well-defined honeycomb structure of carbon as shown in Figure 3-3. The substrate used in the study was a 10 × 10 × 2 mm HOPG sample (Grade SPI-1, SPI Supplies, West Chester, PA) and a 12 × 12 × 2 mm HOPG sample (Grade ZYA, Advanced Ceramics, Lakewood, OH). A 2 mm – thick HOPG was sliced with a razor blade into several thin (0.5 mm) samples for installation in the chamber or O_2 plasma treatment. After air cleaving with adhesive tape to remove the topmost layers of the HOPG surface and expose a fresh surface of basal plane graphite to air, the HOPG was mounted on the sample support. Two mounting holes (Dia =1/16 inch) were drilled in each HOPG samples using clean tools sonicated in 100 % acetone. Atomic force microscope (AFM) images of the sample were taken at atmospheric pressure prior to installation into the chamber.

After the chamber bakeout, the samples were typically annealed at 1000 K overnight for acetone TPD and ODR experiments. For the experiments investigating chemical functional effects, both air cleaved and O_2 plasma treated samples were subjected to the routine bakeout procedure and annealed to the desired temperature before experiments. This annealing procedure removes possible contamination adsorbed from the background or introduced during sample preparation [94, 95]

3.2.2 O_2 Plasma Treated HOPG

In order to investigate the effects of surface morphology on adsorption and desorption, HOPG samples were treated in oxygen plasma to create defects and pores in this ideal surface. Figure 3-4 illustrates the treatment scheme. A raw HOPG sample on a glass slide was placed in the plasma generator (March Instruments Inc., Model March Plasmod). The pressure was lowered to 5×10^{-3} mbar by a mechanical pump. During pumping, high-grade oxygen gas was introduced into the generator through a flow controller (March Instruments Inc., Model GCM 250, Concord, CA) to achieve the pressure of 1 mbar. Oxygen pressure was maintained for several minutes to ensure that the oxygen gas filled the entire generator. The plasma flux was provided for 20 and 90 minutes at the power of 100 W. After the treatment, the sample was transferred to a clean plastic container to avoid damage or contamination. The treated sample was examined by AFM prior to installation. The topological surface modification will be discussed in Section 3-5.

3.2.3 Adsorbates

Acetone used in this study was research grade and was degassed by freeze – pump – thaw cycle before dosing. A 195 K temperature bath, which lowers the temperature below the freezing point of acetone (T_{melt} = 239 K), was prepared with dry ice and acetone[96].

Propane was commercially available research grade and was used as supplied.

The gas phase mercury was generated from a mercury permeation cell (VICI Metrons Inc. Santa Clara, CA) and was prepared by the same freeze – pump – thaw cycle as for acetone. Since mercury vapor pressure is not high enough to achieve reasonable dosing pressure, the mercury reservoir and gas lines were heated at about 100 ^{o}C by a customized heating oven to increase the vapor pressure of mercury.

3.3 Temperature Programmed Desorption (TPD) Experiment

A clean surface exposed to a gas at fixed pressure and constant surface temperature for a fixed time duration provides the initial condition. During the desorption cycle as the temperature is increased at a constant rate and the mass spectrometer is used to detect the type and the amount of species desorbing from the surface. Figure 3-5 describes the steps in a TPD experiment.

TPD experiments always began with cooling the samples to below 90 K using liquid N_2. After the sample was positioned to face the QMS, the QMS shield opening was brought close to the sample (< 1mm). The sample was then initially heated at 5 K/sec to a desired temperature depending on the purpose of the experiment and gas species that evolved from the surface were

monitored by the QMS. The gas compounds monitored in this initial phase are at 16 atomic mass unit (amu), at 18 amu, at 28 amu and at 44 amu. This most likely corresponds to CH_4, H_2O CO and CO_2. Once the sample reached the desired temperature, it was cooled back to 90 K as fast as possible and the shield was retracted to allow dosing. The sample was typically held around 90 K during dosing. Once the exposure (L) reached the desired value, the QMS shield opening was brought close to the sample surface. The sample was heated at a known rate (typically at 2.5 K/sec) while monitoring the sample temperature and partial pressure of adsorbates as a function of time. Once the sample reached the desired temperature (typically 373 K) the heating was stopped and the sample was cooled back to 90 K for subsequent TPD experiments. The resulting QMS signals at 43 amu for acetone, 29 amu for propane and 201 amu for mercury integrated over the desorption temperature range provide the relative amount of adsorbate loaded on the sample surface during the adsorption phase.

3.4 Optical Differential Reflectance (ODR) Experiment

The optical set-up for measuring the ODR signal induced by surface adsorption and desorption is illustrated in Figure 3-6. The laser light, via a polarizer and half waveplate, enters the chamber through a viewport to the sample. The reflected light is divided into two components and two photodiodes measure the intensity of the light. The light source for optical differential reflectance is a low-cost laser pointer (Marlin P. Johnson & Assoc. INC, model #8689-LZ, Lake Park, FL), which is operated at the maximum output power of 5 mW with the wavelength of 655 nm. The laser beam passes through a polarizer (Lambda Research Optics, INC. model ppb-2506u-248, Costa Mesa, CA) and half wave plate (Lambda Research Optics,

INC. model WP-10QC-M, Costa Mesa, CA) on a rotable mount to adjust the relative intensity of p- and s- polarized light incident to the sample. The polarized laser beam is introduced to the sample via a view port and reflected at an angle of about 65 ± 2°, for acetone, and 70 ± 2°, for propane experiments, off the sample housed within a UHV chamber. The reflected light is divided into p- and s- polarized light via a polarizing beam splitter (Coherent, model 44-4703, Santa Clara, CA). Each polarized light intensity component is measured separately by commercially available photodiodes (Thermolabs, model DET-110). For a typical ODR experiment, the cycle started by first cooling the sample and then cleaning it by heating to over 1000 K. The sample is then brought to a desired temperature (typically 90 K) and the intensities of reflected p- and s- polarized light were equalized by adjusting the half wave plate. The monitoring of ODR signal, temperature and pressure as a function of time was performed while dosing the adsorbate gas. After completing the desired exposure (L), the temperature was ramped to about 373 K for desorption, while still monitoring all three signals. As soon as the desired temperature was reached, the heating was stopped and the signals were saved. The experimentally measured normalized ODR signal change is reported as ΔR/R, which is defined by equation (3-2)

$$\frac{\Delta R}{2R} = \left(\frac{I_P - I_S}{I_P + I_S} \right) \qquad (3\text{-}2)$$

where, R is the total reflectivity of clean surface and ΔR is the reflectivity change due to adsorption or desorption. The customized unit for reporting the ODR signal change is either % or relative arbitrary units. ΔR/R is a complex function of the incident angle, as well as the optical

properties of the adsorbate and substrate. [61, 97-99] I_p and I_s indicate the intensity of p- and s-polarized light reflected from the substrate surface, respectively. Both these quantities are linearly related to the reflectivity: $I_s = R_s I_{os}$, $I_p = R_p I_{op}$, where I_{os} and I_{op} are the intensity of p- and s- polarized light incident on the surface and R_s and R_p are the reflectivity of s- and p-polarized light, respectively. The p-polarized light is the "signal" and the s-polarized light is used as the "reference" due to the fact that adsorbate-induced reflectivity changes depend on polarization, with p-polarized light being far more sensitive than s-polarized light to the presence of adsorbates.[68] This subtraction scheme cancels drift and noise caused by the fluctuations of laser intensity and mechanical instabilities that are polarization independent thereby, maximizing the signal to noise ratio. A sensitivity of 0.04 % ($\Delta R/R$) over the time of a single experiment is achieved even with base intensity drift and fluctuations as large as 4 %.

3.5 Atomic Force Microscope (AFM) Imaging

Invented in mid 1980's by Binning et. al. [100], atomic force microscopy (AFM) has provided unprecedented microscopic details about a variety of different systems,[101] such as metal electrodes, semiconductors, insulators and biological systems in different environments, such as air, liquid and ultra high vacuum (UHV).

AFM (Pico SPM, Molecular Imaging, Phoenix, AZ) involves, as shown in Figure 3-7, a sharp probe on a cantilever brought into proximity to the surface. A piezoelectric tube is used to control the position of the cantilever (or the sample, depending on the particular instrument) in three dimensions with nanometer precision. The repulsive or attractive interaction between the probe and surface causes the deflection of the cantilever. The deflection of the cantilever is

detected by the movement of laser beam reflected from the top of the cantilever. In contact mode, the most common mode of AFM, the feedback loop attempts to maintain the same deflection while the piezoelectric is scanning the surface line by line. The height signal is recorded at each point on the (x,y) coordinate plane and a topographic plot can therefore be constructed.

Contact mode AFM images were acquired with a Molecular Imaging PicoSPM system (Pico SPM, Molecular Imaging, Phoenix, AZ). Silicon Nitride tips with curvature radius of 10-20 nm and cantilevers with spring constant 0.06-0.12N/m were selected for imaging.

Both raw and plasma oxidized HOPG have been examined by Atomic Force Microscopy (AFM) and Figure 3-8 shows AFM images for virgin and 20 min and 90 min plasma oxidized HOPG. 20 min oxygen plasma treatment provides a significant amount of pits and defects on the graphite surface, which are shown as darker spots on the image, while the air cleaved HOPG reveals a clean and flat surface except for a few steps (0.5~2.5 nm high). The defects on 20 min plasma treated HOPG vary from ~10 to ~200 nm in diameter, and from ~1 to ~10 nm in depth. Longer exposure time to plasma oxidation does not lead to essential changes of HOPG morphology except that pits become wider and deeper. The surface modification by plasma oxidation was fairly reproducible. Two AFM images on Figure 3-8 (b and c) compare two HOPG surfaces after 20 min plasma oxidation on different days under identical treatment conditions and show very similar distributions of defect sites with similar width and depth. Figure 3-8 (d) illustrates an HOPG sample following 90 min plasma oxidation. Defects increased in diameter from ~100 to 500 nm and in depth from ~ 50 to 200 nm, which is commonly observed morphological change of HOPG surface with plasma oxidation.[102]

It can be concluded that plasma treatment results in the formation of a morphologically heterogeneous HOPG surface distinct from the topologically homogeneous virgin or air-cleaved HOPG surface.

3.6 Activated Carbon Based Fixed-Bed Adsorption

3.6.1 Activated Carbon

A bituminous coal-based carbon (BPL) was used in this study. BPL is supplied by the manufacturer (Calgon Carbon Co, Pittsburgh, PA) in 12×30 U.S. Mesh size. 60×80 U.S. Mesh size was produced by pulverizing the carbon and sieving to a desired range. The carbon was washed in deionized water to eliminate fines and impurities. Prior to its use, the carbon samples were dried at room temperature and stored in a dessicator. In order to investigate surface water effect, the stored activated carbon sample was heated to 150 ^{o}C for 2 hours and cooled to room temperature under nitrogen atmosphere. The sample was heated to 1173 K overnight and cooled to room temperature under nitrogen atmosphere to study the effects of chemical functional groups on mercury uptake.

3.6.2 Fixed-bed Adsorption Experiments for Gas Phase Mercury Uptake

Fixed-bed adsorption experiments were conducted to determine mercury uptake by activated carbon under various mercury inlet concentration and adsorption temperatures. Based

on the breakthrough curves, the adsorption dynamics for various adsorbents could be analyzed both qualitatively and quantitatively.

Adsorber experiments were performed using a quarter inch diameter stainless steel column charged with 100mg of sorbent. This set-up was found to induce relatively small pressure drop (< 5 %) across the bed.

Figure 3-9. illustrates schematic view of the fixed-bed reactor. In order to support the 100mg of 60 × 80 U.S Mesh size adsorbent, a 170 U.S Mesh size stainless steel sieve was installed on top of a 10 Mesh size stainless steel sieve that served as structural support. The adsorber was always operated in a down flow mode to minimize the potential for bed fluidization.

A schematic representation of the experimental setup of activated carbon fixed bed adsorption is shown in Figure 3-10. The adsorber was placed in a laboratory oven (Cole Parmer, Model 05015, Cole Parmer Instrument Company, Niles, IL) to control the adsorption temperature. In order to allow efficient heating of the influent gas, 4 ft of coiled Teflon tubing was installed in the oven prior to the adsorber inlet. Two feet of Teflon tubing was placed downstream of the adsorber inside the oven and two feet of Teflon tubing was used outside the oven.

Carrier gas was supplied through a regulating valve (Precision Scientific, Chicago, IL) connected to the nitrogen tank to control the flowrate in the system. The drier was placed downstream of the nitrogen tank to remove the existing moisture content that may influence generation and purity of vapor-phase mercury injected from the mercury permeation device.

Prior to the start of an adsorption experiment, clean nitrogen was passed through the AAS during a one-hour warm-up period. Once the intensity and energy level in AAS was stabilized

auto-zero button was pushed to set a zero point. At this time, the mercury permeation device was introduced on-line and the oil bath temperature adjusted to a desired level. The gas flowrate was adjusted to 1 l/min and the system was allowed to stabilize for a period of two hours. The absorbance reading on the AAS was recorded. and the adsorber was placed on-line and time set to zero.

The absorbance reading from the adsorber effluent was initially recorded every 0.5 minutes with increasing time intervals depending on the rate of mercury breakthrough. Since most adsorber runs didn't last longer than 10 hours, the AAS was turned off when the system reached 100% breakthrough. The next day when the AAS was turned on, it was first re-zeroed by diverting the adsorber effluent away from the AAS quartz cell using a 3-way valve, and supplying clean nitrogen from an auxiliary nitrogen source.

Mercury breakthrough from fixed-bed adsorber is depicted in Figure 4.32 as the ratio of mercury effluent concentration (C_e) to influent concentration (C_o) as adsorber run progressed in time. The lower values of C_e/C_o represents better mercury adsorption by sorbents and $C_e/C_o = 1.0$ indicates that the adsorption column reached 100% mercury adsorption capacity of the sorbent and no more mercury adsorption will occur. After obtaining the mercury breakthrough profile, the adsorptive capacity of the sorbent was calculated by integrating the area above the breakthrough curve using the following equation:

$$Hg\ Adsorbed = \int_{V_o}^{V_t} (C_o - C)dV \qquad (3\text{-}2)$$

where, Co = adsorber influent concentration ($\mu g/m^3$)

C = adsorber influent concentration ($\mu g/m^3$)

V = Volume of mercury laden gas (m^3)

3.6.3 AAS Calibration

It is essential to properly calibrate the AAS so that the absorbance reading from the AAS can be correlated to the concentration of elemental mercury passing through the quartz cell. The AAS used in this study was calibrated based on the EPA Method 7470 (Mercury in liquid Waste, Manual Cold Vapor Technique)[103] and the study performed by Shendrikar et al.[104] Prior to the commencement of the AAS calibration, mercury trapping impinger solution was produced to collect vapor-phase mercury samples in order to calibrate the atomic absorption spectrophotometer (AAS) and to determine the concentrations of total mercury vapor in the gas stream. The impinger solution used for absorbing the vapor-phase mercury was prepared using 1.5 % potassium permanganate ($KMnO_4$, Fisher Scientific, Pittsburgh, PA) in 10 % (3.6N) sulfuric acid (Fisher Scientific, Pittsburgh, PA) as described by Shendrikar et al.[104] The 10 % (3.6N) sulfuric acid solution was prepared by diluting the 36 N sulfuric acid with deionized water. Due to the instability of the impinger solution in the presence of light, all glassware was covered with aluminum foil and the impinger solution was always prepared within 10 hours of its use.

The optimum setting of the monochrometer wavelength of the AAS was 253.7 nm and the slit was adjusted to 0.1 mm. The hollow cathode lamp and quartz cell were positioned to maximize the energy level of the detector. In the calibration process, 1 l/min of a steady-state stream of gas-phase mercury was passed through the AAS quartz cell and trapped in an impinger solution.

Two 250 ml gas trapping impingers with coarse glass stones (Corning Inc. Horseheads, NY) were arranged in series downstream of the AAS quartz cell. The neck of the impinger

cylinders and all the connections were sealed with Teflon tape to secure the ground glass joints and avoid potential leakage of mercury from the impinger train. A three-way valve placed upstream of the impinger train was installed to bypass the impingers and vent the gas stream prior to the commencement of the impinger run. After preparation of the impingers, which were filled with impinger solution and sealed tightly, the three way valve was turned so that the gas stream passed through the impinger solution and a rotameter. The impinger run proceeded for 1 hour, while the absorbance reading detected by the AAS and flowrate of the gas stream were recorded at 5-minute intervals.

The impingers were taken off-line after 1 hour and 100 ml of the impinger solution from each bottle was transferred into a 120 ml-volumetric flask. 10 ml of concentrated hydrochloric acid (aqua regia) was used to collect any mercury that condensed on the walls of the impinger cylinders. Since the concentration of mercury in the first impinger solution may be very high, it usually required dilution with fresh impinger solution to reach the linear range of the liquid-phase calibration curve. The second impinger typically did not require dilution. 100ml of the diluted impinger solutions was transferred to 150 ml PTFE bottle and 15 ml of a solution containing 12 % hydroxlyamine sulfate and 12 % sodium chloride in DI water was added to each bottle to prevent interference of permanganate with mercury analysis by cold-vapor AAS. The PTFE bottles were mixed vigorously, vented to release extra gas generated by the addition of reducing solution, and kept for liquid-phase analysis. A standard mercury solution was prepared by spiking clean impinger solution with a given volume of 1000μg/l mercury atomic absorption standard (Aldrich Chemical Company, Milwaukee, WI). Four standard solutions prepared by serial dilution and one blank solution were used to generate liquid-phase calibration curve in the concentration range of 1 to 31 μg/l. After completing cold vapor mercury analysis to determine

the mass of mercury trapped in the impinger train, the concentration of the gas-phase mercury corresponding to the AAS absorption reading was determined using the following equation:

$$C_{Hg} = M / (Q \times t) \qquad (3\text{-}3)$$

Where C_{Hg} = concentration of gas-phase mercury ($\mu g/m^3$)

M = mass of mercury in the impinger train (μg)

t = time of impinger run (min)

Q = gas flowrate (l/min)

Once the AAS was calibrated, a simpler method was used for AAS spot check and accuracy of the system using Jerome Calibration Vessel (Arizona Instrument Corporation, Phoenix, AZ), a thermos bottle containing liquid mercury capped with a rubber stopper. This rubber stopper contained a narrow slit through which a syringe was inserted to extract a given volume of mercury vapor from the thermos maintained at room temperature. The mercury vapor from the thermos was injected into a hollow quartz cell of the AAS through a rubber septum. Since the concentration of vapor-phase mercury at a given temperature in the thermos can be calculated from the table supplied by manufacturer, the mercury concentration in the quartz cell can be easily calculated. The calibration curve obtained using this method corresponded very well (within 1%) to one obtained by the impinger technique.

4.0 RESULTS AND DISCUSSION

4.1 A combined Study Using TPD and ODR Techniques: Acetone Adsorption and Desorption on HOPG Surface

This study reports the adsorption and desorption of a model adsorbent representative of a volatile polar organic compound (acetone) on a model carbonaceous surface (HOPG). Many environmental phenomena involving carbonaceous surfaces occur under conditions where standard UHV surface science techniques cannot be applied, e.g., atmospheric pressure. ODR and TPD experiments were performed to show that the strong correlation between ODR, determined in real time, and relative surface coverage, determined a posteriori by TPD, could be extended from metal surfaces to carbonaceous surfaces. Thus, it was established that ODR could be used quantitatively to determine coverage on carbonaceous surface under conditions where TPD cannot be employed. Acetone was chosen as the first adsorbate because it represents polar organics, it is easy to handle (e.g. dosing, fast pumping) and analyze, and there are numerous literature references regarding adsorption of acetone on a variety of surfaces.

4.1.1 Temperature Programmed Desorption (TPD)

The results of TPD experiments for 1000 K treated HOPG surfaces dosed with increasing acetone exposures are shown in the Figure 4-1, where the partial pressure of acetone (QMS signal) is plotted as a function of sample temperature. The area under each curve is proportional to the amount of acetone retained by the sample surface during the adsorption phase (surface

coverage). Each peak in the TPD spectra corresponds to the temperature of maximum desorption rate. In the lowest exposure data, until 7.5 L, only one peak is seen at 160-170 K. For exposures >7.5 L, two peaks are seen at 154-158 K and 160-165 K, respectively. For 15 Langmuir exposure, three peaks can clearly be seen at around 145 K, 156 K, and 164 K, respectively. The three characteristic peaks are still present at higher exposure with the lowest temperature peak growing the most. The high temperature peaks are located between 160 K to 170 K for all exposures.

Each TPD feature is associated with molecules desorbing from different surface layers in agreement with a literature report for acetone desorption from a graphitic layer on Pt(111). [105] The highest temperature peak (160-170 K) represents desorption from the monolayer. [68, 105] The second TPD peak (154-158 K) is associated with desorption from the bilayer.[105] The lowest temperature TPD peak (at about 145 K) represents desorption from the multilayer. [68, 105] Figure 4-2 illustrates the growth of the TPD area of the monolayer and bilayer peaks calculated by the best fit for each individual peak (deconvolution).[106] The dotted lines are the fitting curves assuming that adsorption follows Langmuir kinetics. The bilayer peak begins to grow after the first layer has reached about two thirds of its saturation coverage. The similarity of the slopes of the Langmuir fits for both monolayer and bilayer indicates that the sticking probabilities of acetone on the HOPG surface and on the monolayer are similar, because the slope of the TPD signal as a function of acetone exposure represent the sticking probability. The appearance of the multilayer peak in the TPD spectra (Figure 4-1), at about 13 L, indicates the point at which molecules begin to adsorb on the bilayer. Again, the multilayer peak appears before the bilayer feature has saturated. The data in Figure 4-2 indicate that the monolayer is about 80% complete and the bilayer is about 55% complete when the multilayer appears.

The data clearly suggest that the adsorbates grow according to a Volmer-Weber mechanism rather than a layer by layer mode, as discussed below.[107] Figure 4-3 illustrates the adsorption sequence for the proposed Volmer-Weber adsorption sequence. At low exposure, acetone molecules adsorb directly on the surface, in a monolayer state. The appearance of a second peak before the monolayer state is completely saturated suggests that, in addition to molecules binding on the HOPG surface, acetone molecules begin to bind to the monolayer, thereby creating a bilayer**.** As the bilayer feature grows, the monolayer feature continues to increase, though more slowly, indicating that there are still monolayer surface sites to be filled. The absolute coverage at which the bilayer and multilayer features appear can be estimated, in principle, from optical difference reflectance as discussed below.

The activation energy of desorption from the monolayer, bilayer and multilayer states can be estimated, as described by Witman et at.[108] For example, the thermal desorption spectra of the acetone multilayer state are described by a zero order rate law, because of the observed invariance of the leading edge of the TPD spectra to changes in the coverage of the adsorbate.[79] The activation energy for desorption can be calculated by fitting the Equation 2-3 (ln ($d\theta/dT$) versus 1/T) to Arrhenius plot of with n=0. The activation energy for desorption of the acetone multilayer from graphite was determined to be 31 ± 2 kJ/mol. The activation energy of the multilayer of acetone on HOPG is in agreement with the sublimation energy of acetone, 31 kJ/mol.[96, 109] Therefore, it can be concluded that multilayer growth of acetone on graphite is independent of substrate adsorbate interaction and that bulk molecular interactions dominate the behavior of this system because TPD spectra follows a common leading edge (zero order) and a good agreement of the activation energy and the sublimation energy means substrate adsorbate interaction is almost negligible.

4.1.2 Optical Differential Reflectance (ODR)

ODR experiments were performed by continuous exposure at 1.2×10^{-7} torr of acetone pressure with the HOPG sample at 91 K. Figure 4-4 shows the intensity change of p- and s-polarized light reflected from HOPG as a function of exposure. As the exposure increases, the intensity of p-polarized light increases while the s-polarized light intensity remains constant. The data clearly indicate that p-polarized light is much more sensitive to adsorption than s-polarized light. This confirms the use of p-polarized light as a "signal" and s-polarized light as a "reference".

Using equation 3-2, the ODR signal is plotted as a function of acetone exposure in Figure 4-5. The near linearity of the ODR with exposure suggests that overall acetone adsorption on graphite does not follow simple Langmuir adsorption kinetics because no saturation of signal can be observed. However, the individual monolayer and bilayer states do follow Langmuir adsorption kinetics as discussed with Figure 4-2. As can be seen in Figure 4-5, ODR signal increases linearly until about 7 L exposure (dashed line) at which point the bilayer has begun to grow and the slope of the ODR (solid line) becomes steeper. Even though the number of available sites for adsorption on graphite decreases as the coverage increases, the actual adsorption surface area increases since the acetone layers themselves provide sites for acetone adsorption (see Figure 4-3). Such behavior explains why the slope of the ODR signal and TPD area grow faster at higher coverage rather than saturating once the bilayer appears. The model for acetone adsorption on graphite in Figure 4-3 illustrates how the surface area available for adsorption can increase as adsorption occurs.

In order to validate ODR as a quantitative technique for adsorption analysis, the optical reflectivity change should correlate with coverage as determined from TPD. A plot of the ODR signal as a function of the integrated TPD area is shown in Figure 4-6. The linear correlation between the two signals is very good with R^2 of 0.995. The correlation of the ODR signal and the TPD area clearly demonstrates that ODR measures the surface coverage change induced by adsorption.

The reflectivity change can also probe the surface coverage during thermal desorption**.** Figure 4-7 (b) shows the ODR signal as the temperature of a surface previously exposed to 19 L of acetone is increased. There is a sharp drop of the ODR signal induced by acetone desorption. The magnitude of ODR signal decrease was similar to the ODR increase (about 1 %) during adsorption. The temperature at which the signal drop occurs corresponds to the temperature range at which desorption is observed in the TPD experiment. Because the light reflectivity can be changed as surface temperature changes, temperature-dependant reflectivity changes of the substrate itself must be accounted for. Therefore, it is essential to perform a background reflectivity scan as a function of temperature without adsorbate dosing to correct for such effects (Figure 4-7 (a)). This procedure also corrects for possible sample motion that might occur during heating due to different thermal expansion of different materials. By subtracting the temperature induced reflectivity change of the adsorbate-covered substrate from that of the clean substrate, the adsorbate induced ODR signal can be isolated.

TPD spectra measure the rate of desorption as a function of temperature ($d\theta/dT$).[108] Given the linear relation between the coverage and ODR signal (ODR signal $\propto$ coverage (θ)), the derivative of the ODR signal with respect to temperature, d(ODR)/dT, during desorption should be proportional to the rate of desorption. Thus, the rate of change of the ODR signal with

temperature should correlate with the TPD spectrum (dθ/dT). Figure 4-8 shows the comparison of the d(ΔR/R)/dT signal during the thermal desorption with the TPD spectrum for a surface dosed with 20 L of acetone. Good agreement of desorption peak location between the two curves provides additional evidence for the linearity of the ODR signal with coverage on carbonaceous surfaces. While the TPD clearly has better sensitivity, it can be expected that a more sophisticated modulation scheme could significantly improve the signal-to-noise ratio of the ODR measurement. TPD often detects molecules desorbed from surfaces other than actual sample. However, the ODR can isolate signal contributions from the sample support or other surfaces because it measures the light intensity directly from the sample surface. The ODR technique clearly demonstrates the ability to probe surface coverage changes on a carbonaceous surface *in-situ* and in real time.

The reflectivity change, $\Delta R = R(\theta)-R(\theta=0)$, induced by adsorption/desorption of a physisorbed species can be described by a three-layer model, as shown in Figure 4-9.[69] Figure 4-9 shows a schematic view of the three-layer model. The interface between the layers is considered planar. As acetone does not visible absorb light, the reflectivity change can be described by the following equation when the dielectric constant for the ambient media ε_1, and for adsorbate layer, ε_2, are real numbers, ε_3 is a complex number and $|\varepsilon_3| \gg 1$;[69]

$$\frac{\Delta R_s}{R_s} = \frac{8\pi d \cos\phi}{\lambda} \mathrm{Im}\left(\frac{\varepsilon_2 - \varepsilon_3}{\varepsilon_1 - \varepsilon_3}\right) \tag{4-1}$$

$$\frac{\Delta R_p}{R_p} = \frac{8\pi d \cos\phi}{\lambda} \mathrm{Im}\left[\left(\frac{\varepsilon_2 - \varepsilon_3}{\varepsilon_1 - \varepsilon_3}\right)\left(\frac{1 - (\varepsilon_1/\varepsilon_2\varepsilon_3)(\varepsilon_2 + \varepsilon_3)\sin^2\phi}{1 - (1/\varepsilon_3)(\varepsilon_1 + \varepsilon_3)\sin^2\phi}\right)\right] \tag{4-2}$$

where d is the adsorbate overlayer thickness, Im represents imaginary part, ϕ is the angle of incidence, and λ is the probe wavelength.[61] $R_{p,s}(\theta=0)$ and $R_{p,s}$ $(\theta\neq0)$ refer to the reflectivity of the clean and adsorbate covered surface for p- and s-polarized light, respectively. These equations suggest that p-polarized light is more sensitive to an adsorbate than s-polarized light. This was confirmed experimentally; s-polarized light exhibited almost no intensity changes during adsorption (Figure 4-4).

The acetone overlayer "thickness" for 7L exposure, the point at which the bilayer begins to grow, can be estimated using this model assuming that graphite, in a first approximation, is an optically isotropic substrate.[69] Using the following dielectric constants, 1.846 for acetone [96] and 5.0 + i8.4 for the substrate (graphite),[110] the ODR signal (0.35 %) in Figure 4-5 corresponds to a "thickness" of 5 ± 2 Å. The overlayer "thickness" at which the multilayer begins to grow is calculated from the ODR signal (0.65 %) for 13 L exposure to be 10 ± 3 Å. Errors in the film thickness estimation originate from the ODR noise and the accuracy of the incident angle measurement. The ODR "thickness" compares favorably to the thickness for a single layer estimated from the molecular simulation study that indicates that the locus of the first layer lies at about 3.5Å above the graphite, that of the second layer is located at 7 Å above the surface, and the third at 10.5 Å.[111]

4.2 ODR Investigation of Reversible and Irreversible Adsorption and Desorption: Propane Adsorption and Desorption on HOPG

Although temperature programmed desorption (TPD) is the most widely used surface analysis technique, there are several limitations due to the fact for example that the adsorption process must be irreversible. An *in-situ* surface probe may be needed to investigate reversible processes. The aim of the study is to demonstrate the ability of the ODR technique to monitor adsorption in situations where the TPD technique cannot be used. Propane adsorption on raw graphite (HOPG) was performed while the graphite surface was kept at 90, 95, 100, 105 and 110 K after heat cleaning at over 1270 K. The experimental results are supported by Monte-Carlo Simulations.[112] A detailed description of the simulation study is discussed elsewhere.[112] Propane was chosen as the adsorbate because it is a representative of non-polar organics and lower hydrocarbons that have received significant research attention.[78] However, through literature review, no experimental work has been done on the adsorption behavior of propane on graphite at low temperatures and vacuum pressure.

Both TPD and ODR experiments for propane adsorption were performed on HOPG. The TPD method has been used extensively for studying both chemisorption and physisorption and is considered to be very accurate for determining relative coverage. The ODR method, however, is not as widely used, especially for physisorption systems. In order to validate ODR as a quantitative technique the optical reflectivity change should correlate with coverage as determined from TPD. TPD area has been shown to be proportional to the surface coverage. Figure 4-10, a plot of the ODR signal and TPD area as a function of a common exposure, shows a good agreement between these techniques. Both the ODR signal and TPD area saturate at

around 8 Langmuir. The excellent correlation of the ODR signal and the TPD area indicates that ODR accurately measures the surface coverage change induced by monolayer adsorption. Excellent correlation between ODR and TPD measurements also indicates that the TPD spectra are free from contributions due to desorption from other surfaces in the chamber because ODR only probes a small area (<1 mm^2) in the center of the HOPG sample.[113]

The ODR measurements were performed to determine the reversibility of bilayer formation. The ODR signal change as a function of propane pressure at 90 K is provided in Figure 4-11. The different symbols on the figure describe the sequence of propane pressure adjustment and its adjustment direction (increase or decrease). The propane pressure was initially increased from UHV to about 5×10^{-6} torr (triangles) and then reduced to below 10^{-7} torr (squares). Finally, the propane pressure was increased to above 5×10^{-5} torr while the ODR signal was recorded. The initial signal growth in the lower pressure region, up to 2×10^{-7} torr, in Figure 4-11, suggests monolayer adsorption, as verified by TPD and simulations. The signal in the submonolayer regime does not represent an equilibrium condition. The coverage increases with increasing time as the pressure is increased from UHV to about 10^{-7} torr. Hence, the initial rise in coverage shown in Figure 4-11 reflects the kinetics of the dosing process. It can be assumed that the signal increase for propane pressures between 3×10^{-6} torr and 5×10^{-6} torr is induced by bilayer formation. The reversibility of bilayer formation can be clearly seen from the ODR signal decrease to the monolayer ODR signal level when the pressure is reduced to under 1×10^{-7} torr. However, the ODR signal remained at the level induced by the monolayer formation, although the propane pressure was reduced below the pressure at which monolayer formation occurred. Such behavior suggests that the propane monolayer adsorption is not reversible on the time scale of our measurements at 90 K. Bilayer formation is only observed above a critical

pressure of about 3×10^{-6} torr. Surface coverage increases when the rate of molecular adsorption is greater than the rate of desorption. The bilayer formation occurs at pressures over 3×10^{-6} torr, when the total flux of propane molecules is 6.31×10^{14} cm^{-2} sec^{-1} as calculated at room temperature by the kinetic theory.[114] Multilayer condensation is observed at over 1×10^{-5} torr of propane total pressure (circles). Multilayer formation is also reversible, as the ODR signal returned to the monolayer coverage when the pressure was brought back below 1×10^{-5} torr (not shown here).

Propane isotherms at about 91, 95, 100, 105, and 110 K were obtained in our experimental study. A distinct bilayer transition (apparently first order) was observed for the experiments at 105 K and below. No layering transition was observed in the 110 K experiment because the pressure was not high enough. The pressures at which the bilayer begins to form were found to be about 2.4×10^{-6}, 2.3×10^{-5}, 7×10^{-5}, and 2.4×10^{-4} torr, for 91, 95, 100, and 105 K, respectively. These transition pressures are average values from several runs. The estimated uncertainty in the absolute pressure at which the bilayer forms is about 30%, while the uncertainty in the relative temperature is about 1 K. In order to compare the adsorption behavior of propane on HOPG at different surface temperatures, ODR experiments were performed at 90 K, 100 K and 105 K along with data from GCMC simulations and the results are plotted as a function of propane pressure in Figure 4-12. The observation of the formation of the bilayer and multilayer was enabled by the use of ODR. Although temperature programmed desorption (TPD) is a widely used surface analysis technique, it is not suitable to observe the states that are reversibly populated, i.e., states that require high ambient pressure to be observed. The reduction in pressure required to perform TPD de-populates bilayer and multilayer states, hence the absence of the corresponding peaks in TPD spectra on Figure 4-13.

Figure 4-12 describes the adsorption isotherm data for propane on HOPG at 91 K determined from experiments and simulations. The experimental adsorption loadings were measured in arbitrary units and converted to μmol/m^2 by matching the monolayer loading with the simulation data. Because the relative adsorbed amount measured experimentally are accurate, the good agreement between experiments and simulations for the second layer loadings indicate that simulations accurately predict relative coverages in the first and second layers. The position of the first to second layer transition on the pressure axis determined from experiments and simulations are in remarkable agreement. The agreement, however, is probably fortuitous because of the experimental difficulty in measuring the absolute pressure accurately. Furthermore, transition pressures are very sensitive to substrate temperature. While relative temperature is accurate to about one degree K, absolute temperature is measured less accurately. It was not possible to observe a transition from zero loading to the first layer in any of the simulations. Virtually complete monolayer coverage at the lowest pressures simulated (about 2×10^{-8} torr) is obtained, indicating that the 0-1 transition must occur at pressures lower than 2×10^{-8} torr. The apparent 0-1 layering transition seen in the experimental data (e.g., Figure 4-12 (a) and (b)) is the result of kinetic effects. The pressure in the UHV chamber was rapidly increased before the monolayer had a chance to form completely and the experimental data below the monolayer coverage in Figure 4-12 (a) do not reflect true equilibrium. The kinetic nature of the ODR data can also be inferred from the data in Figure 4-11, which shows that the first layer remains intact upon reduction of the pressure. Indeed, we find that the first layer cannot be removed over a reasonable time by evacuating the chamber; the substrate must be heated to remove the first layer (see Figure 4-13). These data reflect the dynamic nature of adsorption

experiments, i.e., it takes a finite time to form a monolayer at a fixed pressure. The simulations, however, reflect equilibrium (or metastable) conditions.

Experimental data for T = 95, 100, 105 K and simulation isotherms for T = 100 and 105 K are shown in Figure 4-12 (b). The 1-2 layering transition pressures at 100 and 105 K from simulation and experiment do not agree as well as in the 91 K case, but they are in good qualitative accordance. The relative coverages in the first and second layer are in excellent agreement.

As noted above, the desorption of the second layer of propane is reversible, i.e., it can be achieved by lowering the pressure, whereas the monolayer must be heated to be removed. The fact that monolayer desorption is an activated process means that we can use TPD to probe the energetics. We used the equation (2-4) to calculate the activation energy of desorption from TPD experiments[89, 108]

A series of TPD spectra for propane dosed at 90 K on HOPG are shown in Figure 4-13. A single peak appears around 115 K. The propane TPD spectra grow with a common leading edge and abrupt trailing edge, indicating zero order desorption.[75] Using zero order desorption kinetics, the activation energy for desorption of propane on HOPG is estimated to be 30 ± 2 kJ/mol (Figure inserts). The uncertainties arise in part from the accuracy of temperature measurements. The heat of vaporization of propane at its normal boiling point (230.9 K) is 19.04 kJ/mol,[96] while integration of the heat capacity yields a value of 24 kJ/mol for the heat of vaporization at 100 K.[96, 115] This is smaller than the calculated activation energy and is consistent with the strong solid-fluid interaction for adsorbed propane. There is no evidence in the TPD spectra of bilayer or multilayer formation under present experimental conditions.

The isosteric heat of adsorption can be obtained from the following relationship, the Clausius-Clapeyron equation[84]

$$\frac{d(\ln P)}{d(1/T)} = -\frac{\Delta H}{R} \qquad (4\text{-}3)$$

Where ΔH is the heat of adsorption, T is the temperature at which the layer formation occurs, P is the pressure and R is the ideal gas law constant (8.314 kJ/mol). Plots of ln P as a function of reciprocal absolute temperature at constant coverage are called adsorption isosteres and the isosteric heat of adsorption is determined by their slopes. Experiments performed at five temperatures (91, 95, 100, 105 and 110 K) allow determination of ΔH. The average pressure where the second layer just begins to form at each temperature was used to construct a single isostere. For experiments at 110 K second layer formation was not observed at pressures up to 2 $\times 10^{-4}$ torr, consistent with the simulations showing that the second layer forms at a pressure of about 5 $\times 10^{-4}$ torr. The isosteres procedure can be applied to the isotherms calculated from simulations and a value of ΔH can be obtained.

The heat of adsorption computed from experimental and simulation data are plotted in Figure 4-14. The experimental values in Figure 4-14 represent the average of several isotherm measurements and the error bars were estimated based on the scatter in the experimental data. The values of isosteric heat at bilayer formation determined from experimental and simulation data are in excellent agreement. The experimentally determined value of ΔH is 23 ± 2 kJ/mol. The isotherms computed from Monte-Carlo simulation agree well quantitatively with ODR experimental results in terms of the location of pressure at which bilayer of propane occurs. In addition, molecular simulations estimated heat of adsorption of propane bilayer of 24 ± 1 kJ/mol,

which is in good agreement with experimental data. Therefore, this study clearly showed that ODR is suitable for investigating reversible adsorption phenomena in real time and over a wide pressure range.

4.3 The Effects of Surface Functional Groups on Adsorption and Desorption of Acetone on Carbonaceous Surfaces

A series of experiments was designed to probe the role of surface chemical heterogeneity on the adsorption process on carbonaceous surfaces. The objective of this study was to investigate the role of air-formed surface chemical functional groups on a model carbonaceous surfaces (HOPG, highly oriented pyrolytic graphite) on the adsorption and desorption of acetone as a representative of polar organic compounds.

The gas evolution profiles as a function of temperature during surface heat treatment of a-HOPG are displayed in Figure 4-15. Heat treatment clearly leads to desorption of 16, 18, 28 and 44 atomic mass unit (amu) containing species, probably H_2O, CO and CO_2 related compounds, at temperatures above 500 K. It can be seen from Figure 4-15 that there is no re-appearance of these features in the ~24 hours that elapse between each successive heat treatment. The gas evolution only starts at temperatures higher than previous day's maximum treatment temperature. This result can be compared to the study of thermal desorption of spectroscopy of the heterogeneous surface of activated carbon.[116] It was found that the decomposition of the surface oxides on carbon, yielding CO and CO_2, occurs at temperatures above 520 K and that outgassing above 1273 K is required to remove essentially all functional groups. In order to

verify that gas desorption during heat treatment originated from the HOPG samples and not other parts of the sample holder, control experiments were performed where the air-cleaved HOPG sample was replaced by a gold coated Ta sample (10×10×0.05 mm). Heat treatment to over 873 K resulted in no significant gas desorption.

TPD spectra for surfaces dosed at around 120 K with increasing acetone exposures after the desired heat treatment are shown in Figure 4-16, where the partial pressure of acetone (QMS signal at 43 m/e) is plotted as a function of the sample temperature. For all exposures after 473 K heat treatment, a single desorption peak, with a common leading edge, appears at around 130 K (Figure 4-16 (a)).

For 673 K heat treatment (Figure 4-16 (b)), the TPD spectra at the lowest exposure, until 5 L, consist of only one peak at around 155 K. For exposures above 5 L, two peaks are seen at about 147 K and 155 K. For 7 L exposure, three peaks can clearly be seen at around 137 K, 147 K, and 155 K. Each TPD peak is likely associated with molecules desorbing from different surface layers.[111] The highest temperature peak for the TPD spectra after 673 K heat treatment (150-155 K) represents desorption from the monolayer, i.e. acetone bound to HOPG surface.[61, 105] The second TPD peak (around 147 K) is associated with desorption from the bilayer.[105] The lowest temperature TPD peak (at about 137 ^{o}) represents desorption from the multilayer.[61, 105] These three characteristic peaks are also present at higher exposures. The two high temperature peaks saturate while the lowest temperature peak grows with increasing exposure.

TPD spectra after 873 K heat treatment (Figure 4-16 (c)) shows the same three peaks at temperature identical to those in TPD spectra after 673 K heat treatment. The acetone exposure required for monolayer peak saturation, as well as the magnitude of this peak, increases as the heat treatment temperature increases. It can be seen in Figure 4-16 that the monolayer saturates

at 5L for 673 K, between 7 and 10L for 873 K and around 10L for 1073 K and greater heat treatments, respectively. The saturation exposure for the bilayer also increases as the temperature of the heat treatment increases.

Essentially identical results to those reported herein were obtained using an HOPG sample manufactured by a different company (Grade ZYA, Advanced Ceramics Co). Heat treatment leads to similar gas evolution profiles as shown in Fig 4-15. The acetone TPD spectra were almost identical to those shown in Fig 4-16. Exposure of HOPG samples treated to 1323 K to ambient laboratory air results in the regeneration of oxygen functionalities and TPD behavior similar to that depicted in Figures 4-15 and 4-16 is observed. This suggests that the experimental observations reflect intrinsic properties of HOPG, rather than contamination of the HOPG surface during production or preparation.[117]

The evolution of each feature observed in the acetone TPD (Figure 4-16) was investigated by deconvolution of the TPD spectra, the separation of each individual peak by curve fitting. The integrated TPD area for each layer corresponds to the relative amount of acetone molecules adsorbed at 25 L exposure and is plotted as a function of heat treatment temperature in Fig 4-17. As can be seen in Figure 4-16, both the monolayer and bilayer are almost saturated at 25 L in all cases. As the sample is treated at higher temperature, the amount of acetone adsorbed directly on the HOPG surface (monolayer) increases as well as the amount adsorbed on the monolayer of acetone (bilayer). Both features appear to level off for heat treatment above 1000 K.

The results shown in Figures 4-16 and 4-17 suggest that the removal of the surface functional groups from HOPG by heat treatment creates a surface that is representative of a clean HOPG surface for acetone adsorption. The TPD spectra are then almost identical to acetone TPD

from a single graphitic layer grown on Pt(111).[105] The higher temperature associated with the monolayer feature suggests that acetone molecules bind more tightly on the clean HOPG surface than on the functional groups that are initially present on the air cleaved surface. The saturation of the monolayer adsorption uptake of acetone, Figure 4-17, for outgassing temperatures above 1000 K suggests that a heat treatment temperature of at least 1000 K is needed to remove functional groups from the surface and prepare a clean HOPG surface.

It is unlikely that HOPG offers "entry ports" for acetone molecules since intercalation, the adsorption of adsorbate into the layers of HOPG, is unlikely given the size of the molecule and the pressures employed in this investigation. Furthermore, intercalation of acetone molecules should not result in saturation of all HOPG layers with such low acetone exposures, less than 15 L after 1273 K heat treatment. The similarity of TPD spectra for heat treatment above 1000 K (Figure 4-16 (d) and 4-16 (e)) and those from a previous study involving desorption of acetone from a monolayer of graphitic carbon grown on a Pt(111) surface,[105] further supports the hypothesis that acetone molecules do not intercalate into HOPG layers, because a monolayer of graphitic carbon on Pt does not offer any layers for intercalation.

To investigate possible changes in acetone uptake capacity as a function of heat treatment temperature, the total TPD area at 25 L acetone exposure is shown in Figure 4-18. In spite of the changes in the area for each individual TPD feature, the total TPD area at constant exposure remains approximately constant for all heat treatments. This indicates that the sticking probability of acetone on clean HOPG and HOPG decorated with air-formed functional groups is similar. The contribution from each individual TPD peak changes with the removal of functional groups, while the overall adsorption remains constant. On the other hand, the TPD area for low exposure (e.g., 5 L) decreases, by almost a factor of two, as the pre-treatment temperature

increases (inset in Figure 4). Such behavior clearly demonstrates that the sticking probability of acetone on functionalities or an acetone layer already present on the HOPG surface is higher than on a functional group-free HOPG surface.

Previous studies documented quite different behavior for adsorption of a non-polar organic, propane, on HOPG following heat treatment.[117] In the case of propane, the initial uptake capacity was very low. Heat treatment to over 1270 K increased the total adsorption capacity on HOPG by over an order of magnitude. This indicates that the air-formed functional groups on HOPG interact more favorably with polar adsorbate compared to non-polar adsorbates. The higher adsorption capacity of carbonaceous surfaces for polar organic molecules (acetone) than non-polar (propane) is consistent with reports that air-formed functional groups are also polar, e.g., carboxyl group.[10] The presence of polar oxygen-containing functional groups is not completely unexpected because carbonaceous surfaces exposed to ambient conditions typically contain the kind of functionalities encountered in this study.[118] However, it is surprising for HOPG, which is believed to contain very little functionality.

The energy of acetone desorption from the clean HOPG surface (monolayer of acetone) can be determined through the analysis of the desorption rate ($-d\theta/dT$), which is commonly described by Equation (2-4). Figure 4-19 shows both experimental and simulated TPD for acetone exposure from 1L to 7L. The best fits of Equation (2-4) to experimental data shown in Fig 4-19 are obtained with $n = 1$, a pre-exponential factor of $10^{20\pm1.5}$ sec^{-1}, an activation energy of 55.5 ± 3.0 kJ/mol and intermolecular interaction parameter of 0.045 $monolayer^{-1}$ for the acetone monolayer on the clean HOPG surface. The pre-exponential factor obtained from this fit is much higher than the usually assumed value of 10^{13} sec^{-1}.[75] However, the use of a 10^{13} sec^{-1} pre-exponential factor in the TPD peak simulation procedure failed to achieved reasonable fits of

experimental TPD data, as shown in insert (a) on Fig 4-19. The 10^{-13} sec^{-1} pre-exponential factor results in a TPD peak twice as broad as that observed experimentally. One may claim that the monolayer of acetone grows with zero order due to similar leading edge of TPD spectra at different exposures. However, the fitting using zero order reaction fails to predict the tailing feature of the experimental data as shown in insert (b) on Fig 4-19.

The desorption parameters for the second layer (bilayer) can also be estimated using coverage dependant first order simulation. Monolayer and bilayer peaks are separated by deconvolution and are fitted separately using the same simulation procedure as that employed for acetone monolayer. The best fits to experimental data were obtained with n = 1, a pre-exponential factor of $10^{21.6\pm\ 1.5}$ sec^{-1}, an activation energy of 51.5 ± 3.0 kJ/mol and an intermolecular interaction parameter of 0.004 for the acetone bilayer on the clean HOPG surface.

Thermal desorption spectra of acetone multilayer state are usually described by a zero order rate law because of the observed invariance of the leading edge of the TPD spectra to changes in the initial coverage of the adsorbate and a sharp drop after reaching maximum desorption rate.[77] The activation energy for desorption can be calculated by fitting the intensity profile to Equation (2-4) with n = 0 and $\alpha = 0$. The activation energy for desorption of acetone multilayer from graphite was determined using this procedure to be 31 ± 2 kJ/mol This is in agreement with the sublimation energy of acetone, 31 kJ/mol.[96, 109, 119] The excellent agreement between the multilayer desorption energy determined in this study and the bulk enthalpy of sublimation suggests that relative sample temperature readings are quite accurate (± 2 K) and that the adsorbate is pure. The results obtained in this study can be compared to the TPD spectra of other polar organic adsorbates (alcohols and ethers) on HOPG, which showed first order monolayer and zero order multilayer desorption peaks.[120, 121]

In addition to using the simulation method described above to assess the desorption parameters, acetone TPD experiments were performed using different heating rates at 7L acetone exposure to independently determine acetone desorption parameters.[89] Figure 4-20 illustrates how the TPD peak amplitude grows and the peak location shifts to higher temperature as the heating rate increases. These experiments allow the determination of the pre-exponential factor and activation energy using Redhead first order kinetics, described by Equation (4-4).[89]

$$\frac{E_d}{RT_p^{\,2}} = \left(\frac{\nu}{\beta}\right) \exp\left(-\frac{E_d}{RT_p}\right) \qquad (4\text{-}4)$$

where, T_p represents temperature where the maximum desorption rate occurs.

The Equation (4-4) can be transformed to Equation (4-5) to allow direct estimation of exponential factor and activation energy.[75, 102]

$$\nu = \frac{\beta\, E_d}{RT_p^{\,2}} \exp\left(\frac{E_d}{RT_p}\right) \qquad (4\text{-}5)$$

The procedure for the determination of activation energy and pre-exponential factor involves plotting $\ln(\beta/T_p^2)$ versus $1/T_p$. This yields a straight line with a slope of $-E_d/R$, as shown in the insert on Figure 4-20. A linear regression performed on the data yielded activation energy of 57.7 ± 2.5 kJ/mol for 7 L and 54.9 ± 2.5 kJ/mol for 3 L, and a common pre-exponential factor of $10^{19\pm1}$ sec^{-1}. Both methods for the analysis of acetone desorption kinetics parameters resulted in very similar values for the activation energy and pre-exponential factor, which gives confidence in the data reported here. The pre-exponential factor obtained from both simulation and experimental methods is much higher than the typical value of 10^{-13} 1/sec assumed in TPD

analysis.[89] However, the high pre-exponential factor for organics on HOPG surface can be found in a study which investigated desorption kinetics of n-alkanes (n > 5) from HOPG.[75, 76] This study also compared pre-exponential factor estimated by first order simulation and experiments using variable temperature ramping rate in TPD studies and showed high values of ν in the range from 19^{19} to 10^{20} sec^{-1}.

4.4 The Effects of Surface Functional Groups and Topological Heterogeneity on Propane Adsorption and Desorption on Carbonaceous Surface

This section discusses the adsorption and desorption of a model adsorbent representative of non-polar organic compounds (propane) on model carbonaceous surfaces. Both raw and plasma oxidized HOPG were used to investigate the effects of chemical functional groups and surface morphology on the adsorption/desorption behavior of propane. Considering that industrial sorbents like activated carbon contain chemical functionalities as well as topological surface roughness, understanding the role of these heterogeneities on adsorption and desorption is extremely important in terms of producing "better sorbents" for a given purpose. By introducing chemical and morphological heterogeneity on homogenous HOPG surface, this approach can provide a better understanding of the adsorption/desorption characteristics of carbonaceous surfaces used in practice (e.g., activated carbon that contains high chemical and morphological heterogeneity).

4.4.1 Adsorption /Desorption on Air-Cleaved HOPG (a-HOPG)

A series of TPD spectra for propane dosed at 90 K on air-cleaved HOPG following heat treatment to various temperatures is shown in Figure 4-21. A peak appears around 115 K in all cases and saturates at 3L for 673 K, 7L for 873 K and 8L for 1073 K and higher heat treatments, respectively. The TPD peak for air-cleaved HOPG treated at 473 K is barely detectable even when multiplied by 10 on this scale. As the heat treatment temperature increases, the propane TPD desorption peak height increases at equivalent exposure levels.

Figure 4-22 illustrates the integrated TPD areas, corresponding to the relative amount of propane molecules adsorbed at 25 L exposure for air-cleaved HOPG and plasma-oxidized HOPG, as a function of the heat treatment temperature. A 25 L exposure results in saturation for all heat treatments reported here. The results depicted in Figure 4-15 suggest that oxygen-containing functional groups exist on the air-cleaved HOPG surface and that they are removed by thermal treatment. The results shown in Figures 4-21 and 4-22 suggest that the removal of these functional groups increases the number of accessible adsorption sites for propane molecules. The results also suggest that propane, a non-polar organic, has an unfavorable interaction with the naturally existing polar functional groups on air-cleaved HOPG prior to heat treatment. The saturation of the adsorption uptake seen in Figure 4-22 for outgassing temperatures above 1173 K suggests that heat treatment at $T \geq 1173$ K is needed to clean the air-cleaved HOPG surface for alkane adsorption.

Exposure to laboratory air for 24 hours results in the reappearance on HOPG of similar types and quantities of functional groups as those that have been removed by heat treatment of air cleaved HOPG. This is revealed by the observation that the surface capacity for propane

adsorption is initially low and that heating to 1273 K results in evolution of the same fragments as observed from air cleaved HOPG, resulting in, once again, a factor of 20 increase in propane adsorption capacity. This behavior suggests that these oxygen-containing surface functionalities result from the interaction of the freshly cleaved or vacuum heat treated surface with air.

Interestingly, qualitatively similar behavior was seen in the study of xenon adsorption on carbon nanotubes.[52, 53] Thermal treatment over 600 K leads to the desorption, of oxygen containing functional groups, which are believed to block the entry ports of the nanotubes, without change of the molecular structure of the nanotubes. The removal of the blocking functional groups enhances the capacity of the carbon nanotubes for xenon uptake.[53]

Propane TPD spectra grow with a common leading edge for all heat treatments, indicating zero order desorption[75]. Using zero order desorption kinetics, the activation energy for propane desorption on HOPG is estimated to be 30 ± 2 kJ/mol, which represents a reasonable agreement with another study of n-alkane adsorption on HOPG[76]. Uncertainties in the estimation of activated energy arise in part from the accuracy of temperature measurements. The location of the thermocouple in this experimental system is restricted by the fact that it cannot be spot-welded to HOPG. The calculated activation energy is about 25 % greater than the heat of vaporization of propane of 23.9 kJ/mol at 100 K as shown in appendix.[96, 115] The observations that the shape of the TPD spectra does not change with heat treatment temperature, the increasing propane uptake subsequent to each heat treatment temperature, and the invariance of the activation energy with each heat treatment step verifies that little adsorption occurs at 90 K at sites blocked by chemical functional groups. It is very likely that chemical functional groups on HOPG are polar species (e.g., quinone, carbonyl or carboxylic acid) and that adsorption of a non-

polar organic (e.g., propane) is hindered by their presence on the surface. This is consistent with the well-known immiscibility of polar and non-polar solvents, e.g., oil and water.

The magnitude of the desorption energy suggests that the interaction between propane and the clean HOPG surface is greater than the interaction between propane molecules. There is no evidence of bilayer or multilayer formation under the present experimental conditions, because ambient pressures in excess of 10^{-6} torr are necessary for propane bilayer formation at 90 K.[112]

The propane adsorption capacity increase of air-cleaved HOPG after high temperature heat treatment is highly reproducible from sample to sample. During thermal treatment to 1050 K of air-cleaved HOPG from Advanced Ceramics, the desorption of gases containing 16, 18, 28 and 44 amu fragments was also observed in similar temperature regions to those evolved from the HOPG sample supplied by SPI. TPD experiments using air-cleaved HOPG from Advanced Ceramics also verify that HOPG has almost no propane adsorption capacity after 473 K heat treatment and that its ability to adsorb propane increased by over an order of magnitude after heat treatment to 1050 K.

4.4.2 Adsorption/Desorption on Plasma-oxidized HOPG (p-HOPG)

An important objective of this study was to understand the role of chemical and topological heterogeneity on adsorption and desorption on carbonaceous surfaces. In order to introduce defect sites and etch pits on HOPG, an air-cleaved HOPG sample was subjected to plasma treatment at controlled oxygen pressure**.** It has been shown previously that high temperature oxidation in air creates low density (< 1% by surface area) of monolayer deep etch

pits at existing defects of HOPG, while maintaining the flatness of the graphite surface[102, 122-125]. Plasma oxidation, however, creates mechanical damage on initially flat surface that augments pre-existing defect sites[102]. Plasma oxidation etches the surface, resulting in highly roughened surfaces confirmed by our AFM images[102].

Similar features to those shown in Figure 4-15 evolve during the heat treatment of plasma-oxidized HOPG as shown in Figure 4-23. Exposure of plasma-oxidized HOPG to air for about 24 hours results in essentially complete recovery of these features while the amount of the desorption of each detected gas compound and their peak location is varies somewhat. This suggests that the oxygen-containing groups do not result from impurities incorporated during sample preparation or manufacture.

The effects of surface morphology on adsorption are depicted in Figure 4-24, which compares TPD spectra from air-cleaved and plasma-treated HOPG at low propane exposure (< 3L) after heat treatment at 1173 K. TPD spectra for air-cleaved HOPG below 3 L propane exposure consist of a single peak with a leading common edge. On the other hand, for plasma-oxidized HOPG, it consists of two peaks, at around 120 K and 175 K, which both grow together with propane exposure. The growth of the lower temperature peak with exposure resembles that observed for the air-cleaved HOPG except that the peak height is about a factor of 5 lower. The higher temperature peak shifts to lower temperatures with increasing exposure.

It is reasonable to assume that the TPD spectra observed on p-HOPG are a consequence of the defects generated by plasma treatment. These defects provide adsorption sites with stronger binding energy as indicated by the higher temperature peak. These sites do not exist on air cleaved HOPG. The downward shift in peak temperature with increasing exposure suggests sequential filling of the defect sites, with the higher binding energy sites being filled first. This

behavior also suggests significant mobility of adsorbed species enabling them to sample all the sites. In addition, the TPD areas for plasma-oxidized HOPG are always greater than those for the air-cleaved HOPG under identical exposure conditions, as shown in Figure 4-25. Hence, the capacity for propane adsorption on plasma-oxidized HOPG is greater than that for air-cleaved HOPG. Plasma-oxidized HOPG has pits that are several tens of layers deep, thereby providing access to many more graphite layers than air-cleaved HOPG. Control experiments with a gold coated Ta sample indicate that the quantity of propane desorbed from a gold-coated Ta sample is similar to that desorbed from the heat-treated air-cleaved HOPG. These results suggest that no propane intercalation occurs under the experimental condition used in this study. The pits would provide access to many more layers than air cleaved HOPG. Therefore, the observed increase in uptake capacity of plasma-oxidized HOPG of about 50% is most likely associated with the increased surface area provided by the topologically heterogeneous plasma-oxidized HOPG sample.

The energy of propane desorption from the clean HOPG surface for high temperature peak can be determined through the analysis of the desorption rate (-dθ/dT), which is commonly described by Equation (4-6)[76]

$$-\frac{d\theta}{dT} = \frac{\nu}{\beta}\theta^{n}\exp\left(-\frac{E_d(1+\alpha\theta)}{RT}\right) \qquad (4\text{-}6)$$

where, ν is the pre-exponential factor, θ is the adsorbate coverage, β is temperature ramping rate (dT/dt), n is the order of the desorption process, and E_d is the activation energy for desorption at zero coverage.[76] The variable α is an intermolecular interaction parameter. Positive values of α

reflect attractive intermolecular interactions and negative values of α reveal repulsive intermolecular interactions.

After numerous trials to generate a reasonable fit of experimental data, it was decided that a simple first order kinetics never describes this high temperature peak properly because of significant surface heterogeneity caused by plasma oxidation. It was therefore decided to insert a pseudo-parameter ($\gamma\theta^2$) into the ($1+\alpha\theta$) term to better model the coverage dependence of the activation energy for desorption and to improve the quality of the fit, as follows,

$$-\frac{d\theta}{dT} = \frac{\nu}{\beta}\theta^{n} \exp\left(-\frac{E_d(1+\alpha\theta+\gamma\theta^2)}{RT}\right) \qquad (4\text{-}7)$$

The lineshape simulation of the high temperature propane peak and average heat of adsorption for both low and high temperature peak are shown in Figure 4-26. The main purpose of this phenomenological analysis is to demonstrate that the average binding energy of propane from defect sites created by plasma oxidation is higher than that from basal plane of HOPG and that there is considerable heterogeneity in the sites generated by plasma oxidation.

As shown in Figure 4-25, the TPD areas for plasma-oxidized HOPG are always greater than those for the air-cleaved HOPG under identical exposure conditions. Hence, the capacity for propane adsorption on plasma-oxidized HOPG is greater than that for air-cleaved HOPG. As discussed earlier, the observed increase in uptake capacity of plasma-oxidized HOPG of about 50% is most likely associated with the increased surface area provided by the topologically heterogeneous plasma-oxidized HOPG sample.

4.5 Adsorption and Desorption of Mercury on Model (HOPG) and Real (activated carbon) Carbonaceous Surfaces

This section compares adsorption and desorption of gas-phase elemental mercury on real and model carbonaceous surfaces. The investigation of elemental mercury adsorption is carried out using both highly oriented pyrolytic graphite (HOPG) as a model carbonaceous surface in well-controlled UHV condition and coal based activated carbon (BPL) in fixed bed conditions. It is clear that there are major differences between graphite and other carbonaceous sorbents with regards to inorganic impurities (ash content) and morphology. Therefore, attempts will be made to modify the pore structure and chemical heterogeneity (surface functional groups) of HOPG to capture the essential features of porous carbon because most researchers believe that these are the key surface properties influencing adsorption and catalysis by carbonaceous sorbents.[83, 126] Carefully selected thermal and chemical modifications of graphite and other sorbents would aim to delineate the importance of these surface properties in both adsorption and catalysis. (See Figure 2-3)

4.5.1 UHV studies with HOPG

A series of TPD experiments were carried out to investigate the impact of oxygen-containing functional groups on mercury adsorption and desorption from chemically modified HOPG surface. Figure 4-27 shows a series of TPD spectra for mercury dosed at 100 K on air cleaved HOPG sample following heat treatment to 473 K and 1273 K. A mercury TPD desorption peak appears around 200 K in both cases. It increases in height and width with an

increase in exposure levels. The peak did not saturate up to 20 L exposure and its location tends to shift to higher temperature with an increase in exposure.

The energy of mercury desorption from HOPG can be determined through the analysis of the desorption rate ($-d\theta/dT$), which is commonly described by Equation [102](4-4). Figure 4-28 is one example showing experimental and simulated TPD peaks for mercury exposure at 20L for a 1273 K treated a-HOPG sample. The best fit of Equation (4-4) to all experimental data shown on Figure 4-28 was obtained using 1st order kinetics, a pre-exponential factor of $10^{18\pm1}$ sec^{-1}, an average heat of adsorption of 82 ± 3 kJ/mol and an intermolecular interaction parameter of 0.003. Uncertainties arise in part from the accuracy of temperature measurements because location of the thermocouple in the experimental system is restricted by the fact that it cannot be spot-welded to HOPG. The calculated activation energy is only about 25 % greater than the heat of sublimation of mercury of 64.3 kJ/mol at 200 K.[96, 115] It can be concluded that mercury adsorption on HOPG under the experimental conditions used in this study occurs exclusively through physisorption.[127]

Figure 4-29 illustrates the integrated TPD areas, which correspond to the relative amount of adsorbed mercury, as a function of mercury exposure for both air cleaved HOPG samples. These results indicate that the heat treatment of HOPG at 1273 K causes some increase in the amount of mercury adsorbed under the experimental conditions used in this study. Previous studies demonstrated that heat treatment of HOPG leads to desorption of oxygen containing functional groups at temperatures above 500 K and that there is no re-appearance of these functionalities over a 24 hour period that elapses between successive heat treatments in UHV condition.[117] Similar behavior was demonstrated earlier for graphitized carbon fiber[128] and activated carbon[116], which demonstrated that outgassing above 1273 K is required to remove

essentially all functional groups. Therefore, it can be concluded that the increase in mercury adsorptive capacity of HOPG after 1273 K heat treatment was caused by the removal of chemical functionalities from the surface. Similar behavior was observed for the adsorption of propane on HOPG[111] and xenon on single wall carbon nanotubes.[52, 53] Propane, a non-polar organic, has unfavorable interactions with functional groups that exist on air-cleaved HOPG. Heating to 1273 K removed these functionalities and resulted in over an order of magnitude increase in propane adsorption capacity. The degree of the increase in mercury adsorption capacity upon heading HOPG to 1273 K was significantly lower than that observed for propane indicating stronger interaction between surface functional groups and non-polar organic molecules than metallic atoms.

An important objective of this study was to understand the role of topological heterogeneity on adsorption and desorption on HOPG under UHV conditions. In order to introduce defect sites and etch pits on HOPG, an air-cleaved HOPG sample was subjected to plasma treatment at controlled oxygen pressure**.** It has been shown that high temperature oxidation in air creates low density (< 1% by surface area) of monolayer deep etch pits at existing defects of HOPG, while maintaining the flatness of the graphite surface.[102, 122, 123, 129] Plasma oxidation, however, creates mechanical damage on initially flat surfaces that augments pre-existing defect sites.[102] Plasma oxidation etches the surface, resulting in highly roughened surfaces as confirmed by AFM measurements.[102] As shown in Figure 3-8, the air-cleaved HOPG (Figure 3-8 (a)) shows a clean and flat surface except for a few steps of ~2.5 nm height. A significant density of defects (dark spots in Fig 3-8 (b) and (c)) is observed on the 20 min plasma-oxidized HOPG surface (20-p-HOPG). Most defects are around 100 nm in diameter, and from ~1 to ~10 nm in depth. Plasma oxidation clearly results in the formation of topologically

heterogeneous surface distinct from the topologically homogeneous air-cleaved surface. Longer exposure to plasma oxidation does not lead to essential changes in the morphology of HOPG samples. Figure 3-8 (d) illustrates an increase in defect diameter (from ~100 to 500 nm) and depth (from ~ 50 to 200 nm) following 90 min plasma oxidation (90-p-HOPG), a commonly observed behavior.[102]

The 20 min plasma-oxidized HOPG and 90 min plasma-oxidized HOPG samples were subjected to heat treatment at 1273 K before mercury exposure to ensure that they contain no chemical functionalities and that only the impact of topological heterogeneity on mercury uptake is studied. Figure 4-30 shows a series of TPD spectra for mercury dosed at 100 K on plasma oxidized HOPG, while Figure 4-31 compares relative amounts of mercury adsorbed on virgin and plasma oxidized samples.

The impact of topological heterogeneity on elemental mercury adsorption can be evaluated by comparing TPD spectra for 1273 K treated a-HOPG (Figure 4-27 (b)) to those shown in Figure 4-30. The changes in the TPD spectra resulting from the difference in topology caused by plasma oxidation are minimal. There is no evidence that the defect sites caused by plasma treatment created new adsorption sites for mercury under the experimental condition used in this study because all desorption peaks appear at almost identical temperature. In addition, the heat of adsorption on plasma-oxidized samples, which was also estimated using coverage dependant first order kinetics, is within the error range of the heat of adsorption determined for air cleaved HOPG sample. As shown in Figures 4-30 and 4-31, the mercury adsorption capacity of HOPG increased after 20 min plasma oxidation, but no significant increase in the capacity was observed with further plasma oxidation. Therefore, it can be concluded that defect sites created by plasma oxidation only provided additional surface area for mercury adsorption.

On the other hand, the adsorption of an organic adsorbate (propane) was drastically different for air-cleaved and plasma-oxidized HOPG.[117] Plasma-created defects provided adsorption sites with stronger binding energy and faster adsorption kinetics for propane molecules as indicated by the appearance of the high temperature peak, the sequence of peak growth in a TPD spectra, and additional adsorption capacity.

The fact that there is no further increase in mercury adsorptive capacity with 90-p-HOPG sample over 20-p-HOPG sample also suggest that micro-pores are more important for mercury adsorption than meso- or macropores since after 20 min plasma oxidation of HOPG surface already produced defects with meso- and macro-sized ones and 90 min plasma oxidation just expanded existing defect site in size and depth.[125] It is well known that plasma oxidation initially attacks the pristine HOPG surface (basal plane) and that longer treatment leads to further expansion of initial defects.[102] As shown in Figure 3-8, 90 min plasma oxidation simply enlarged all smaller defects created on HOPG after 20 min treatment. However, even for a 20 min plasma oxidized sample, most of the defects are approximately 100 nm in diameter and fall in the mesopore region as classified by IUPAC, which explains limited increase in capacity for 20-p-HOPG over a-HOPG.

4.5.2 Fixed-bed Adsorption Studies with Activated Carbon

Breakthrough of elemental mercury from an adsorber charged with outgassed BPL carbon measured at different adsorption temperatures and influent mercury concentrations of 70 and 1120 $\mu g/m^3$ are shown in Figure 4-32. It can be seen that mercury uptake increases with a decrease in the reaction temperature, which follows the well-documented impact of temperature

on adsorption.[127] Breakthrough studies with influent mercury concentrations of 540 and 780 μg/m^3 were also performed in this study (data not shown here). Mercury uptake as a function of equilibrium vapor pressure at 100% breakthrough, that was estimated by integrating the breakthrough curves at different bed temperatures, is shown in Figure 4-33. It can be observed that the mercury adsorptive capacity increases linearly with an increase in influent mercury concentration for all adsorption temperatures, which suggests mercury adsorption on activated carbon occurs in Henry's law region[127] under the experimental conditions used in this study. Such behavior can be explained by the fact that the highest mercury concentration used in breakthrough experiments was less than 5 % of the vapor pressure at that temperature. In that case, mercury atoms are isolated from their neighbors and the equilibrium relationship between the gas phase and adsorbed phase concentration is linear.[127]

The relationship between the mercury equilibrium pressure and the reaction temperature at constant coverage can be approximated by the Clausius-Clapeyron equation[84] given in equation 4-3. Figure 4-34 depicts adsorption equilibrium data in the form of lnP versus 1/T for constant coverage of 200 μg/g at different adsorption temperatures investigated in this study. It is quite obvious that the experimental data point to two distinct regions with 348 K as the common point. Linear fit to data collected below 348 K is obtained with the heat of adsorption of 97 ± 5 kJ/mol while the data collected above 348 K revealed the heat of adsorption of 579 ± 25 kJ/mol. Compared to the heat of vaporization of mercury at 298 K of 64.3 kJ/mol,[96, 115] it is clear that mercury adsorption on activated carbon below 348 K is accomplished through physisorption, while the reaction temperatures above 348 K promote chemisorption.[127] These findings are supported by previous studies which suggested that mercury adsorption by activated carbon occurs through a combination of chemisorption and physisorption at ambient temperature[42] and

that chemisorption predominates at higher temperatures.[37, 130] The heat of adsorption of mercury on activated carbon at low temperatures (below 348 K) is in reasonable agreement with the value of 82 ± 3 kJ/mol estimated from the TPD studies with HOPG at UHV conditions. It can, therefore, be concluded that UHV studies with simple model carbonaceous surface can be used to investigate mercury adsorption on activated carbon in the physisorption region.

The data presented in Figures 4-27 and 4-29 demonstrated extremely limited impact of chemical functional groups on mercury uptake by HOPG. The impact of activated carbon surface chemistry on mercury uptake was studied using fixed-bed adsorption experiments with different samples of BPL activated carbon. Mercury breakthrough was measured for virgin (as received) BPL carbon and BPL carbon that was outgassed at 423 K (BPL-423) and 1173 K (BPL-1173). The heat treatment at 423 K was chosen because the water present on the carbon surface can be removed by this low temperature treatment without changing or damaging morphological structure of activated carbon[131] or removing the significant amount of oxygen containing functional groups that are normally stable up to 473 K.[10] The heat treatment at 1173 K was chosen to completely remove oxygen-containing functional groups from the carbon surface.[93]

Figure 4-35 compares mercury breakthrough at 293 and 423 K from fixed-bed adsorbers charged with different BPL samples using influent mercury concentration of 70 $\mu g/m^3$. The operating temperatures of 293 and 423 K were selected based on the findings shown in Figure 4-34 to facilitate physisorption and chemisorption mechanisms for mercury uptake, respectively. Breakthrough profiles on Figures 4-35 (a) and (b) suggest that the virgin BPL sample with original moisture content had the highest mercury adsorption capacity among the samples tested in this study. This observation agrees with the findings of Li et al.,[83] who also suggested that the surface water content of a carbon-based sorbent significantly enhances mercury uptake.

However, the water content was less significant for mercury uptake in chemisorption region because water is vaporized and removed from the carbon surface during the adsorption experiment at high bed temperatures. Figure 4-35 (a) also shows that mercury uptake capacity in a physisorption region increases by about 25 % as a result of the removal of surface functional groups by outgassing at 1123 K. Possible explanation for such behavior is that these functional groups restrict access of mercury molecules to micro pores that are very important for physisorption as demonstrated in studies with plasma-oxidized HOPG. On the other hand, removal of surface functionalities has an adverse impact on mercury uptake by chemisorption as shown in Figure 4-35 (b). Such behavior was expected because oxygen containing functional groups are important chemisorption sites for elemental mercury.[132]

The key findings of this study open the possibility to apply scientific information obtained from the studies with simple surfaces like HOPG under ideal conditions (UHV) to industrial sorbents process conditions. HOPG surface can be modified chemically and topologically by plasma oxidation to simulate key features of activated carbon adsorbents. A good agreement between the heats of adsorption determined from TPD studies under UHV conditions and breakthrough experiments at atmospheric pressure validates the proposed approach to bridge the traditional pressure gap in surface science.

5.0 SUMMARY AND CONCLUSIONS

This study investigated adsorption and desorption of model adsorbents representative of polar (acetone) and non-polar (propane) organic compounds and metallic (elemental mercury) compounds on a model carbonaceous surface (HOPG) under ultra high vacuum (UHV) conditions. Optical differential reflectance (ODR) technique was proven to be a powerful tool to investigate surface adsorption and desorption under the conditions where the temperature programmed desorption (TPD) technique can not be used, e.g., high pressure or reversible adsorption. The results showed a strong correlation between ODR determined in real time and a conventional surface science probe like TPD. This study also evaluated the effects of surface functional groups and topological heterogeneity on adsorption and desorption using and plasma oxidized HOPG as model carbonaceous surfaces. The key tasks that have been accomplished in this study include:

1. Demonstrate the utility of ODR technique for surface science studies on carbonaceous surfaces by comparison with conventional methods like TPD. This task was accomplished using acetone as a model adsorbate.
2. Establish the superiority of ODR technique over TPD to study reversible adsorption on HOPG using propane as a model adsorbate.
3. Determine the impact of oxygen containing functional groups on HOPG on adsorption and desorption of polar (acetone) organic compounds.
4. Establish the methodology to study the impact of chemical and topological heterogeneity (presence of pores) on adsorption/desorption on carbonaceous surfaces. This task was

accomplished using virgin and plasma-oxidized HOPG and propane as model adsorbent-adsorbate system.

5. Attempt to bridge the traditional pressure gap in surface science and extend the findings from UHV studies to industrial applications. This task was accomplished by studying mercury adsorption on model (HOPG) and real (activated carbon) carbonaceous surfaces under UHV and atmospheric pressure. The discussion that follows represents a summary of the accomplishments for each task of this study.

Task 1

Optical differential reflectance (ODR) and temperature programmed desorption (TPD) were combined to investigate adsorption and desorption of a volatile polar organic compound (acetone) on a semi-metal surface (highly oriented pyrolytic graphite, HOPG) under ultra high vacuum (UHV) conditions. The ODR change induced by adsorption/desorption was shown to correlate with relative coverage as determined by TPD experiments. TPD spectra revealed the existence of monolayer, bilayer and multilayer adsorption states with coverage dependent binding energies, reflecting inter-adsorbate interactions. Absolute acetone coverage was estimated from ODR experiments and adsorption was found to follow Volmer-Weber rather than layer-by-layer growth mode. ODR showed a great promise to monitor sub-monolayer coverage of organic compounds on carbonaceous surfaces.

Task 2

Propane adsorption and desorption on HOPG was studied to demonstrate the ability of the ODR technique in situations where the TPD technique cannot be used. Experiments were carried out for surface temperatures from 90 K to 110 K and pressures from ultra high vacuum up to 10^{-4} torr. The results showed that propane adsorbs in a layer-by-layer fashion. The reversibility of bilayer (and multilayer) formation can be clearly seen from the ODR signal increase and decrease caused by increases and decreases in propane pressure, while the monolayer of propane is formed regardless of propane pressure. The ODR method is able to dynamically follow the adsorption process as a function of time over a wide pressure range. The TPD measurements provide an estimate of the binding energy of propane monolayer on HOPG of 30 ± 2 kJ/mol. ODR measurements were used to estimate the heat of adsorption at incipient second layer formation of 23 ± 2 kJ/mol. The layer-by-layer formation feature can be observed by molecular simulations, showing a good agreement in the heat of adsorption for bilayer. This study clearly showed that ODR is suitable for investigating adsorption phenomena in real time and over a wide pressure range.

Task 3

Oxygen-containing functional groups that exist on both air-cleaved HOPG and plasma-oxidized HOPG can be removed by thermal treatment at over 500 K. Once these functional groups are removed, there is little re-adsorption occurring in UHV conditions. TPD results revealed a high temperature acetone desorption peak, which cannot be observed before significant amount of chemical functionalities are removed from HOPG surface. Thus, the

removal of oxygen containing functional groups on HOPG surfaces provides access for a polar organic adsorbate to a clean carbonaceous surface. These results suggest that carbonaceous surfaces should be thermally treated at temperatures above 1000 K to provide access to a non-functionalized surface. However, carbon sorbents may not need high temperature treatment for adsorption of polar organics, depending on the adsorption temperature. The energetics of acetone desorption from clean HOPG surface were estimated using both TPD simulation and variable heating rate experiments. The heat of adsorption of acetone using coverage dependant first order kinetics was estimated to be 55.5 ± 3.0 kJ/mol and 51.5 ± 3.0 kJ/mol for monolayer and bilayer, respectively. The thermal desorption spectra of acetone multilayer state are usually described by a zero order rate law. The activation energy for desorption of the acetone multilayer from graphite was determined using this procedure to be 31 ± 2 kJ/mol.

Task 4

The effects of chemical functional groups and surface morphology on the adsorption/desorption behavior of a model non-polar organic adsorbent (propane) on model carbonaceous surfaces: air-cleaved highly oriented pyrolytic graphite (HOPG) and plasma-oxidized HOPG, were investigated using temperature programmed desorption (TPD). The presence of oxygen functional groups almost completely suppresses propane adsorption at 90 K. However, these groups can be removed from both air-cleaved and plasma-oxidized HOPG by thermal treatment (> 500 K), leading to more than an order of magnitude increase in adsorption capacity. Oxygen related surface functional groups exist on HOPG surface. They apparently block available adsorption sites for non-polar organics. Heat treatment can remove existing functional groups to make these adsorption sites more accessible. It is essential for both air-

cleaved HOPG and plasma-oxidized HOPG to be outgassed at over 1273 K for all the adsorption sites to be chemically accessible for propane molecules.

Plasma oxidation, however, creates mechanical damage on initially flat surface that augments pre-existing defect sites which vary from ~10 to ~200 nm in diameter, and from ~1 to ~10 nm in depth. These defects serve as additional adsorption sites with stronger binding energy as indicated by the appearance of high temperature TPD features that do not exist on air-cleaved HOPG. The downward shift in peak temperature with increasing exposure suggests sequential filling of the defect sites, with the higher binding energy sites being filled first. In addition, the TPD areas for plasma-oxidized HOPG are always greater than those for the air-cleaved HOPG under identical exposure conditions. The effect of morphological heterogeneity is evident for plasma-oxidized HOPG as this substrate provides greater surface area available for adsorption as well as higher energy binding sites. It can be concluded that HOPG surface can be modified chemically and topologically by plasma oxidation to simulate key features of activated carbon adsorbents. The key findings of this study open the possibility to apply scientific information obtained from the studies with simple surfaces like HOPG under ideal conditions (UHV) to industrial sorbents and realistic process conditions.

Task 5

Temperature programmed desorption (TPD) with a model carbonaceous material (highly oriented pyrolitic graphite, HOPG) under ultra-high vacuum (UHV) conditions and fixed bed adsorption by activated carbon (BPL) at atmospheric conditions were combined to investigate the effects of chemical and morphological heterogeneities on mercury adsorption by

carbonaceous surfaces in an attempt to bridge the traditional pressure gap between UHV and atmospheric conditions in surface science. TPD results showed that mercury adsorption at 100 K onto HOPG surfaces, with and without chemical functional groups and topological heterogeneity created by plasma oxidation, occurs through physisorption. The removal of oxygen containing functional groups from HOPG surface slightly enhances mercury physisorption. Plasma oxidation of HOPG provides additional surface area for mercury adsorption. However, the pits created by plasma oxidation are more than 100 nm in diameter and do not simulate microporosity that predominates in activated carbons.

Mercury adsorption by activated carbon at atmospheric pressure occurs through two distinct mechanisms. Physisorption governs mercury adsorption at temperatures below 348 K while chemisorption predominates at adsorption temperatures above 348 K. The presence of water on activated carbon surface enhances mercury uptake by both physisorption and chemisorption. While oxygen-containing functional groups reduce mercury physisorption by blocking access to the micropores, no significant impact of oxygen functionalities was observed in the chemisorption region.

Overall, an optical technique (ODR) was proven to be a versatile tool to investigate surface adsorption and desorption under the conditions where TPD technique cannot be used due to high pressure or reversible adsorption. Surface chemical functional groups, which exist on HOPG surface, exert significant impact on the adsorption and desorption of polar and non-polar organics, but not so much for metallic species. Creating defects by plasma treatment of HOPG and adsorption/desorption studies under UHV conditions provides a great opportunity to understand the fundamental aspects of adsorption/desorption on high surface area carbonaceous materials (e.g., the impact of chemical and/or topological heterogeneity). A good agreement

between TPD studies under UHV conditions and breakthrough experiments at atmospheric pressure validates the proposed approach to bridge the traditional pressure gap in surface science.

5.1 Significance of the Study

This study demonstrated that in the presence of oxygen containing functional groups and topological heterogeneity (pores or defects) on carbonaceous surfaces, the adsorption capacity can vary significantly depending on the characteristics of the adsorbate. Experimental results showed that the removal of oxygen functional groups from HOPG surfaces leads to significant increase in adsorption capacity for propane. It can therefore be concluded that oxygen containing functional groups exhibit adverse impact on the uptake of non-polar organic adsorbates. One practical implication of this finding is that activated carbon manufacturers may find it beneficial to take necessary steps to prevent excessive oxidation of the carbon surface during the manufacturing process (e.g., reduce the oxygen content of the activation agent) if that adsorbent is to be used for the control or recovery of non-polar organic compounds.

On the other hand, removal of oxygen-containing functional groups from HOPG resulted in a slight increase in the adsorption capacity for mercury that can serve as a representative of metallic vapors. Furthermore, the removal of oxygen containing functional groups from HOPG resulted in higher energy binding sites on these carbonaceous surfaces for the adsorption of polar organic compounds (i.e., acetone), while the total adsorption capacity for these compounds remained unchanged regardless of the presence or absence of these groups. Therefore, it can be suggested that carbon sorbents that will be used for the uptake of metallic compounds, most notably, mercury, and polar organic compounds may not require special steps to prevent

excessive oxidation during manufacturing and should not be subjected to high temperature cleaning procedure (i.e., outgassing) as a pretreatment step. On the other hand, high temperature heat treatment may be one way to remove oxygen containing functional groups from the adsorbent surface to enhance its uptake efficiency for non-polar organic compounds.

This study also showed that the UHV studies with air-cleaved HOPG could be used to obtain fundamental insight into the adsorption processes occurring on high surface area carbonaceous materials (e.g., activated carbon) operated in physisorption region and under more realistic pressures (i.e., atmospheric). This extremely important finding is for the first time advanced by the results of this study and is supported by the fact that similar binding energies were obtained for mercury adsorption on HOPG operated under UHV conditions and commercially available activated carbon operated at lower adsorption temperatures (i.e., below 348 K). It is likely that the development of future adsorbent materials will take advantage of UHV studies because they allows precise determination and accurate understanding of adsorption processes on a molecular level. Such understanding will be crucial if we were to develop highly specialized adsorbents and take full advantage of new carbonaceous materials (e.g., nanotubes, nanofibers, etc.) that are currently quite expensive and should be used only for high value-added application (separation of valuable products like proteins, medications, noble metals, etc.)

Plasma oxidation is the experimental method that was deployed in this study in order to create adsorbents with high surface area to be able to study the impact of surface heterogeneity on adsorption process and offer a better approximation for industrial sorbents like activated carbon. However, the plasma treatment utilized in this study created mostly large pores (> 10 nm) that are representative of meso- and macropores in activated carbons. Therefore, the pores

created during a 20-min plasma treatment only provide additional surface area for the adsorption of propane and mercury. While these large pores resulted in only about 10 % increase in mercury uptake, propane adsorption was enhanced by over an order of magnitude and even the propane binding energy increased due to the introduction of this surface heterogeneity.

Therefore, it could be concluded that the relatively large pores (> mesopore) existing in carbon materials are not as significant in mercury adsorption as the smaller pores (micropore), which can be explained by capillary condensation that is facilitated in the pores whose size is on the same order of magnitude as the adsorbate molecule. Microporosity should be promoted during sorbent manufacturing (e.g., higher degree of burnout, more aggressive activating agent) in order to optimize particular sorbent for mercury removal.

This study also showed that mercury adsorption by activated carbon at atmospheric pressure and by HOPG at the UHV conditions occurs through two distinct mechanisms. Physisorption, which is typically considered reversible and results from low-level non-specific van der Waals forces, governs mercury adsorption at temperatures below 348 K. On the other hand, chemisorption, which is typically considered irreversible and results from high energy covalent bonds, predominates at adsorption temperatures above 348 K. Based on these findings, it can be concluded that any sorbent removing mercury from a contaminated air stream using a physisorption mechanism will not be a good long-term solution for mercury control because these weak bonds between mercury and adsorbent surface can be easily broken leading to mercury leaching into the environment. Such outcome is particularly undesirable in the case of mercury because there is no known mechanisms that leads to mercury degradation, while a well-known methylation process leads to the creation of highly toxic methyl mercury forms.

The presence of water on activated carbon and HOPG surface enhances mercury uptake by both physisorption and chemisorption. While oxygen-containing functional groups reduce mercury physisorption on activated carbon by blocking access to the micropores, no significant impact of oxygen functionalities was observed in the chemisorption region.

This study suggests that the high temperature (over 900 ^{o}C) treatment of carbon substrate provides only about 10 % increase of the mercury uptake capacity, thus treatment at high temperature of carbon substrate may not be a cost effective method for both low and high temperature flue gas conditions. The optimization of pore size distribution or finding favorable chemical functional groups should be much better approach to obtain a cost effective carbon adsorbent for mercury removal.

6.0 SUGGESTIONS FOR FUTURE WORK

Environmental engineering is faced with the lack of fundamental understanding of molecular interactions in the complex mixtures and at the mineral, organic, and biological interfaces that characterize environmental systems. This is particularly troubling because many of the techniques and associated methods for data interpretation have been developed to study well defined systems, e.g. single crystal under ideal conditions (ultra high vacuum). However, the application of these tools to environmental samples is very challenging due to their amorphous, complex, and multiple nature.

From the results of current study, it is clear that a linear optical differential reflection technique can be used to monitor adsorption of organic and metallic adsorbates. It can be suggested that improvement of the sensitivity of ODR is needed so that the differential ODR signal as a function of temperature in the desorption can be used in place of QMS for doing TPD at high pressure. It was also demonstrated that UHV studies using chemically and morphologically modified HOPG as a model carbon surface could be a possible approach to investigate the roles of chemical complexes and carbon morphological structure on mercury uptake. However, the role of chemical functional groups and morphological structure for efficient uptake of various other pollutants has not yet been determined. Therefore, the identification of the exact functional groups on carbonaceous surface and the investigation of the role of those functional groups should be followed.

Future studies may focus on extending adsorption study with model carbonaceous surface under UHV conditions using strategy that combines multiple techniques to fully characterize the many components of environmental samples. For instance, nano-scale carbon materials, such as

nanotubes or nano-carbon fibers, have attracted huge attention for controlling organic or inorganic gas and liquid phase pollutants by adsorption. In order to provide insight into environmental phenomena of these systems, experimental studies will be required. This work can be based on experimental analytical methodologies that I have used and developed through my research. However, in order to understand these phenomena more quantitatively, one should apply more advanced surface science approaches, such as scanning tunneling microscopy (STM), infrared reflection absorption spectroscopy (IRAS), etc.

It is well known that the performance of sulfur-impregnated activated carbons for mercury uptake is strongly related to physical and chemical properties of both the sulfur and carbon. However, in order to gain a better understanding of mercury uptake, it is important to incorporate information on the micro–structure and surface chemistry of the carbon. It is also important to expand molecular-level insight into adsorption, dissociation, and subsequent impregnation of sulfur containing compounds on carbonaceous surface. This work may offer the potential to understand the formation of HgS inside the carbon and the basic science underlying the adsorption of mercury on sulfur impregnated activated carbon.

The presence of a particular combination of gas constituents in the carrier gas, especially those that can affect the performance of carbonaceous adsorbents, (i.e., SO_2, NO and water) may also have some impacts on the carbon surface. Carbon may selectively adsorb certain gases, which could change the surface of that carbon. Furthermore, these gas molecules may compete for active sites with mercury. It may be very helpful to investigate this effect on selective adsorption on a microscopic level to explain findings from pilot scale column tests in terms of surface chemistry.

Novel carbon materials such as carbon nanotubes and activated carbon fiber have potential uses in selective adsorption of toxic species and selective catalysts or catalytic supports, since these carbon materials have distinct advantages over the activated carbon sorbents used industrially due to their abilities of modification on the molecular level to adsorb or transport specific classes of molecules. One may be able to extend the experimental approach used in this study to a study of the essential physics of the interactions on these nanoporous carbonaceous surfaces.

APPENDIX

APPENDIX

A1. Propane Heat of Vaporization (at 1(lation

- Calculation of heat of vaporization of propane at 100 K

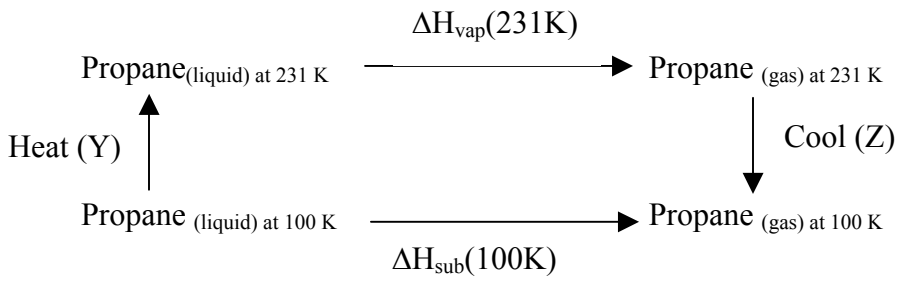

- $\Delta H_{vap}(231K)$ = Propane heat of vaporization at 231 K = 19.04 kJ/mol [96]
- Energy needed to heat liquid propane from 100 K to 231 K

$$Y = \int_{100}^{231} C_p[propane(l)]dT = \int_{100}^{231} [59.642 + 0.32831T - 0.0015377T^2 + (3.6539 \times 10^{-6})T^3]dT$$

= 11.6 kJ/mol

$C_p[Propane(l)]$ = Heat capacity of liquid propane [115]

- Energy needed to cool vapor propane from 231 K to 100 K

$$Z = \int_{231}^{100} C_p[propane(g)]\,dT$$

$$= \int_{231}^{100} [28.277 + 0.116T + 0.00019597T^2 - (2.3271 \times 10^{-7})T^3 + (6.8669 \times 10^{-11})T^4]dT$$

= - 6.81 kJ/mol

$C_p[propane(g)]$ = Heat capacity of vapor propane [115]

The heat of vaporization of propane at 100 K = $\Delta H_{vap}(231K)$ + Y + Z
= 19.04 + 11.64 -6.81
= 23.87 kJ/mol

A2. Acetone Heat of Sublimation (at 130 K) Calculation

- Calculation of heat of sublimation of acetone at 130 K

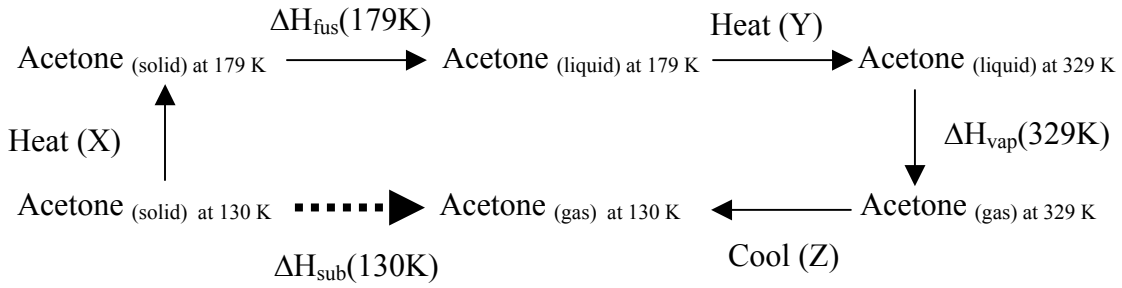

- $\Delta H_{fus}(179K)$ = Acetone heat of fusion at 179 K = 5.69 kJ/mol[109]
- $\Delta H_{vap}(329K)$ = Acetone heat of vaporization at 329 K = 29.1 kJ/mol[109]
- Energy needed to heat solid acetone from 130 K to 179 K

$$X = \int_{130}^{179} C_p[acetone\ (s)]\ dT = \int_{100}^{231} [-3.893 + 0.93523\ T - 0.0021879\ T^2]dT$$

= 4.31 kJ/mol

$C_p[acetone(s)]$ = Heat capacity of solid acetone[115]

- Energy needed to heat liquid acetone from 179 K to 329 K

$$Y = \int_{179}^{329} C_p[acetone(l)]\ dT$$
$$= \int_{179}^{329} [46.878 + 0.62652T - 0.0020761T^2 + (2.9583\times10^{-6})T^3]dT$$

= 18.13 kJ/mol $C_p[acetone(l)]$ = Heat capacity of liquid acetone[115]

- Energy needed to cool vapor acetone from 329 K to 130 K

$$Z = \int_{329}^{130} C_p[acetone(g)]\ dT$$
$$= \int_{329}^{130} [35.918 + 0.093896T + 0.0001873T^2 - (2.1643\times10^{-7})T^3 + (6.3174\times10^{-11})T^4]dT$$

= - 12.95 kJ/mol $Cp[acetone(g)]$ = Heat capacity of vapor acetone[115]

- $\Delta H_{sub(130K)}$
  = Acetone heat of sublimation at 130 K = $\Delta H_{fus}(179K) + X + \Delta H_{vap}(329K) + Y + Z$
  = 5.69 + 4.31 + 18.13 + 29.1 -12.95 = 44.28 kJ/mol

A3. Mercury Heat of Sublimation (at 200 K) Calculation

- Schematic view for the calculation of heat of sublimation of mercury at 200 K

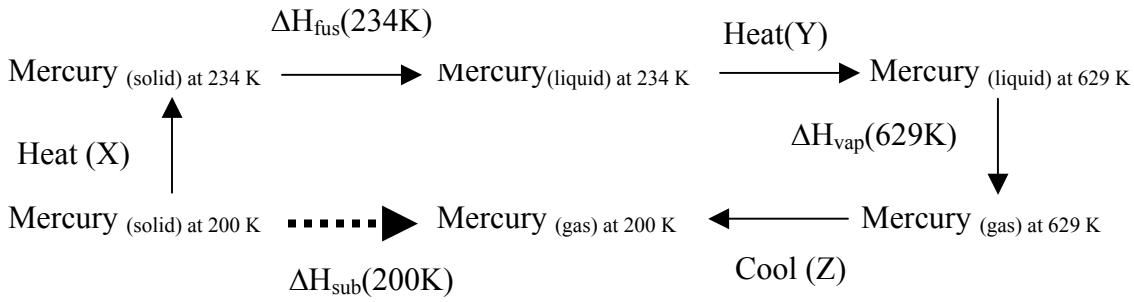

- $\Delta H_{fus}(234K)$ = Mercury heat of fusion at 234 K: 2.3 kJ/mol [96]
- $\Delta H_{vap}(629K)$ = Mercury heat of vaporization at 629 K = 59.11 kJ/mol[96]

$$X = \int_{200}^{234} C_p[mercury\ (s)]\,dT = \int_{200}^{234} [21.905 + 0.023673 + 0.00001707\ T^2]dT$$

- Energy needed to heat solid mercury from 200 K to 234 K
= 0.95 kJ/mol

$C_p[mercury(s)]$ = Heat capacity of solid Hg [115]

- Energy needed to heat liquid mercury from 234 K to 629 K

$$Y = 59.11 + \int_{234}^{629} C_p[mercury(l)]\,dT$$

$$= 59.11 + \int_{234}^{629} [30.388 - 0.01098T + (9.4412\times10^{-6})T^2 + (6.7418\times10^{-10})T^3]dT$$

= 10.9

$C_p[mercury(l)]$ = Heat capacity of liquid Hg [115]

- Energy needed to cool vapor mercury from 629 K to 200 K

$$Z = \int_{629}^{200} C_p[mercury(g)]\,dT$$

$$= \int_{629}^{200} [20.79 - 0.000018318T + (2.3525\times10^{-8})T^2 - (1.0144\times10^{-11})T^3 + (1.3685\times10^{-15})T^4]dT$$

= - 8.92 kJ/mol

$C_p[mercury(g)]$ = Heat capacity of vapor Hg [115]

- The heat of sublimation of mercury at 200 K
= X + $\Delta H_{fus}(234K)$ + $\Delta H_{vap}(629K)$ + Y + Z = 0.95 + 2.3 + 59.11 + 10.9 - 8.92
= 64.34 kJ/mol

A4. Properties of Adsorbates

	Mercury (Hg)		Acetone (C_3H_6O)		Propane (C_3H_8)	
Molecular weight (g/mol)	200.59[96]		58[96]		44.1[96]	
Boiling point (T_b,K)	629.73[96]		329[96]		230.9[96]	
Melting point (T_m,K)	234.17[96]		229[96]		83.3[96]	
Refractive index	1.91+ *i* 5.15 at 619.9 nm[133]		1.36 at 589 nm[96]		1.4745 at 589 nm[96]	
Triple point (K)	234.17[96]		229[96]		83.3[96]	
Critical point (K)	1750[96]		508[96]		369.83[96]	
Density (g/cm^3)	13.53 at 20 ^oC[96]		0.7899 at 20 ^oC[96]		0.493 at 25 ^oC[96]	
Heat capacity (J/mol-K)	**Sol**	28.196 @228K[115]	**Sol**	93.32 @178 K[115]	**Sol**	52.32[126] @84 K
	Liq	27.87 @298K[96]	**Liq**	127.53 @298K[115]	**Liq**	117.67 @298K[115]
	Gas	20.79 @298K[96]	**Gas**	80.32 @329K[115]	**Gas**	62.86 @230.9K[115]
Heat of vaporization (kJ/mol)	59.11 @T_b[96]		28.31 @T_b[96]		19.04 @T_b[96]	
Heat of fusion (kJ/mol)	2.3 @T_m[96]		5.69 @ T_m[96]		3.53 @T_m[96]	

BIBLIOGRAPHY

BIBLIOGRAPHY

1. McFarland, R.B. and Reigel, H., "Chronic Mercury Poisoning from A Single Brief Exposure". Journal Occupational Medicine, 1978. 20: p. 532-534.

2. Susuki, T., ed.,, "Advances in Mercury Toxicology, "Epidemiological and Clinical Features of Minamata Disease, by A. Igata". 1991, NewYork: Plenum Press. 439-457.

3. Lehotzky, K. and Bordas, S., "Study on the Subacute Neurotoxic Effect of Methoxy-Ethyl Mercury Chloride (MEMC) in Rats". Medicina del Lavoro, 1968. 59: p. 241-249.

4. Billings, C.E., Sacco, A.M., Matson, W.R., Griffin, R.M., Coniglio, W.R., and Harley, R.A., "Mercury Balance on A Large Pulverized Coal-Fired Furnace". Journal of the Air Pollution Control Association, 1973. 23(9): p. 773-777.

5. Johnson, J., "Controversial EPA Mercury Study Endorsed by Science Panel". Environmental Science and Technology, 1997. 31(5): p. 218A-219A.

6. Rodriguez-Reinoso, F., "The Role of Carbon Materials in Heterogeneous Catalysis". Carbon, 1998. 36(3): p. 159-175.

7. Tsutsumi, K., Matsushima, Y., and Matsumoto, A., "Surface Heterogeneity of Modified Active Carbons". Langmuir, 1993. 9: p. 2665-2669.

8. Marchon, B., Carrazza, J., Heinemann, H., and Somorjai, G.A., "TPD and XPS Studies of O_2, CO_2 and H_2O Adsorption on Clean Polycrystalline Graphite". Carbon, 1988. 26(4): p. 507-514.

9. Bandosz, T.J., Jagiello, J., and Schwarz, J.A., "Effect of Surface Chemical Groups on Energetics Heterogeneity of Activated Carbons". Langmuir, 1993. 9: p. 2518-2522.

10. Otake, Y. and Jenkins, R.G., "Characterization of Oxygen-Containing Surface Complexes on a Microporous Carbon by Air and Nitric Acid Treatment". Carbon, 1993. 31(1): p. 109-121.

11. Tamon, H. and Okazaki, M., "Influence of Acidic Surface Oxides of Activated Carbon on Gas Adsorption Characteristics". Carbon, 1996. 34(6): p. 741-746.

12. Lisovskii, A., Semiat, R., and Aharoni, C., "Adsorption of Sulfur Dioxide by Active Carbon Treated by Nitric Acid: I. Effect of the Treatment on Adsorption of SO_2 and Extractability of the Acid Formed". Carbon, 1997. 35(10-11): p. 1639-1643.

13. Prado-Burguete, C., Linares-Solano, A., Rodriguez-Reinoso, F., and Salinas-Martinez de Lecea, C., "The Effect of Oxygen Surface Groups of the Support on Platinum Dispersion in Pt/Carbon Catalysis". Journal of Catalysis., 1989. 115: p. 98-106.

14. Bautista-Toledo, I., Rivera-Utrilla, J., Ferro-Garcia, M.A., and Moreno-Castilla, C., "Influence of the Oxygen Surface Complexes of Activated Carbons on the Adsorption of Chromium Ions from Aqueous Solutions: Effect of Sodium Chloride and Humic Acid". Carbon, 1994. 32(1): p. 93-100.

15. Moreno-Castilla, C., Ferro-Garcia, M.A., Rivera-Utrilla, J., and Joly, J.P., "A TPD Study of Chromium Catalysts Supported on an Oxidized and Nonoxidized Activated Carbon". Energy & Fuels, 1994. 8: p. 1233-1237.

16. Otani, Y., Emi, H., Kanaoka, C., Uchjima, I., and Nishino, H., "Removal of Mercury from Air with Sulfur-Impregnated Adsorbents". Environmental Science and Technology, 1988. 22: p. 708-711.

17. Youssef, A.M., Mostafa, M.R., and Dorgham, E.M., "Coal-Based Activated Carbons for the Removal of Sulphur Dioxide via Adsorption". Adsorption Science and Technology, 1997. 15: p. 803-814.

18. Moreno-Castilla, C., Carrasco-Marin, F., Utrera-Hodalgeo, E., and Rivera-Utrilla, J., "Activated Carbons as Adsorbents of SO_2 in Flowing Air. Effect of Their Pore Texture and Surface Basicity". Langmuir, 1993. 9: p. 1378-1383.

19. Davini, P., "Adsorption and Desorption of SO_2 on Activated Carbon: The Effect of Surface Basic Groups". Carbon, 1990. 28(4): p. 565-571.

20. Daley, M.A., Mangun, C.L., DeBarr, S., Lizzio, A.A., Donnals, G.L., and Economy, J., "Adsorption of SO_2 on Heat-Treated Activated Carbon Fibers". Carbon, 1997. 35: p. 411-417.

21. Lindqvist. O., Johnsson. A., Astrup. M., Anndersson. A., Bringmark. L., Hovseniun. G., Iverfilt. A., and Timm. B., "Mercury in Swedish Environment - Recent Research on Causes, Consequences and Corrective Method". Water, Air and Soil Polution, 1991. 55: p. 260-270.

22. Lindberg, S.E., "Mercury Partitioning in a Power Plant Plume and Its Influence on Atmospheric Removal Mechanisms". Atmospheric Environment, 1980. 14: p. 227-231.

23. Klein, D.H., Andren, A.W., Carter, J.A., Bolton, N., and Vanhook, R.I., "Pathways of Thirty-seven Trace Elements Through Coal-Fired Power Plant". Environmental Science and Technology, 1975. 9(10): p. 973-979.

24. Porcella, D.B. and Jermelov, A., "Global Mercury Pollution and the Role of Gold Mining: An Overview". Water, Soil and pollution, 1997. 97: p. 205-207.

25. Chu, P. and Porcella, D.B., "Mercury Stack Emissions From U.S. Electric Utility Power Plan". Water, Air and Soil Pollution, 1995. 80: p. 135-144.

26. Midwest Research Institute, "Locating and Estimating from Sources of Mercury and Mercury Compounds". EPA -454/R-93-023, September 1993.

27. Proceedings of the 91st Annual Meeting & Exhibition of the Air and Waste Management Association, S.D., CA, June 14-18, 1998, "A Comparison of Air Toxic Metal Control Technology, by J.H. Pavlish and M. D. Mann," 98-RA79B.01.

28. Pai, P., Heisler, S., and Joshi, A., "An Emission for Regional Atmospheric Modeling of Mercury". Water, Air and Soil Pollution, 1998. 101: p. 289-308.

29. "EPA Strengthens Air Emissions Standards for Municipal Waste Incinerators". Journal of the Air and Waste Management Association, 1991. 41: p. 259-260.

30. Proceedings of the 1994 Pittsburgh Coal Conference, V., Pittsburgh, PA, Sept. 12-16, 1994, "A New Survey of Mercury in U.S. Coals, by N. S. Bloom and E.M. Prestbo" (Pittsburgh: Pittsburgh Coal Conference, 1994), pp. 563-568.

31. Germani, M.S. and Zoller, W.H., "Vapor-Phase Concentrations of Arsenic, Selenium, Bromine, Iodine, and Mercury in the Stack of a Coal-Fired Power Plant". Environmental Science and Technology, 1988. 22: p. 1079-1085.

32. Douglas, J., "Mercury in the Environment". EPRI Journal, 1991. 16: p. 4-11.

33. EPA, "Characterization of Products Containing Mercury in Municipal Solid Waste in the United States, 1970 to 2000, PB92-162596." 1992.

34. Fukuzaki, N. and Ichikawa, Y., "Determination of Particulate Mercury in Air". Bunseki Kagaku, 1984. 33: p. 178-182.

35. Kitamura, M., ed.,, "Mercury". 1976, Tokyo: Kodansha.

36. Nriagu, J.O., ed. The Biogeochemistry of Mercury in the Environment, "Economic Considerations in Controlling Mercury Pollution, by W.D. Watson, Jr.", (New York: Elsevier/North-Holland Inc., 1979), Chapter 3.

37. Krishnan, S.V., Gullett, B.K., Jozewicz, W., "Sorption of Elemental Mercury by Activated Carbons". Environmental Science and Technology, 1994. 28: p. 1506-1512.

38. Chang, R. and Owens, D., "Developing Mercury Removal Methods for Power Plants". EPRI Journal, 1994: p. 46-49.

39. Ghorishi, B. and Gullet, B.K., "Sorption on Elemental Mercury and Mercuric Chloride by Activated Carbon and Calcium Based Sorbents. (Dunham, NC. : Acurex Environmental Corporation, 1997), unpublished." 1997.

40. Liu, W., Vidic, R.D., and Brown, T.D., "Optimization of Sulfur Impregnation Protocol for Fixed-Bed Application of Activated Carbon-Based Sorbents for Gas-Phase Mercury Removal". Environmental Science and Technology, 1998. 32: p. 531-538.

41. Proceedings of the 87th Annual Meeting and Exhibition of the Air and Waste Management Association, C., OH, June 19-24, 1994, "Experimental Evaluation of Sorbents for the Capture of Mercury in Flue Gases, by C.D. Livengood, H.S. Huang, and J.M. Wu" 14 p.

42. Chang, R. and Offen, G., "Mercury Emission Control Technologies: An EPRI Synopsis". Power Engineering, 1995. 99(11): p. 51-57.

43. Otani, Y., Kanaoka, C., Usui, C., Matsui, S., and Emi, H., "Adsorption of Mercury Vapor on Particles". Environmental Science and Technology, 1986. 20: p. 735-738.

44. Sinha, R.K. and Walker, P.L., "Removal of Mercury by Sulfurized Carbons". Carbon, 1972. 10: p. 754-756.

45. Proceedings of the of the 90th Annual Meeting & Exhibition on the Air and Waste Management Association, T., Ontario, Canada, July 8-13, 1993, "Mercury Vapor Removalfrom Simulated Flue Gas with Illinois Coal-Derived Activated Carbon, by Hsi, H., Massoud, R. A., Rood, M. J., Chen, S.," 97-RA79B.03.

46. Kwon, S. and Vidic, R.D., "Evaluation of Two Sulfur Impregnation Methods on Activated Carbon and Bentonite for the Production of Elemental Mercury Sorbent". Environmental Engineering Science, 2000. 17(6): p. 303-313.

47. Karatza, D., Lancia, A., Musmarra, D., Pepe, F., and Volpicelli, G., "Removal of Mercuric Chloride from Flue Gas by Sulfur Impregnated Activated Carbon". Hazardous Waste & Hazardous Materials, 1996. 13(1): p. 95-105.

48. Toles, C.A., Marshall, W.E., and Johns, M.M., "Surface functional groups on acid-activated nutshell carbons". Carbon, 1999. 37(8): p. 1207-1214.

49. Mangun, C.L., DeBarr, J.A., and Economy, J., "Adsorption of sulfur dioxide on ammonia-treated activated carbon fibers". Carbon, 2001. 39(11): p. 1689-1696.

50. Swiatkowski, A. and Goworek, J., "Studies on the adsorption equilibrium in the system benzene-methanol/deoxidized active carbon". Carbon, 1987. 25(3): p. 333-6.

51. Kuznetsova, A., Yates, J., J. T.,, Liu, J., and Smalley, R.E., "Physical Adsorption of Xenon in Open Single Walled Carbon Nanotubes: Observation of a Quasi-One-Dimensional Confined Xe Phase". Journal of Chemical Physics, 2000. 112(21): p. 9590-9598.

52. Mawhinney, D.B., Naumenko, V., Kuznetsova, A., Yates Jr., J.T., and Smalley, R.E., "Surface defect site density on Single Walled Carbon Nanotubes by Titration". Chemical Physics Letters, 2000. 324: p. 213-216.

53. Kuznetsova, A., Mawhinney, D.B., Naumenko, V., Yates. Jr., J.T., Lui, J., and Smalley, R.E., "Enhancement of Adsorption inside of Single-walled Nanotubes : Opening the Entry Ports". Chemical Physics Letters, 2000. 321: p. 292-296.

54. Jia, Y.F. and Thomas, K.M., "Adsorption of cadmium ions on oxygen surface sites in activated carbon". Langmuir, 2000. 16(3): p. 1114-1122.

55. Chiang, H.-L., Huang, C.P., Chiang, P.C., and You, J.H., "Effect of metal additives on the physico-chemical characteristics of activated carbon exemplified by benzene and acetic acid adsorption". Carbon, 1999. 37(12): p. 1919-1928.

56. Hsi, H.-C., Rood, M.J., Rostam-Abadi, M., Chen, S., and Chang, R., "Effects of Sulfur Impregnation Temperature on the Properties and Mercury Adsorption Capacities of Activated Carbon Fibers (ACFs)". Environmental Science and Technology, 2001. 35(13): p. 2785-2791.

57. Lizzio, A.A. and DeBarr, J.A., "Effect of Surface Area and Chemisorbed Oxygen on the SO_2 Adsorption Capacity of Activated Char". Fuel, 1996. 75(13): p. 1515-1522.

58. Davini, P., "Adsorption of Sulfur Dioxide on Thermally Treated Active Carbon". Fuel, 1989. 68(2): p. 145-148.

59. Lizzio, A.A. and DeBarr, J.A., "Mechanism of SO_2 Removal by Carbon". Energy & Fuels, 1997. 11: p. 284-291.

60. Lisovskii, A., Shter, G.E., Semiat, R., and Aharoni, C., "Adsorption of Sulfur Dioxide by Active Carbon Treated by Nitric Acid: II. Effect of Preheating on the Adsorption Properties". Carbon, 1997. 35(10-11): p. 1645-1648.

61. Dvorak, J. and Dai, H.L., "Optical Reflectivity Change Induced by Adsorption on Metal Surface : The Origin and Applications to Monitoring Adsorption Kinetics". Journal of Chemical Physics, 2000. 112(2): p. 923-934.

62. Halevi, P.E., "Photonic Probes of Surface". Surface Differential Reflectance-Experiment. Vol. 2. 1995, NY: Elsevier. 97-174.

63. Wong, A. and Zhu, X.D., "An Optical Differential Reflectance Study of Adsorption and Desorption of Xenon and Deuterium on Ni(111)". Applied Physics A, 1996. 63: p. 1-8.

64. Jin, X.F., Mao, M.Y., Ko, S., and Shen, Y.R., "Adsorption and Desorption Kinetics of CO on Cu(110) Studied by Optical Differential Reflectance". Physical Review B, 1996. 54: p. 7701-7704.

65. Volkmann, U.G., Mannebach, H., and Knorr, K., "Ellipsometery Study of Multilayer Growth and Wetting of $C_2Cl_2F_4$ Physisorbed on Graphite". Langmuir, 1998. 14: p. 4904-4907.

66. Chabal, Y.J., "Surface Infrared Spectroscopy". Surface Science Reports, 1988. 8((5-7)): p. 211-357.

67. Kuhl, D.E., Lin, K.C., Chung, C., Luo, J.S., Wang, H., and Tobin, R.G., "Coverage-, Temperature-, and Frequency-Dependent Broadband Infrared Reflectance Change Induced by CO Adsorption on Pt(111)". Chemical Physics, 1996. 205(1): p. 1-10.

68. Dvorak, J., Borguet, E., and Dai, H.L., "Monitoring Adsorption and Desorption on a Metal Surface by Optical Non-Resonant Reflectivity Changes". Surface Science, 1996. 369: p. L122-L130.

69. McIntyre, J.D.E. and Aspnes, D.E., "Differential Reflection Spectroscopy of Very Thin Films". Surface Science, 1971. 24: p. 417-434.

70. Reutt, J.E., Chabal, Y.J., and Christman, S.B., "Coupling of H vibration to Substrate Electronic States in Mo(100)-p(1 x 1)H and W(100)-p(1 x 1)H: Example of Strong Breakdown of Adiabaticity". Physical Review B, 1988. 38: p. 3112-3132.

71. Dumas, P., Suhren, M., Chabal, Y.J., Hirschmugl, C.J., and Williams, G.P., "Adsorption and Reactivity of NO on Cu(111): A Synchrotron Infrared Reflection Absorption Spectroscopic Study". Surface Science, 1997. 371(2-3): p. 200-212.

72. Xiao, X., Xie, Y., and Shen, Y.R., "Surface Diffusion Probe by Linear Optical Diffraction". Surface Science., 1992. 271: p. 295-298.

73. Zhu, X.D., Rasing, T., and Shen, R.Y., "Surface Diffution of CO on Ni(111) Studied by Diffraction of Optical Second-Harmonic Generation off a Monolayer Grating". Physical Review Letters, 1988. 61(25): p. 2883-2885.

74. Schlichting, H. and Menzel, D., "Techniques for Wide Range, High Resolution and Precision, Thermal Desorption Measurements". Surface Science, 1993. 285: p. 209-218.

75. de Jong, A.M. and Niemantsverdriet, J.W., "Thermal Desorption Analysis: Comprehensive Test of Ten Commonly Applied Procedures". Surface Science, 1990. 233: p. 355-365.

76. Paserba, K.R. and Gellman, A.J., "Effects of conformational isomerism on the desorption kinetics of n-alkanes from graphite". Journal of Chemical Physics, 2001. 115(14): p. 6737-6751.

77. King, D.A., "Thermal Desorption from Metal Surface: A Review". Surface Science, 1975. 47: p. 384-402.

78. Paserba, K., Shukla, N., Gellman, A.J., Gui, J., and Marchon, B., "Bonding of Ethers and Alcohols the a-CHx Films". Langmuir, 1999. 15: p. 1709-1715.

79. King, D.A., Madey, T.E., and Yates Jr., J.T., "Interaction of Oxygen with Polycrystalline Tungsten. II . Corrosive Oxidation". Journal of Chemical Physics, 1971. 55(7): p. 3247-3253.

80. King, D.A., Madey, T.E., and Yates Jr., J.T., "Interaction of Oxygen with Polycrystalline Tungsten. I . Sticking Probabilities and Desorption Spectra". Journal of Chemical Physics, 1971. 55(7): p. 3236-3246.

81. Chakarov, D.V., Osterlund, L., and Kasemo, B., "Water Adsorption and Coadsorption with Potassium on Graphite(0001)". Langmuir, 1995. 11: p. 1201-1214.

82. Aubuchon, C.M., Davison, B.S., Nishimura, M., and Tro, N.J., "Desorption Kinetics and Adlayer Structure of n-Pentane on Al_2O_3(0001)". Journal of Physical Chemistry, 1994. 98: p. 240-244.

83. Li, Y.H., Lee, C.W., and Gullett, B.K., "The effect of activated carbon surface moisture on low temperature mercury adsorption". Carbon, 2002. 40: p. 65-72.

84. Akins, P., "Physical Chemistry, 6th ed." 1998, YewYork: W. H. Freeman and Company.

85. Morris, M.A., Bowker, M., and King, D.A., "Comprehensive Chemical Kinetics.,edited by C. H. Bamford, C. F. H. Tipper and R. G. Compton". Vol. 19. 1984, Amsterdam: Elsevier.

86. Habenschaden, E. and Kuppers, J., "Evaluation of Flash Desorption Spectra". Surface Science, 1984. 138: p. L147-L150.

87. Chan, C.M., Aris, R., and Weinberg, W.H., "An Analysis of Thermal Desorption Spectra. I." Applied Surface Science, 1978. 1: p. 360-376.

88. Konvalinka, J.A. and Scholten, J.J.F., "The "Shape Index" of Temperature-Programmed Desorption Curves". Journal of Catalysis, 1978. 52: p. 547-549.

89. Redhead, P.A., "Thermal desorption of Gas". Vacuum, 1962. 12: p. 203-211.

90. Kreuzer, H.J. and Payne, S.H., "Advanced in Gas-Phase Photochemistry and Kinetics : Dynamics of Gas-Surface Interface-Chapter 6: Thermal Desorption Kinetics", ed. M.N. Ashfold. 1991, Cambridge: The Royal Chemical Society. 221-526.

91. Hall, R.C. and Holmes, R.J., "The Preparation and Properties of Some Activated Carbons Modified by Treatment with Phosgene or Chlorine". Carbon, 1992. 30(2): p. 173-176.

92. Hall, R.C. and Holmes, R.J., "The Preparation and Properties of Some Chlorinated Activated Carbons, Part II. Further Observations". Carbon, 1993. 31(6): p. 881-886.

93. Tessmer, C.H., Vidic, R.D., and Uranowski, L.J., "Impact of Oxygen-Containing Surface Functional Groups on Activated Carbon Adsorption of Phenols". Environmental Science and Technology., 1997. 31: p. 1872-1878.

94. Blum, B., Salvarezza, R., and Arvia, A.J., "Vapor-deposited Gold Film Formation on Highly Oriented Pyrolitic Graphite. A Transition from Pseudo-Two-Dimensional Branched Island Growth to Continuous Film Formation". Journal of Vacuum Science and Technology B, 1999. 17(6): p. 2431-2438.

95. Palmer, R.E. and Kenny, D.J., "Nucleation and Growth of C_{60} Thin Films on Graphite". Surface Science, 2000. 447: p. 126-132.

96. Lide, D.R., "CRC Handbook of Chemistry and Physics, 78 th ed". 1997, Boca Raton: CRC press.

97. Kim, S., Wang, Z., and Scherson, D.A., "Theoretical Aspects of Differential Reflectance and Electroreflectance Spectroscopy in the UV-Vis Region Applied to the Study of Molecular Layers Adsorbed on Metal Surface". Journal of Physical Chemistry B, 1997. 101: p. 2735-2740.

98. Cole, R.J., Frederik, B.G., and Weightman, P., "Substrate Dependence of Adlayer Optical Response in Reflectance Anisotropy Spectroscopy". Journal of Vacuum Science & Technology A, 1998. 16(5): p. 3088-3095.

99. Selci, S., Ciccacci, F., Chiarotti, G., Chiaradia, P., and Cricenti, A., "Surface Differential Reflectivity Spectroscopy of Semiconductor Surface". Journal of Vacuum Science Technology A, 1987. 5(3): p. 327-332.

100. Binning, G., Quate, C., and Gerber, C., "Atomic Force Microscope". Physical Review Letters, 1986. 56: p. 930-933.

101. Colton, R., Engle, A., Frommer, J., Gaub, H., Gewirth, A., Guchenberger, R., Rabe, J., Heckel, W., and Parkinson, B., "Procedures in Scanning Probe Microscopies". 1998, Chichester, NY: John Wiley & Sons.

102. Paredes, J.I., Martinez-Alonso, A., and Tascon, J.M.D., "Comparative Study of the Air and Oxygen Plasma Oxidation of Highly Oriented Pyrolytic Graphite: A Scanning Tunneling and Atomic Force Microscopy Investigation". Carbon, 2000. 38: p. 1183-1197.

103. Test Methods for Evaluating Solid Wastes, P.C.M., U.S. EPA SW-846, Method 7470 (Mercury in Liquid Waste), 1986, pp. 1-8., 1986.

104. Shendrikar, A.D., Damie, A., and Gutknecht, W.F., "Collection Efficiency Evaluation of Mercury-Trapping Media for the SASS Train Impinger System, EPA-600/7-84-089 (Research Triangle Park, NC: NTIS, August, 1984)." 1984.

105. Dinger, A., Lutterloh, C., Biener, J., and Kuppers, J., "Reactions of Hydrogen Atoms with Acetone Monolayers Adsorbed on Graphite Monolayer Covered Pt(111) surfaces". Surface Science., 1999. 437: p. 116-124.

106. Pisani, C., Rabino, G., and Ricca, F., "Statical Analysis and Model Determination for Thermal Desorption Spectra: Nitrogen on Tungsten". Surface Science, 1974. 41: p. 277-292.

107. Zangwill, A., "Physics at Surfaces". 1988, New York: Cambridge University Press. 428-432.

108. Witman, K., Borgmann, D., and Wedler, G., "Combination of Temperature-Programmed Thermal Desorption and Laser-Induced Thermal Desorption". Applied Physics A, 1990. 51: p. 132-136.

109. Dean, J.A., "Lange's Handbook of Chemistry, 5th ed." 1999, New York: McGraw-Hill Inc.

110. Johnson, L.G. and Dresselhaus, G., "Optical Properties of Graphite". Physical Review B, 1973. 7(6): p. 2275-2285.

111. Kwon, S., Russell, J., Zhao, X., Vidic, R., Johnson, J.K., and Borguet, E., "A Combined Experimental and Theoretical Investigation of Polar Organic Adsorption/Desorption from Model Carbonaceous Surfaces; Acetone on Graphite". Langmuir, 2002. 18(7): p. 2595-2600.

112. Zhao, X., Johnson, J.K., Kwon, S., Radisav, R.D., and Borguet, E., "Layering and Orientational ordering of Propane on Graphite: An Experimental and Simulation Study". In Preparation, 2002.

113. Wetterer, S.M., Lavrich, D.J., Cummings, T., Bernasek, S.L., and Scoles, G., "Energetics and Kinetics of the Physisorption of Hydrocarbons on Au (111)". J. Phys. Chem. B, 1998. 102: p. 9266-9275.

114. Woodruff, D.P. and Delchar, T.A., "Modern Techniques of Surface Science". 1986, Cambridge: Cambridge University Press.

115. Yaws, C.L., ed. Chemical Properties Handbook. 1999, McGraw-Hill: New York.

116. Ma, M.C., Brown T. C., and Haynes, B.S., "Evaluation of Thermal Desorption Spectra for Heterogeneous Surface : Application to Carbon Surface Oxides". Surface Science, 1993. 297: p. 312-326.

117. Kwon, S., Vidic, R., and Borguet, E., "Enhancement of Adsorption on HOPG by Modification of Surface Chemical Functionality and Morphology". Carbon, 2002. In Press.

118. Boehm. HP., "Some Aspects of the Surface Chemistry of Carbon Blacks and Other Carbons". Carbon, 1994. 32: p. 759-769.

119. D. R. Lide and H. V. Kehiaian, "CRC Hnadbook of Thermophysical and Thermochemical Data". 1997, Boca Raton: CRC Press.

120. Shukla, N., Gui, J., and Gellman, A.J., "Adsorption of Fluorinated Ethers and Alcohols on Graphite". Langmuir, 2001. 17: p. 2395-2401.

121. Lei, R.Z. and Gellman, A.J., "Humidity Effects on PFPE Lubricant Bonding to a-CHx Overcoats". Langmuir, 2000. 16: p. 6628-6635.

122. Chang, H. and Bard, A.J., "Formation of Monolayer Pits of Controlled Nanometer Size on Highly Oriented Pyrolytic Graphite by Gasification Reactions as Studied by Scanning Tunneling Microscopy". Journal of the American Chemical Society, 1990. 112: p. 4598-4599.

123. Chang, H. and Bard, A.J., "Scanning Tunneling Microscopy Studies of Carbon-Oxygen Reactions on Highly Oriented Pyrolytic Graphite". Journal of the American Chemical Society, 1991. 113: p. 5588-5596.

124. Stevens, F., Kolodny, L.A., and Beebe, T.P., "Kinetics of Graphite Oxidation: Monolayer and Multilayer etch pits in HOPG Studied by STM". Journal of Physical Chemistry B, 1998. 102: p. 10799-10804.

125. Patrick, D.L., Cee, V.J., and Beebe Jr., T.P., "Molecular Corrals for Studies of Monolayer Organic Films". Science, 1994. 265: p. 231-234.

126. Ghorishi, B. and Sedman, C.B., "Low Concentration Mercury Sorption Mechanisms and Control by Calcium-Based Sorbents: Application in Coal-Fired Processes". Journal of Air & waste management Association, 1998. 48: p. 1191-1198.

127. Ruthven, D.M., "Principles of Adsorption and Adsorption Processes". 1984, New York: John Willy & Sons, Inc.

128. Dandekar, A., Baker, R.T.K., and Vannice, M.A., "Characterization of Activated Carbon, Graphitized Carbon Fibers and Synthetic Diamond Powder Using TPD and DRIFTS." Carbon, 1998. 36(12): p. 1821-1831.

129. Stevens, F., Kolodny, L.A., and Beebe, J.P., "Kinetics of Graphite Oxidation: Monolayer and Multilayer Etch Pits in HOPG Studied by STM". Journal of Physical Chemistry B, 1998. 102: p. 10799-10804.

130. Gulett, B.K. and Jozewicz, W., "Bench-scale Sorption and Desorption of Mercury with Activated Carbon". 1993 International Conference on Municipal Waste Combustion, Williamsburgh, VA, 1993.

131. Bacon, R. and Tang, M.M., "Carbonization of Cellulose Fibers-II Physical Property Study". Carbon, 1964. 2: p. 221-226.

132. Huggins, F.E., Huffman, G.P., Dunham, G.E., and Senior, C.L., "XAFS Examination of Mercury Sorption on Three Activated Carbons". Energy & Fuels, 1999. 13: p. 114-121.

133. Borghiesi, A. and Guizzetti, G., "Handbook of Optical Constants of Solids II, edited by E. D. Palik". 1991, New York: Academic Press. 449.

FIGURES

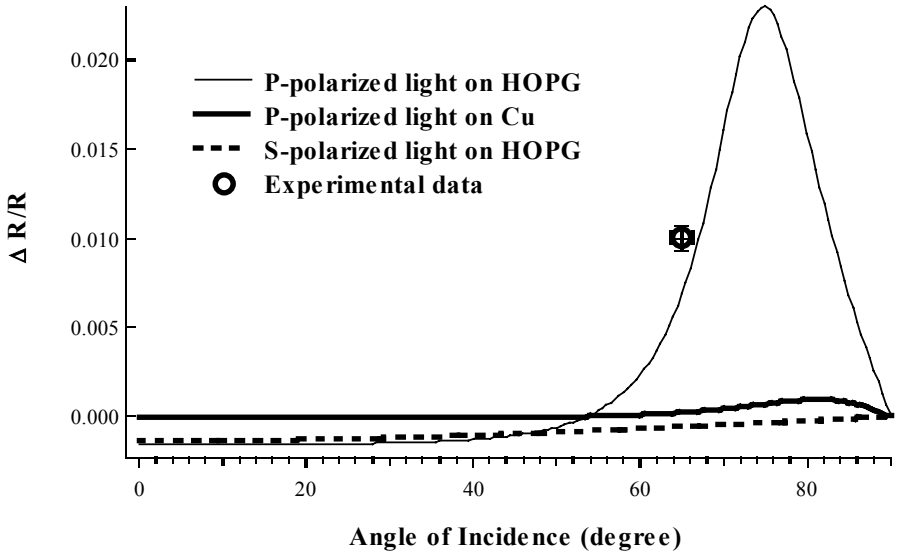

Figure 2-1. Normalized difference in p-polarized reflectivity for a 5 Å layer of acetone on HOPG ($\varepsilon_3 = 5.04+i8.4$) and Cu ($\varepsilon_3 = -13.33+i1.24$) as a function of the angle of incidence at $\lambda = 655$ nm. The lines are prediction from equation 4-2.

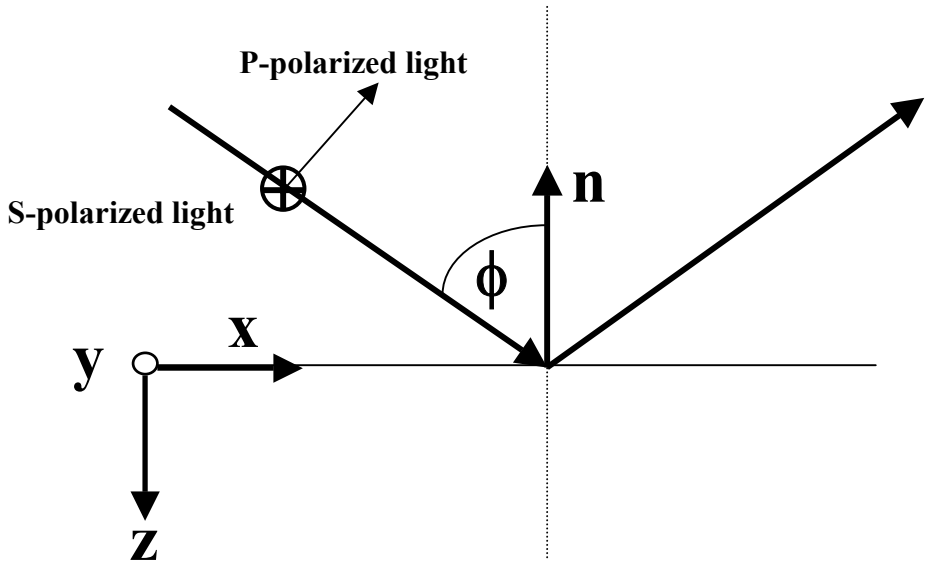

Figure 2-2. Coordinate system describing the polarization state of light.

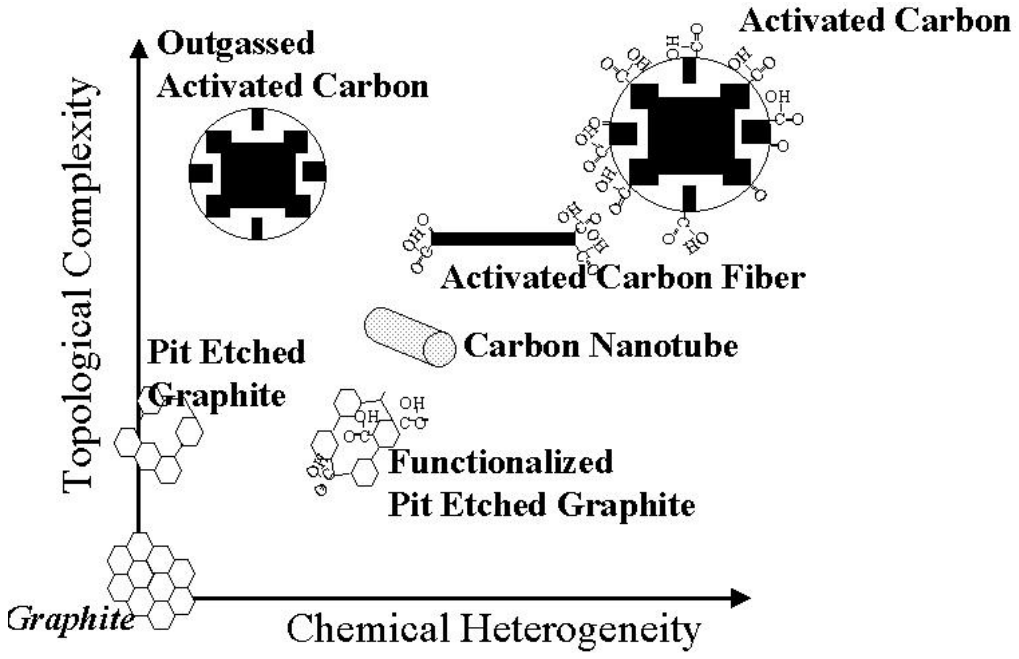

Figure 2-3. Schematic view of various carbon materials

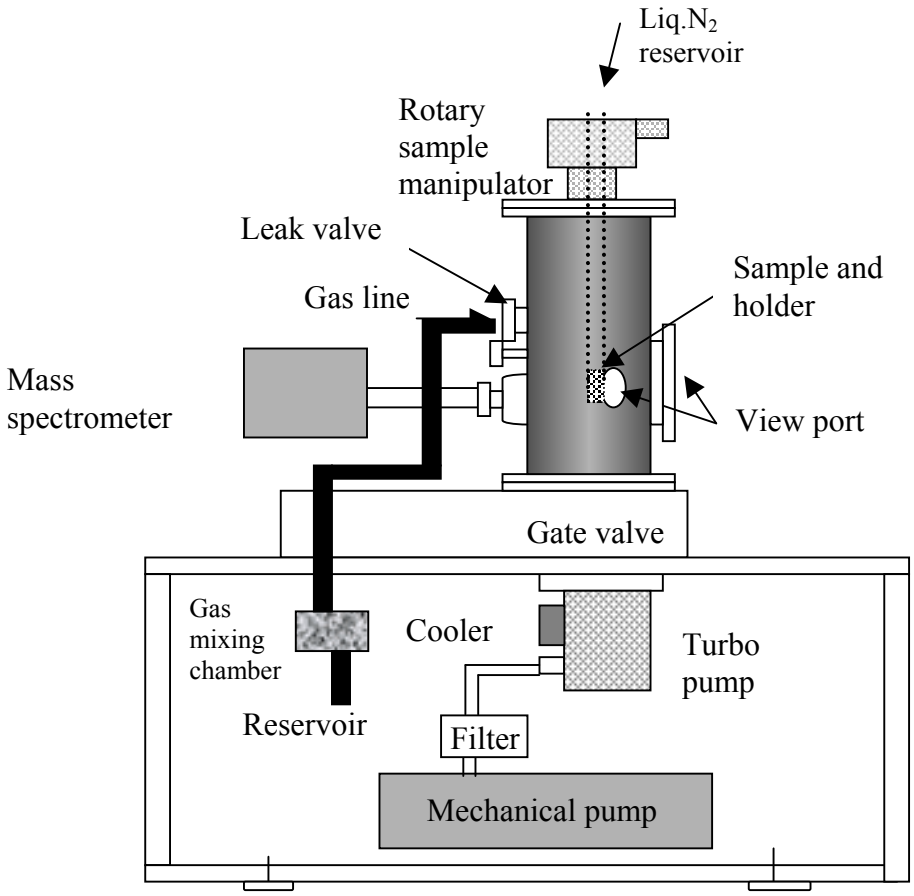

Figure 3-1. Schematic of the UHV chamber and gas handling unit

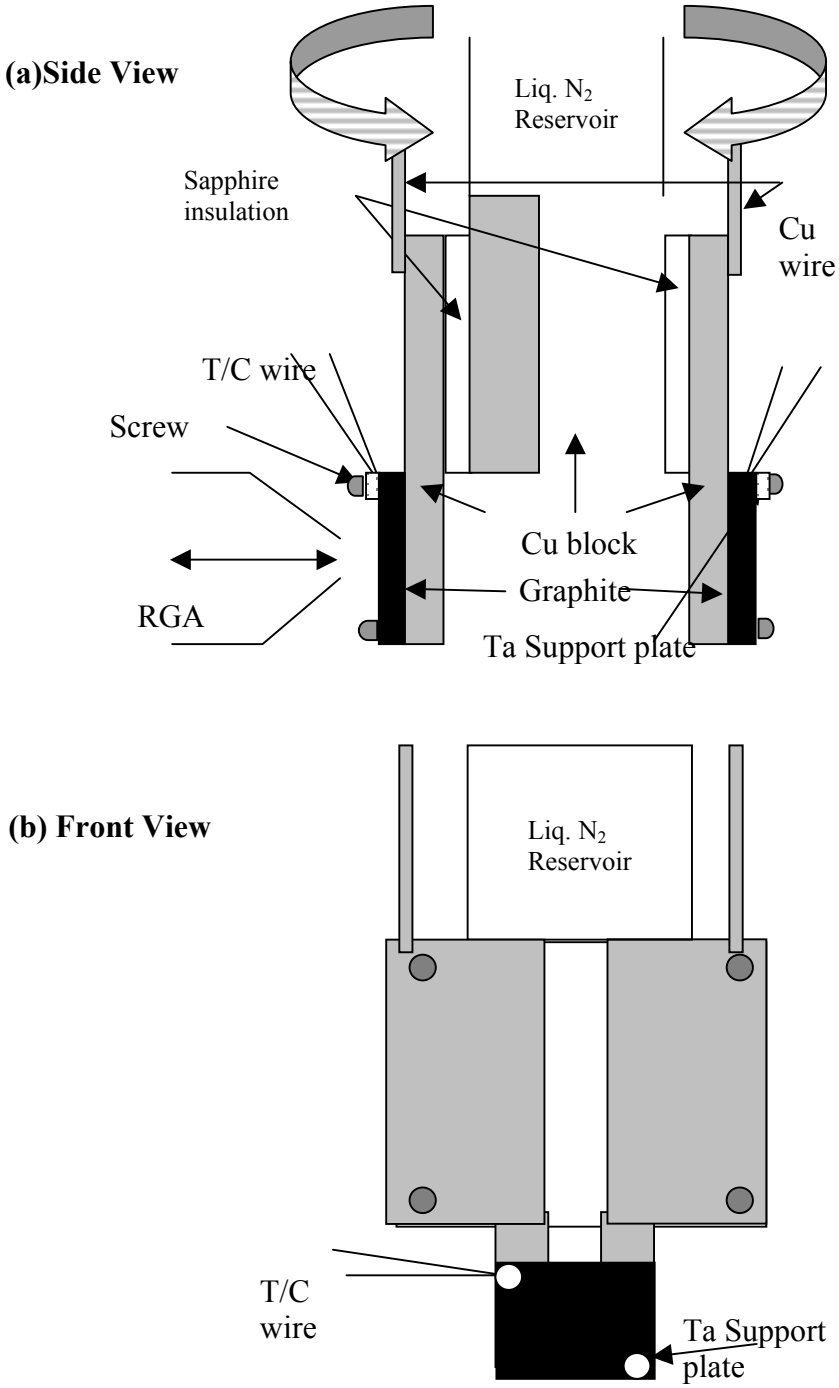

Figure 3-2. Schematic of the dual sample mount : (a) side view and (b) front view

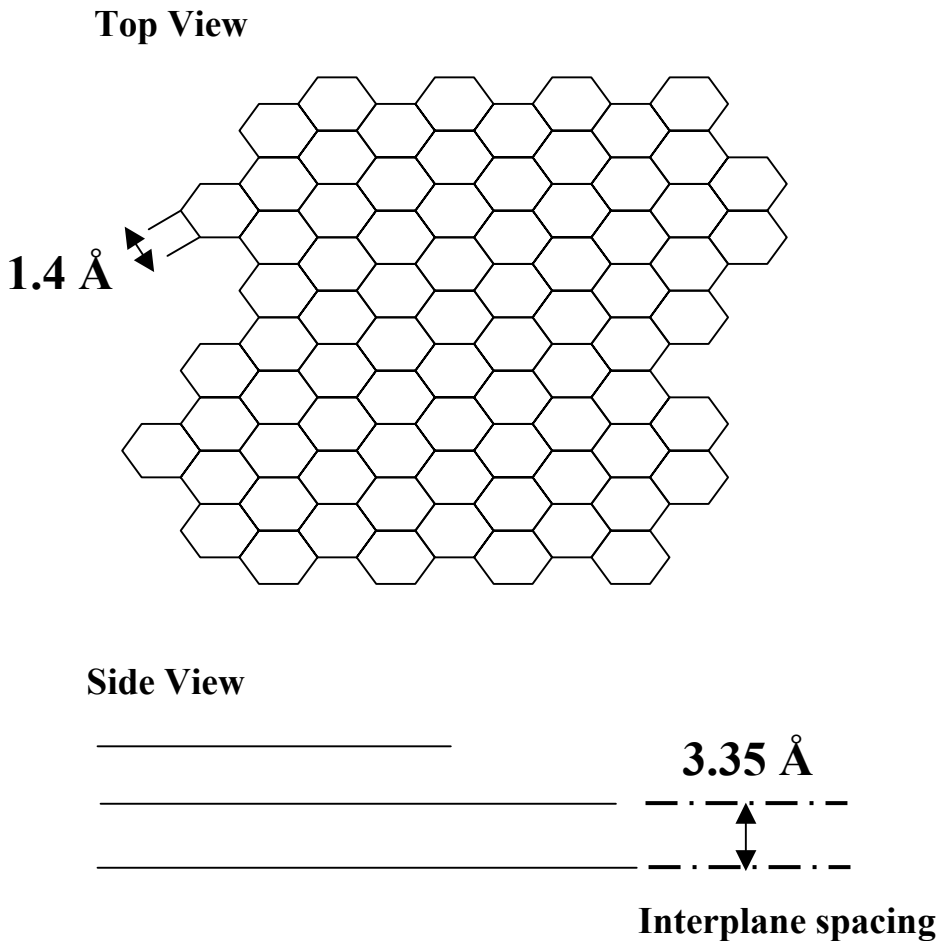

Figure 3-3. Structure of HOPG. HOPG is a relatively new form of high purity carbon consisting of planes of well-defined honeycomb structure.

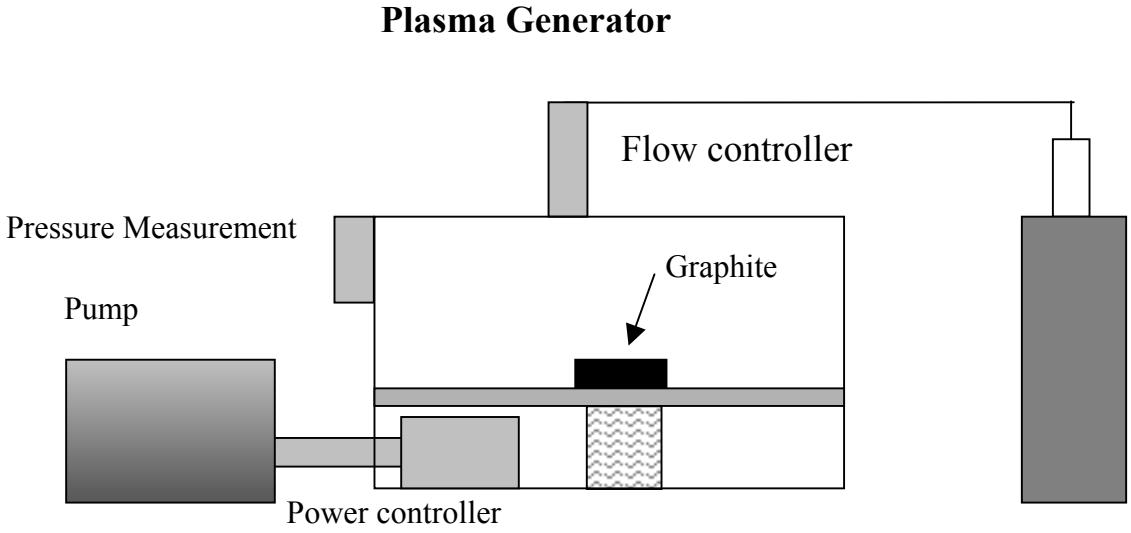

Figure 3-4. Schematic of O_2 plasma system

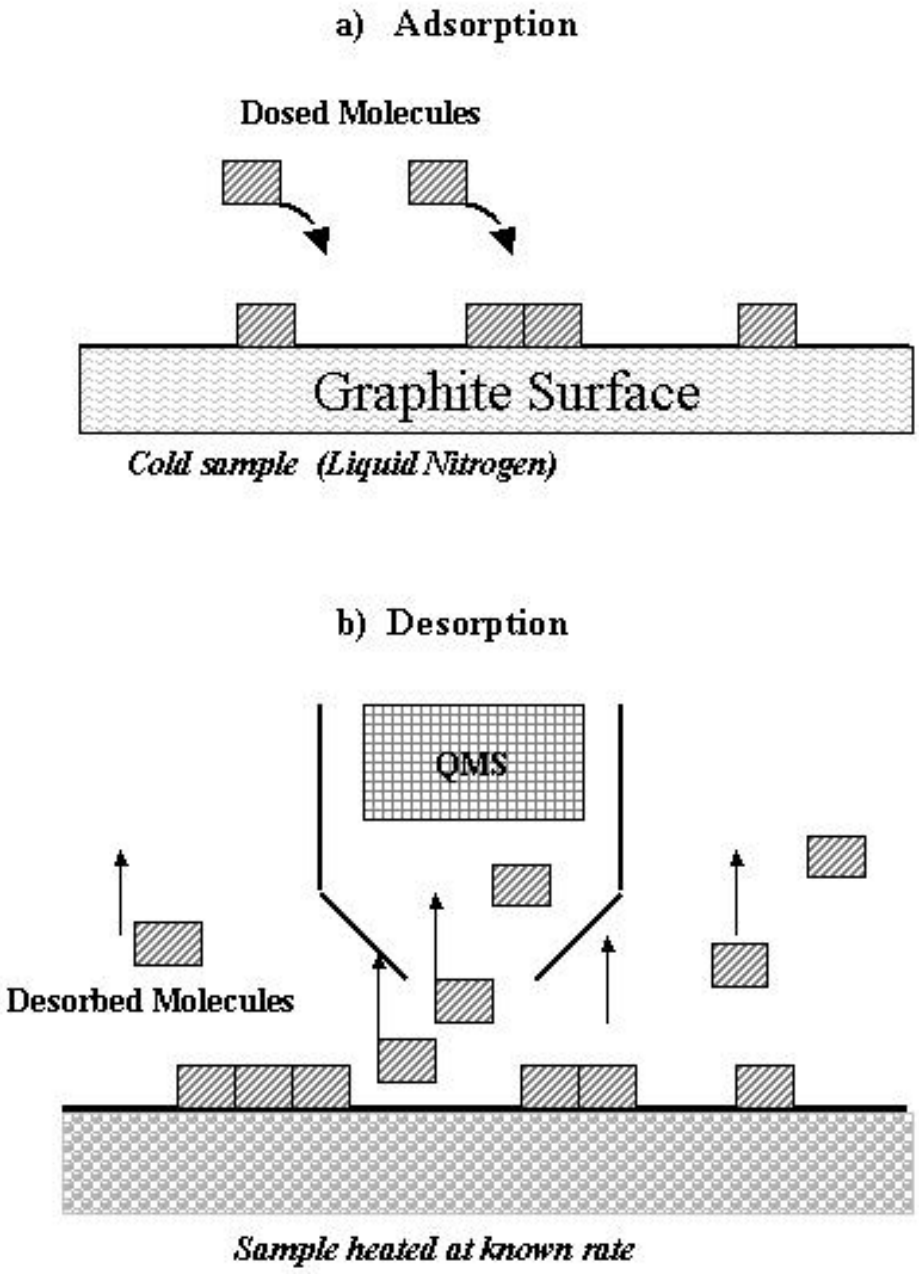

Figure 3-5. Experimental procedure for TPD experiments

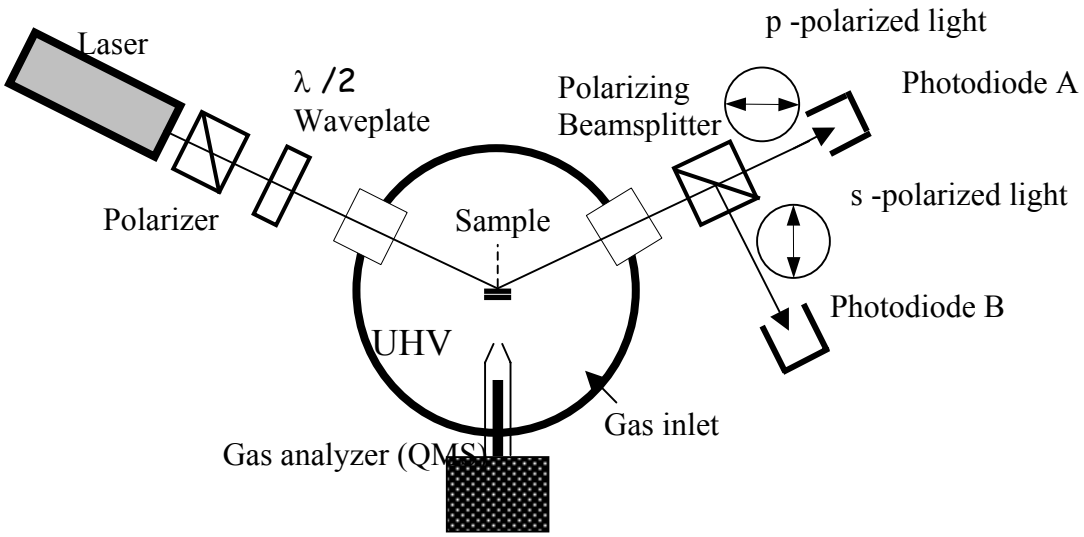

Figure 3-6. Optical differential reflectance (ODR) System

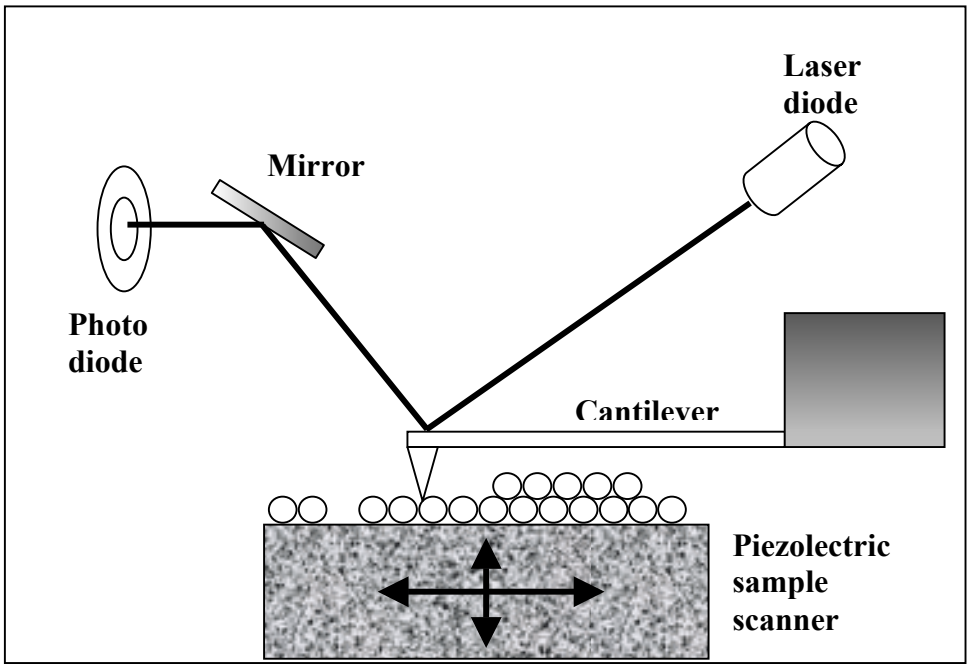

Figure 3-7. Schematic view of AFM imaging

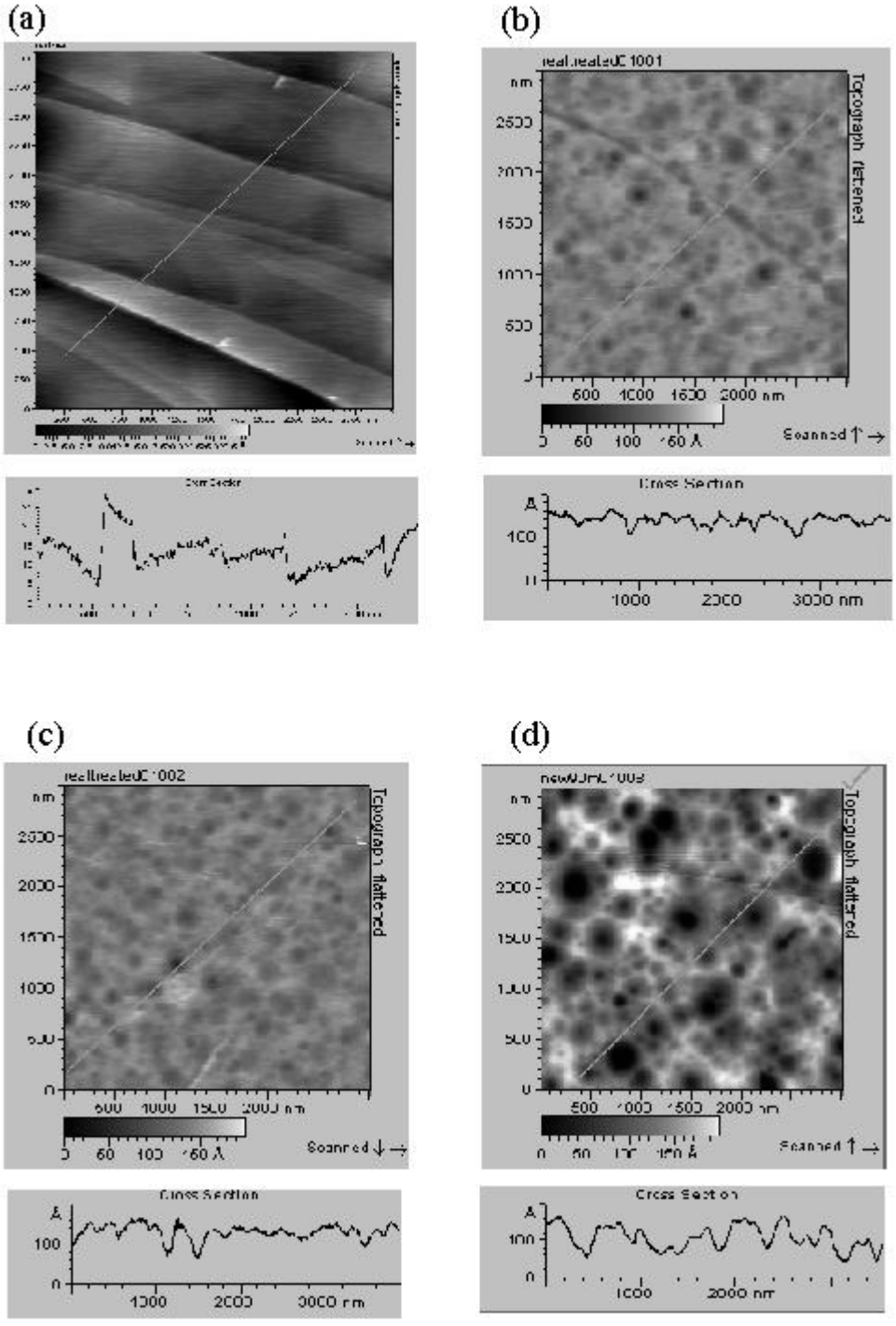

Figure 3-8. AFM images for (a) virgin HOPG, (b) and (c) O_2 plasma oxidized HOPG for 20 min (d) for 90 min. Graphs under the images show cross sectional in height

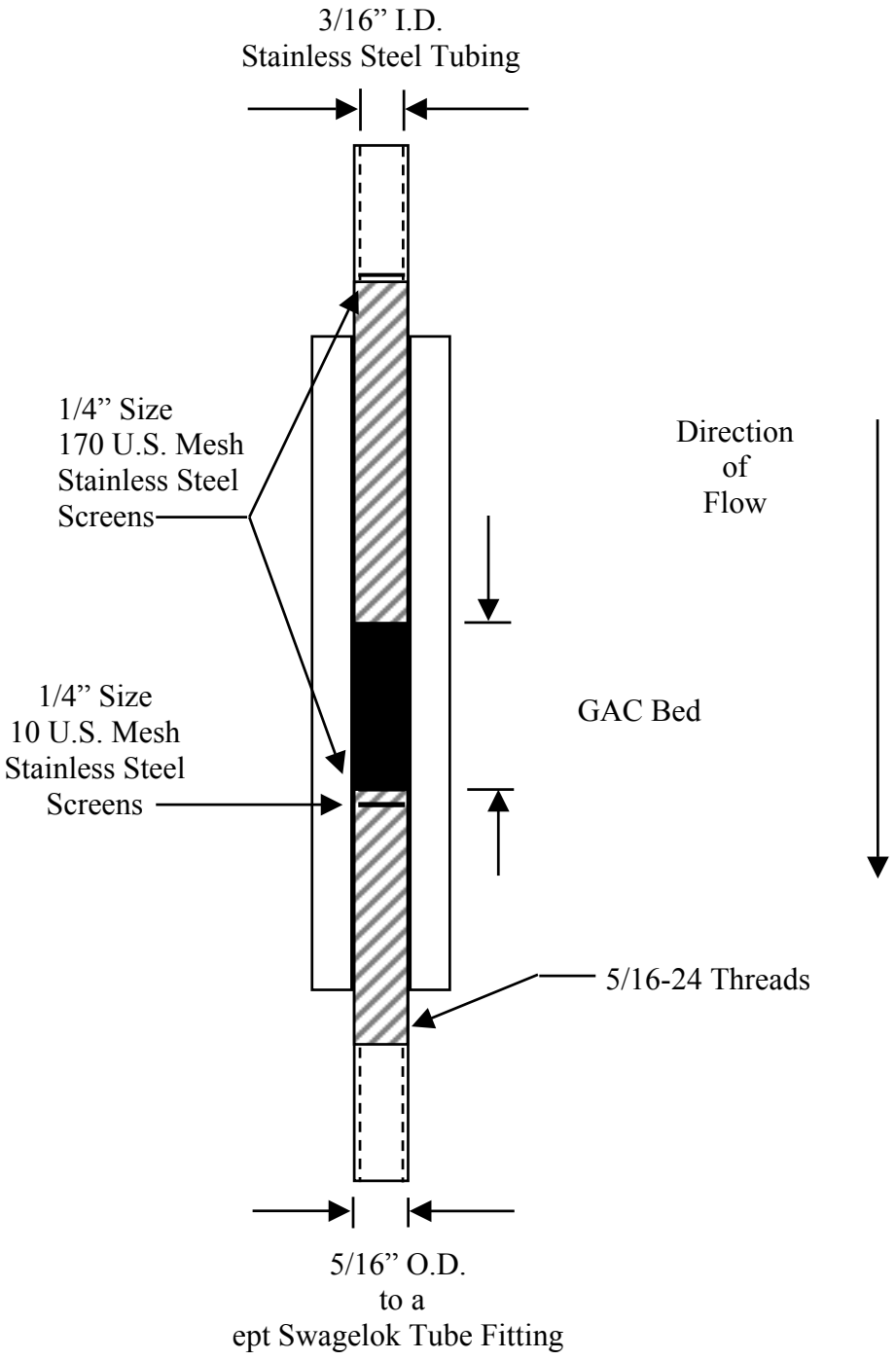

Figure 3-9. Setup of the fixed-bed adsorber

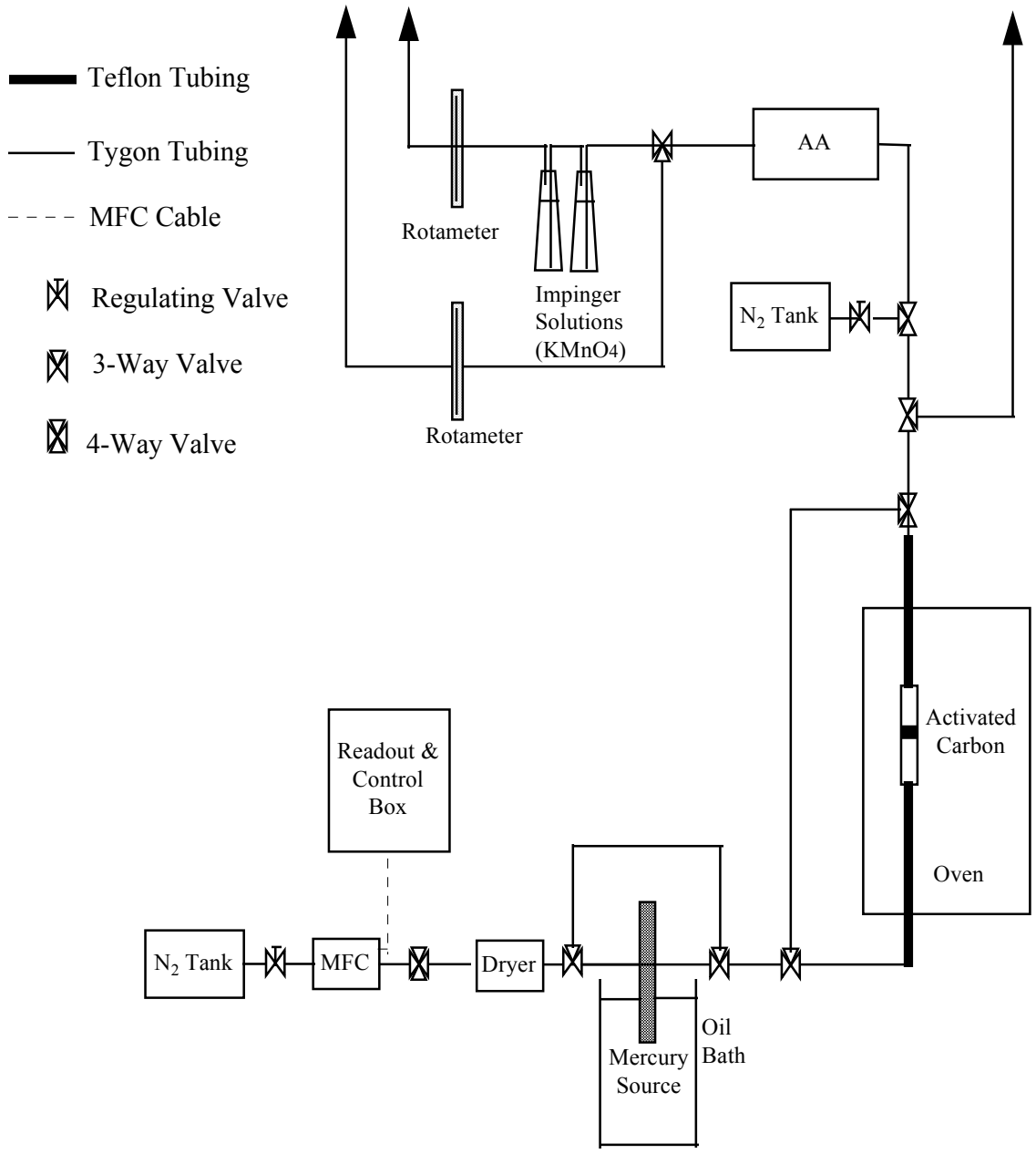

Figure 3-10. Experimental system for fixed-bed breakthrough tests

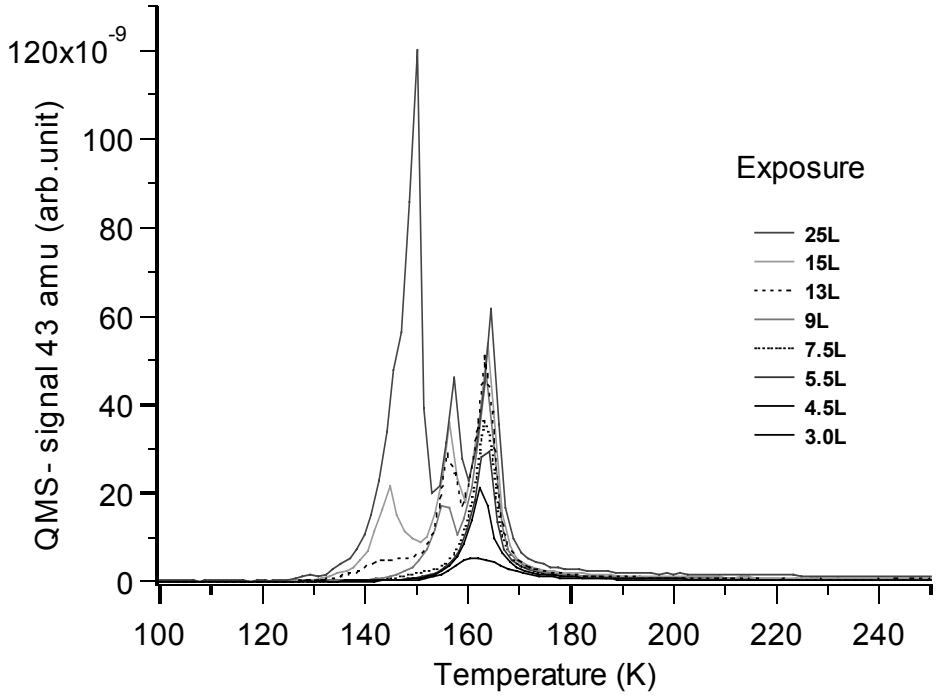

Figure 4-1. TPD spectra for acetone on HOPG at 91 K (temperature ramp at 2.5 K/sec)

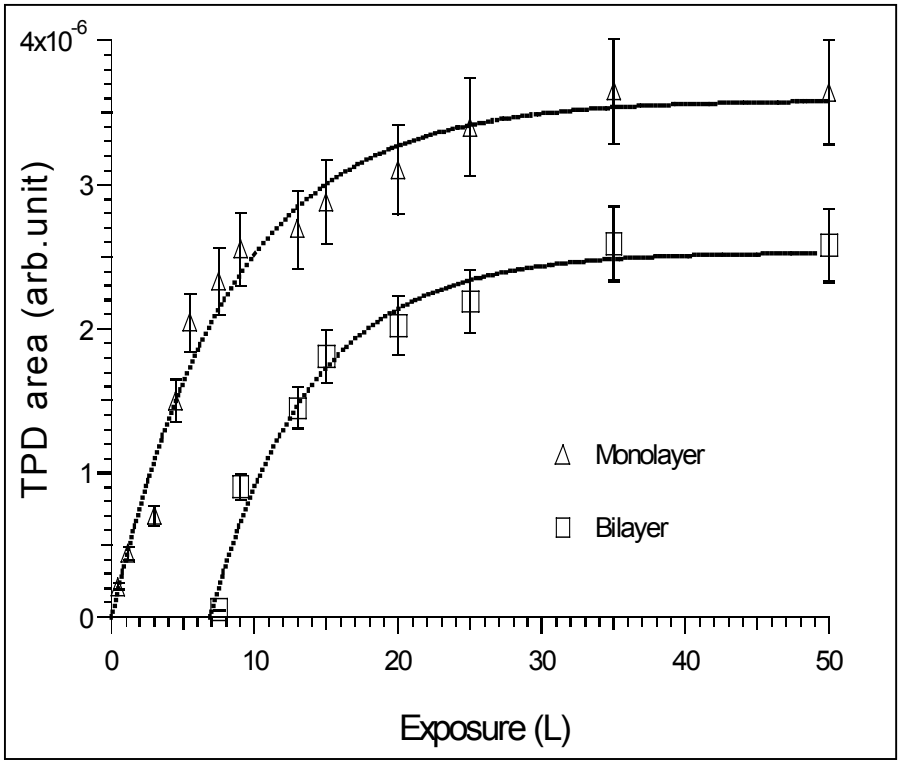

Figure 4-2. Integrated area of monolayer and bilayer of TPD features. The dotted lines are model fits assuming that adsorption follows Langmuir kinetics

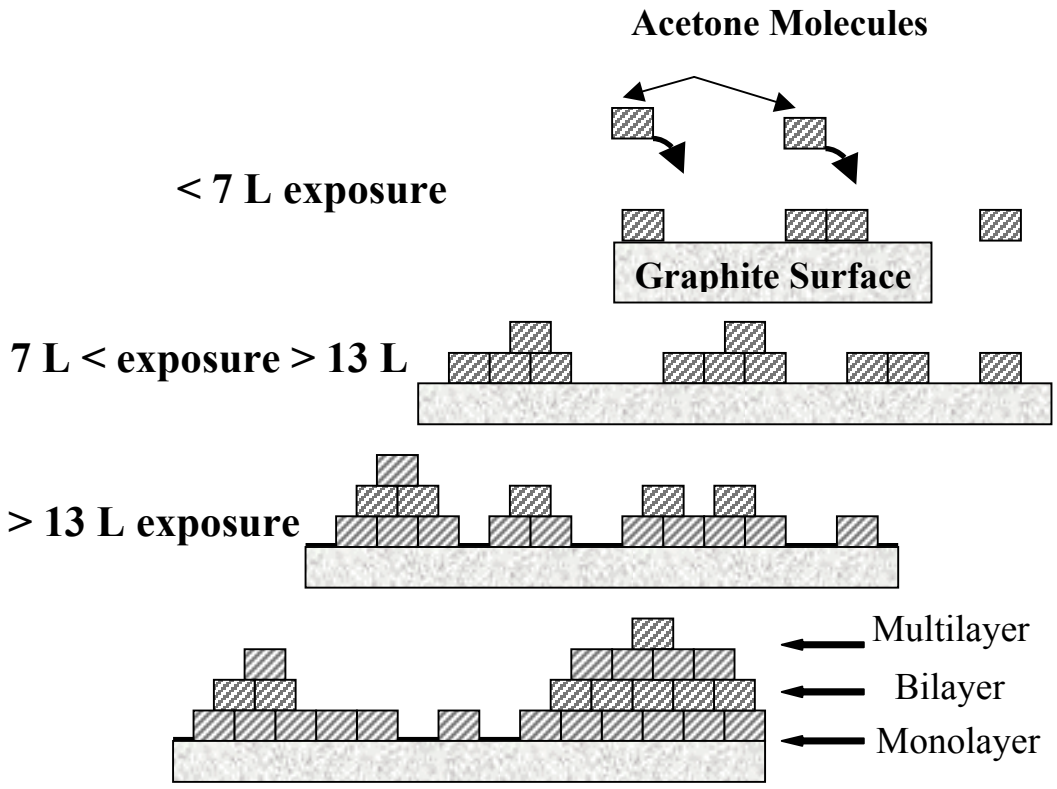

Figure 4-3. Schematic of the proposed growth model (Volmer- Weber) of acetone on graphite at 91 K

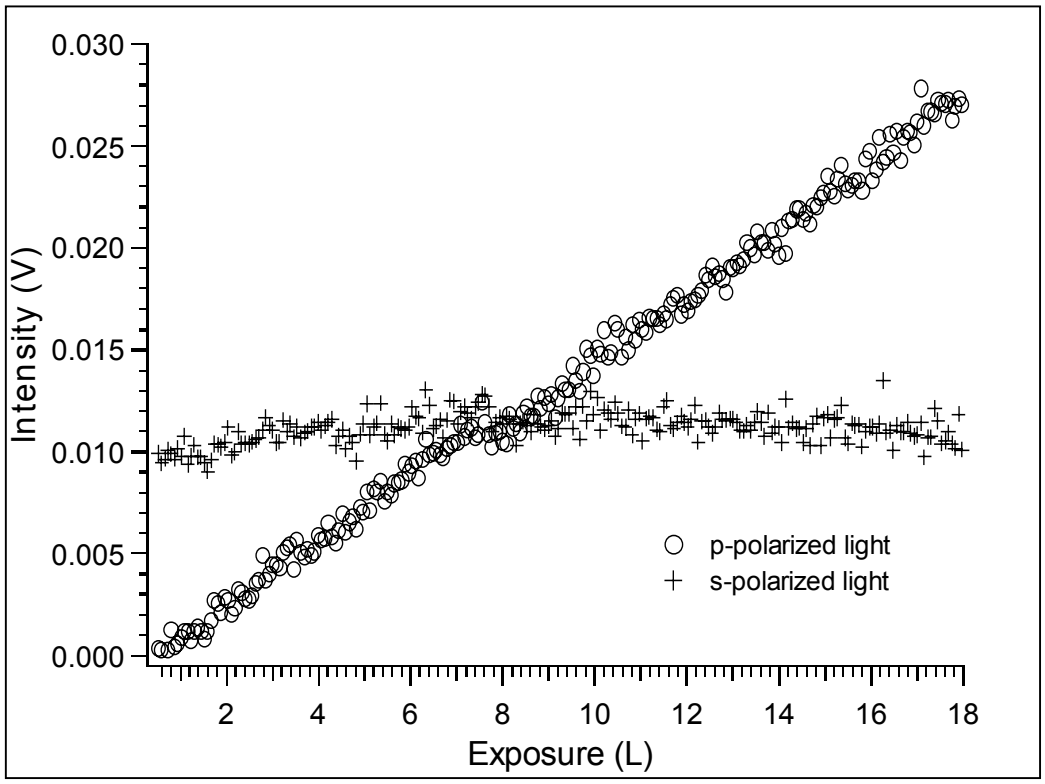

Figure 4-4. Intensity of s and p-polarized light reflected from HOPG as a function of exposure induced by acetone adsorption at 1.2×10^{-7} torr and 91 K

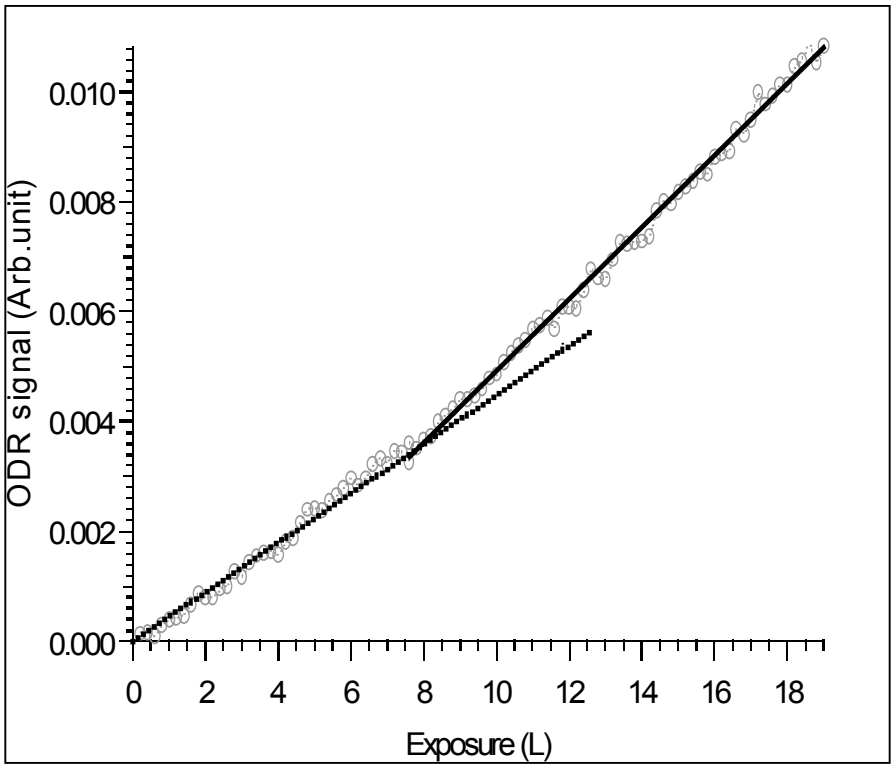

Figure 4-5. ODR signal as a function of acetone exposure at 91 K

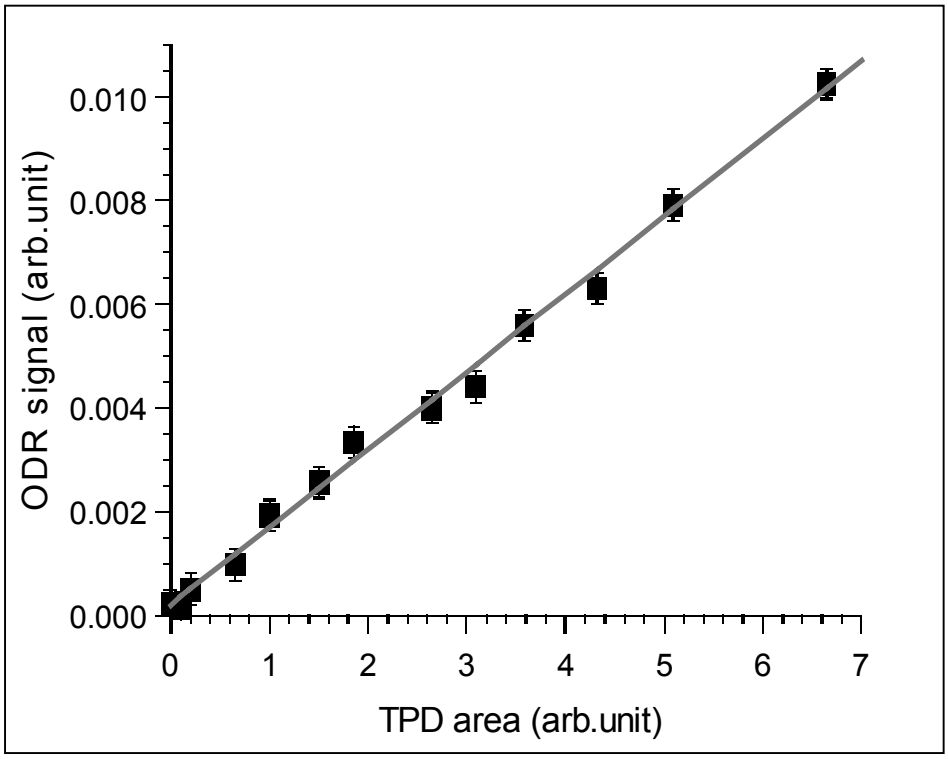

Figure 4-6. Correlation between ODR and TPD experiments for acetone adsorption on graphite. The solid line is a linear fit of experimental data (R^2=0.995)

(a)

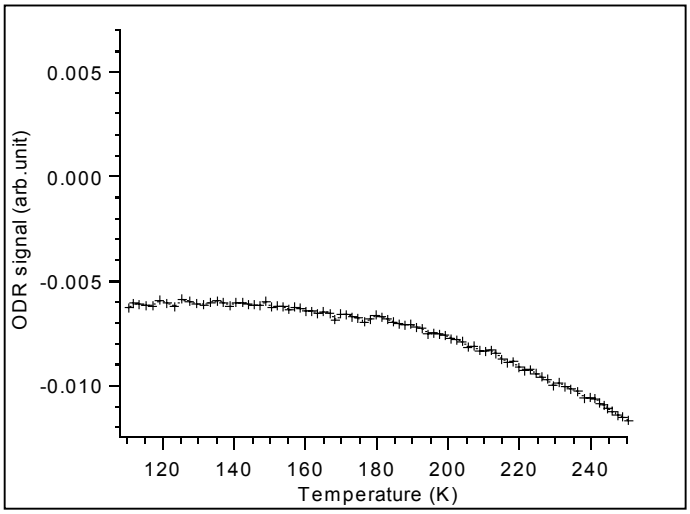

(b)

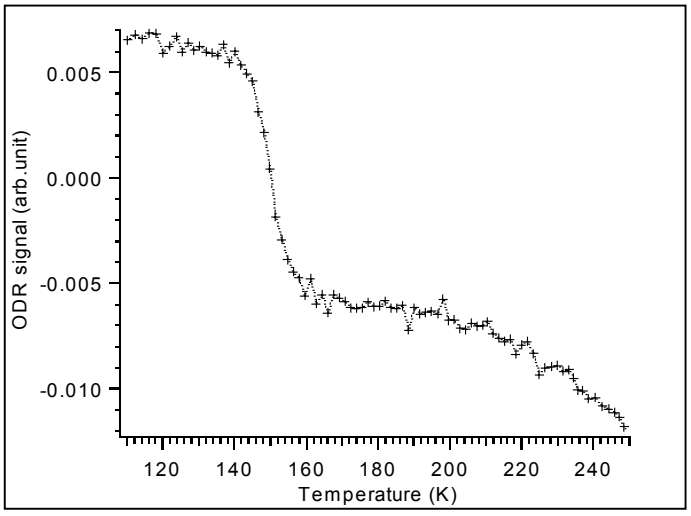

Figure 4-7. (a) Background ODR signal for a clean surface (b) ODR signal during thermal desorption for a surface containing pre-adsorbed acetone

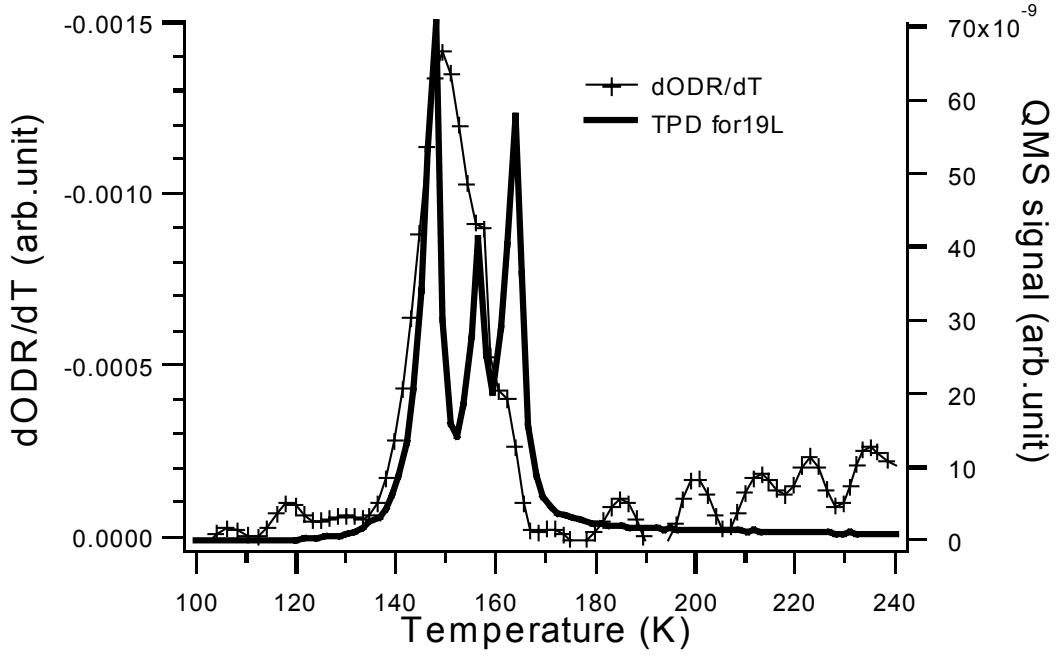

Figure 4-8. d(ODR)/dT and TPD spectra as a function of temperature for graphite initially exposed acetone at 19L.

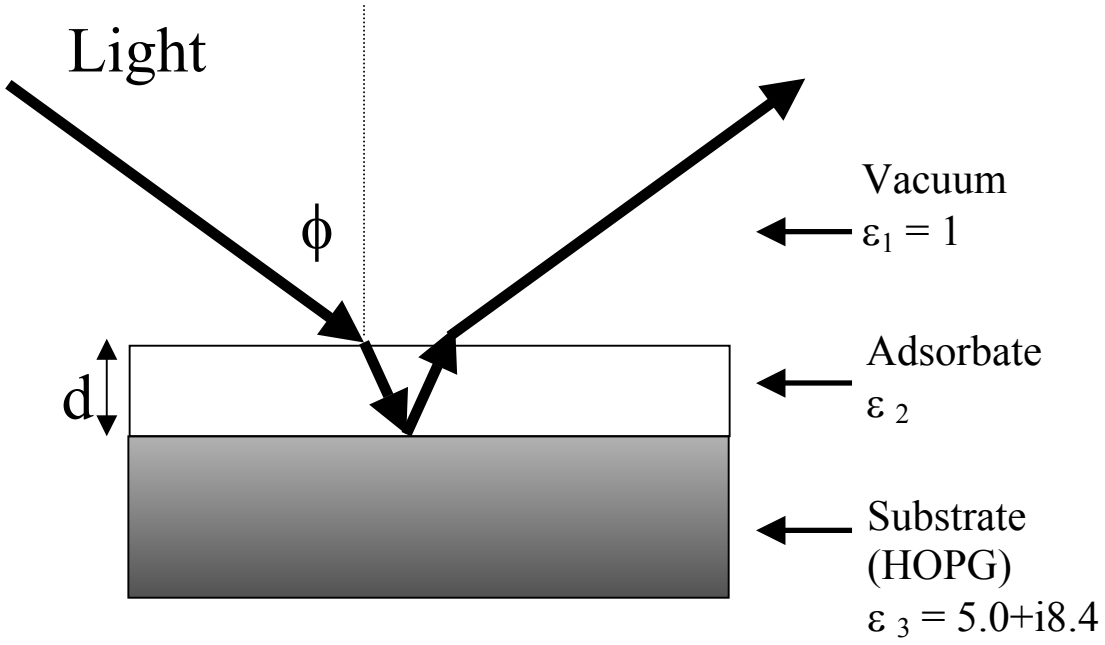

Figure 4-9. Schematic view of the three layer model. Each layer is described by its dielectric constant (ε_i). d is the adsorbate overlayer thickness, ϕ is the angle of incidence

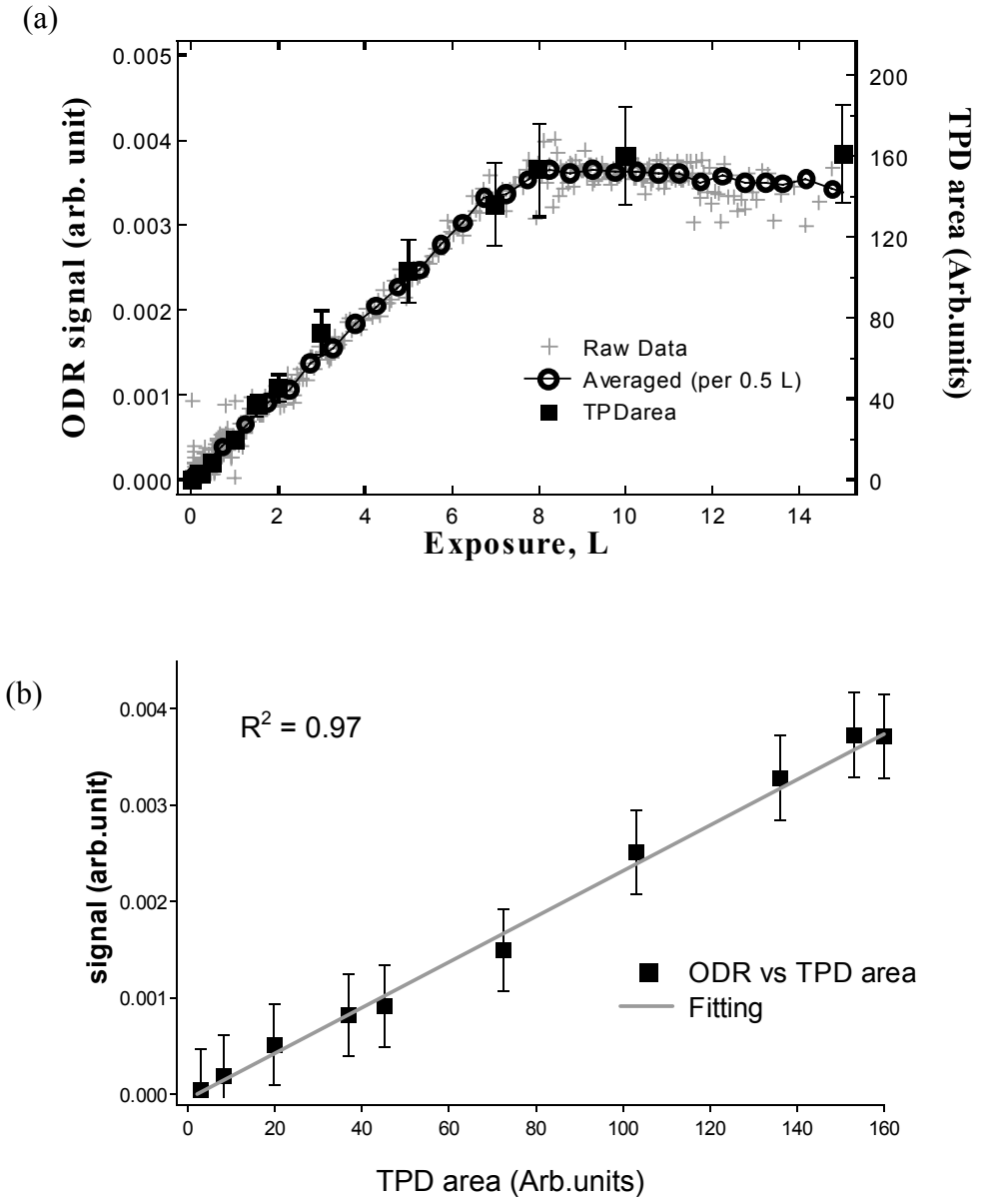

Figure 4-10. ODR signal and TPD area resulting from adsorption of propane on graphite at 100 K as a function of exposure (a) and the correlation between ODR and TPD (b).

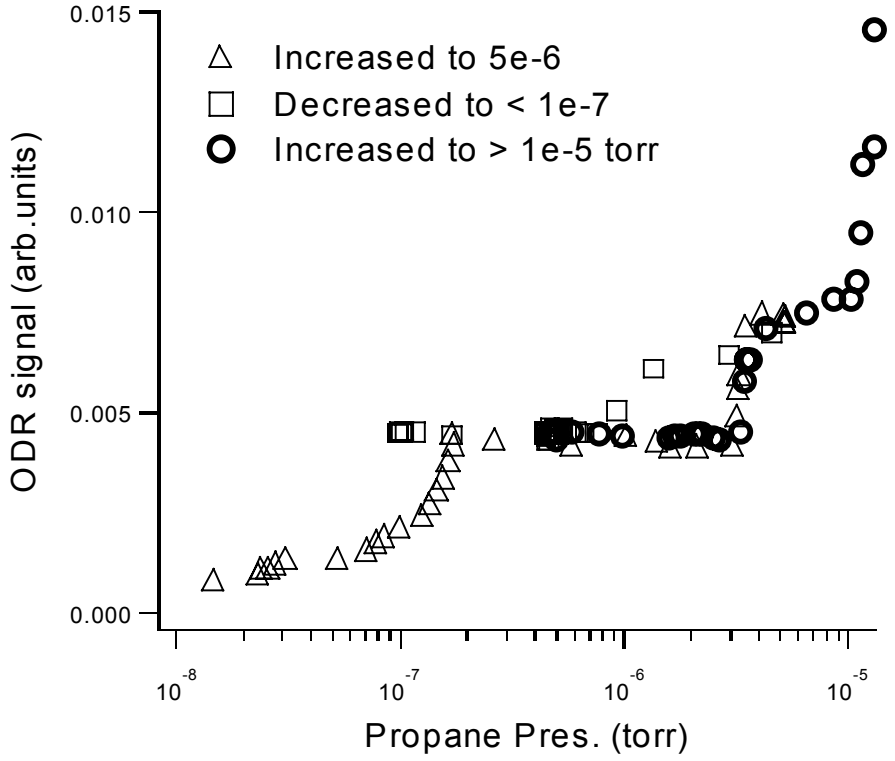

Figure 4-11. Propane adsorption on graphite at 90 K : ODR as a function of propane pressure

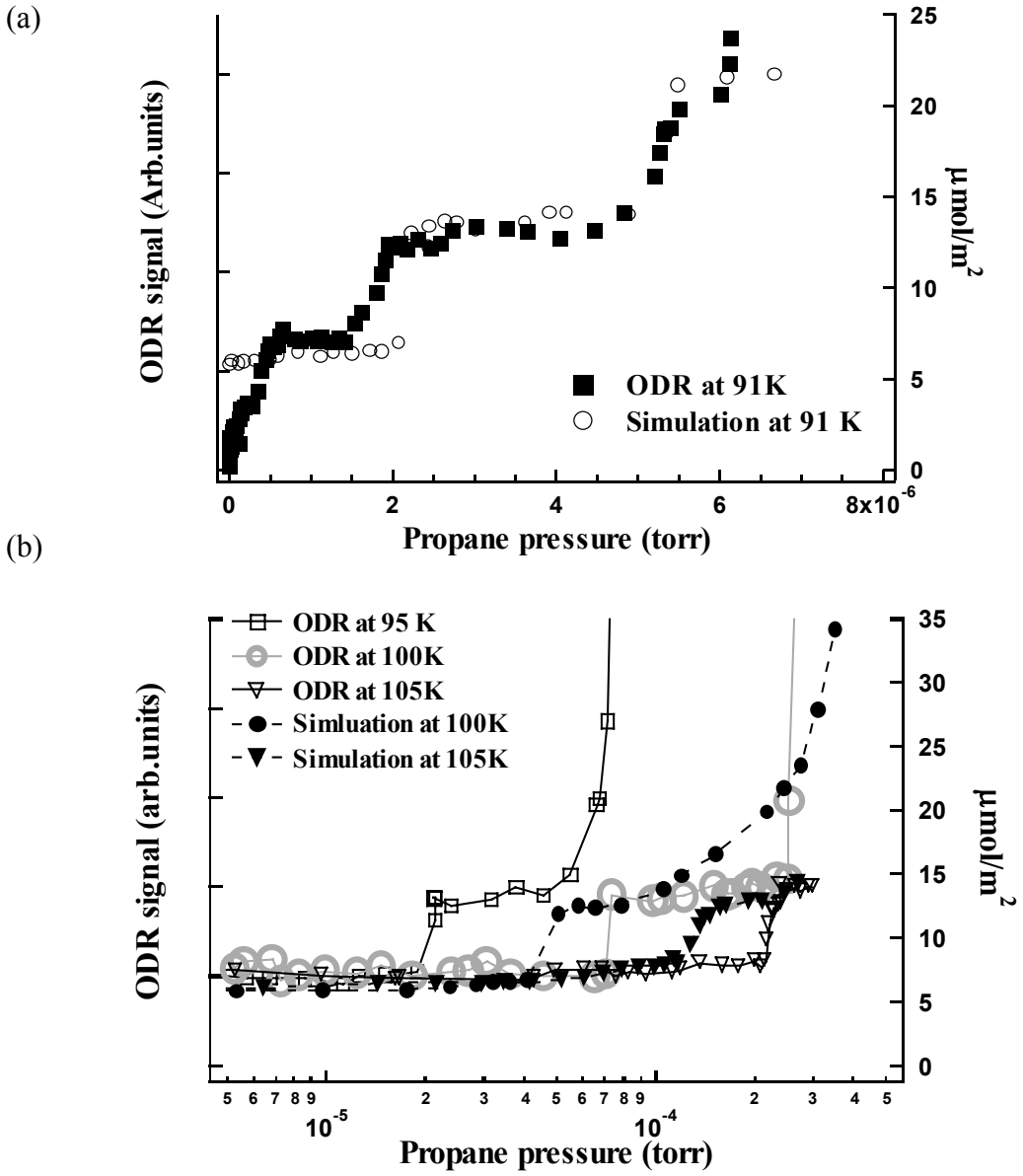

Figure 4-12. Propane adsorption on graphite at (a) 90 and (b) 95, 100 and 105 K determined from ODR and molecular simulation as a function of propane pressure[112]

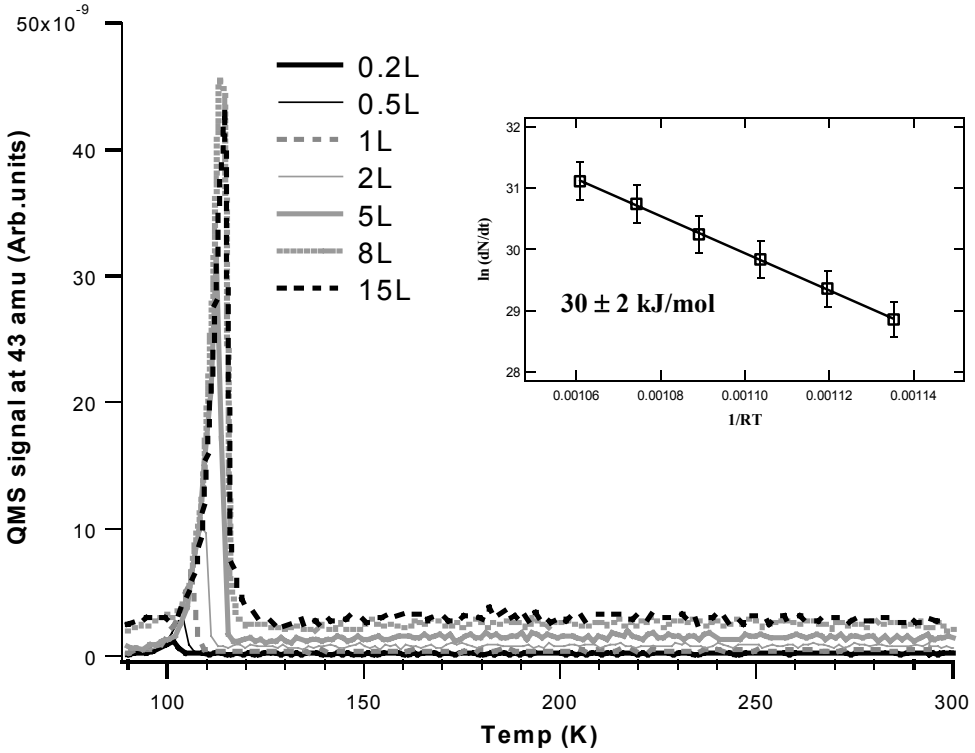

Figure 4-13. TPD of propane adsorption on HOPG at 90 K (temperature ramp at 2.5 K/sec)

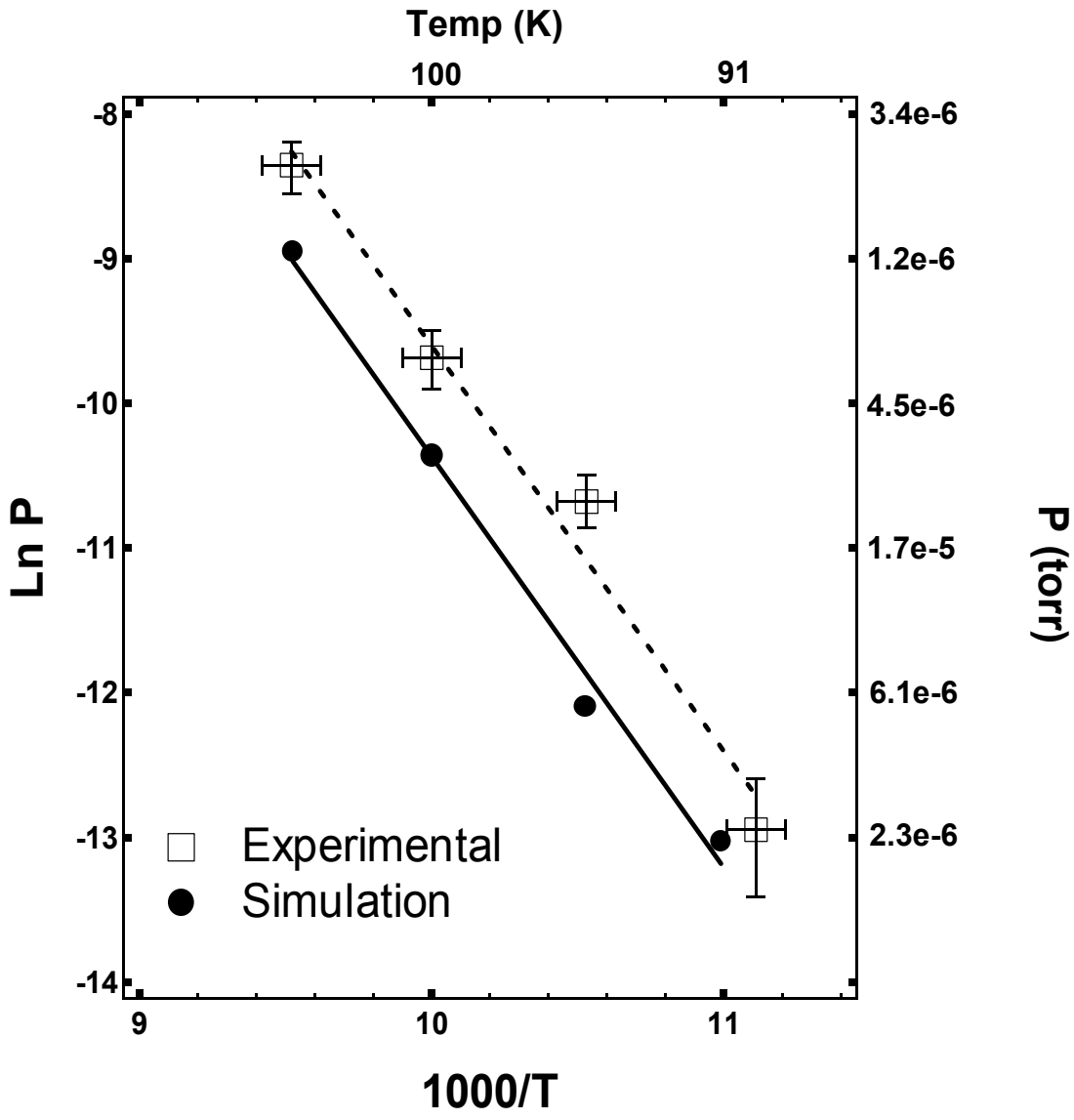

Figure 4-14. Plots of the ln P versus 1/T. This approach reveals that the bilayer heat of adsorption of propane on graphite is 23 ± 2 kJ/mol

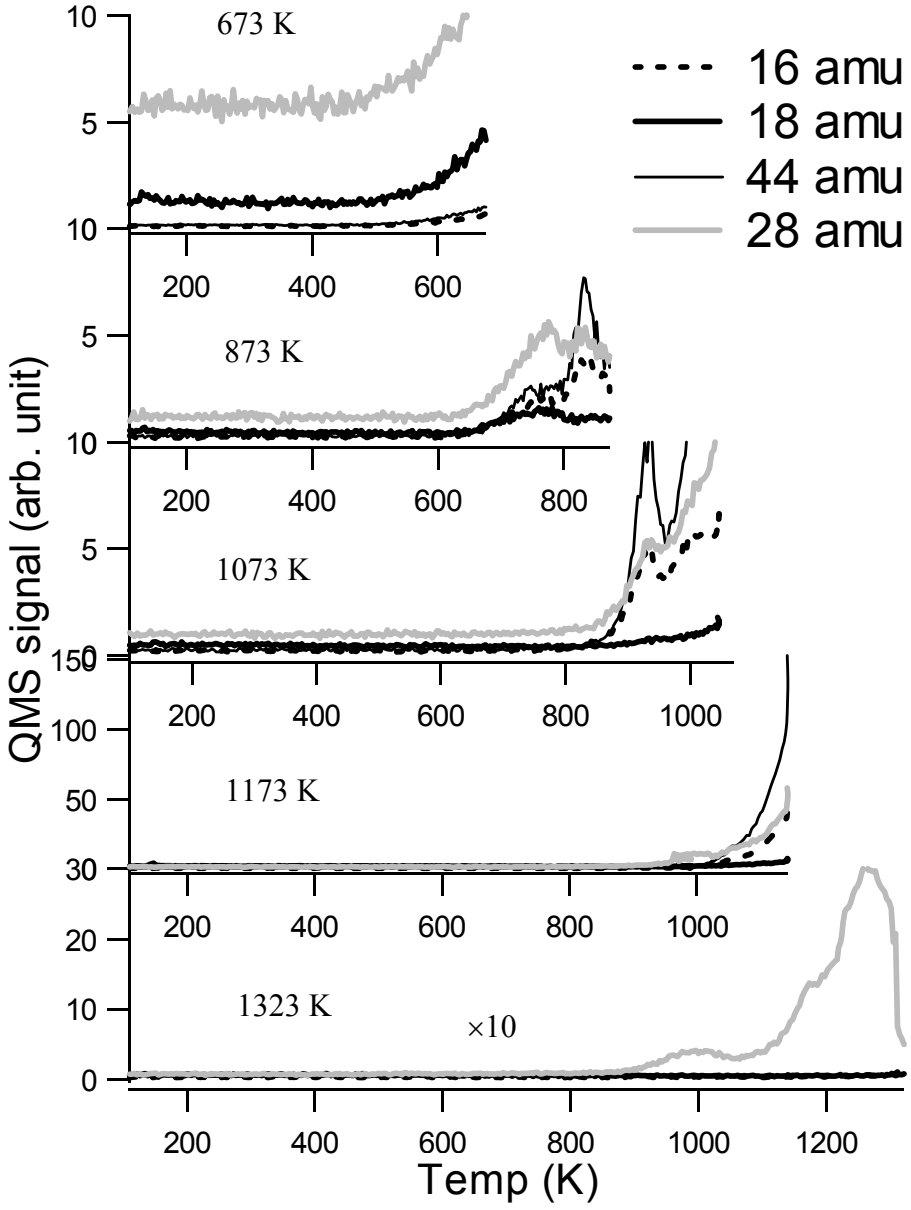

Figure 4-15. Evolution of masses 16, 18, 28 and 44 amu during initial heat treatment of air-cleaved HOPG to different temperatures. Data for 16, 18 and 44 amu in the 1323 K scan are multiplied by 10 to aid in viewing

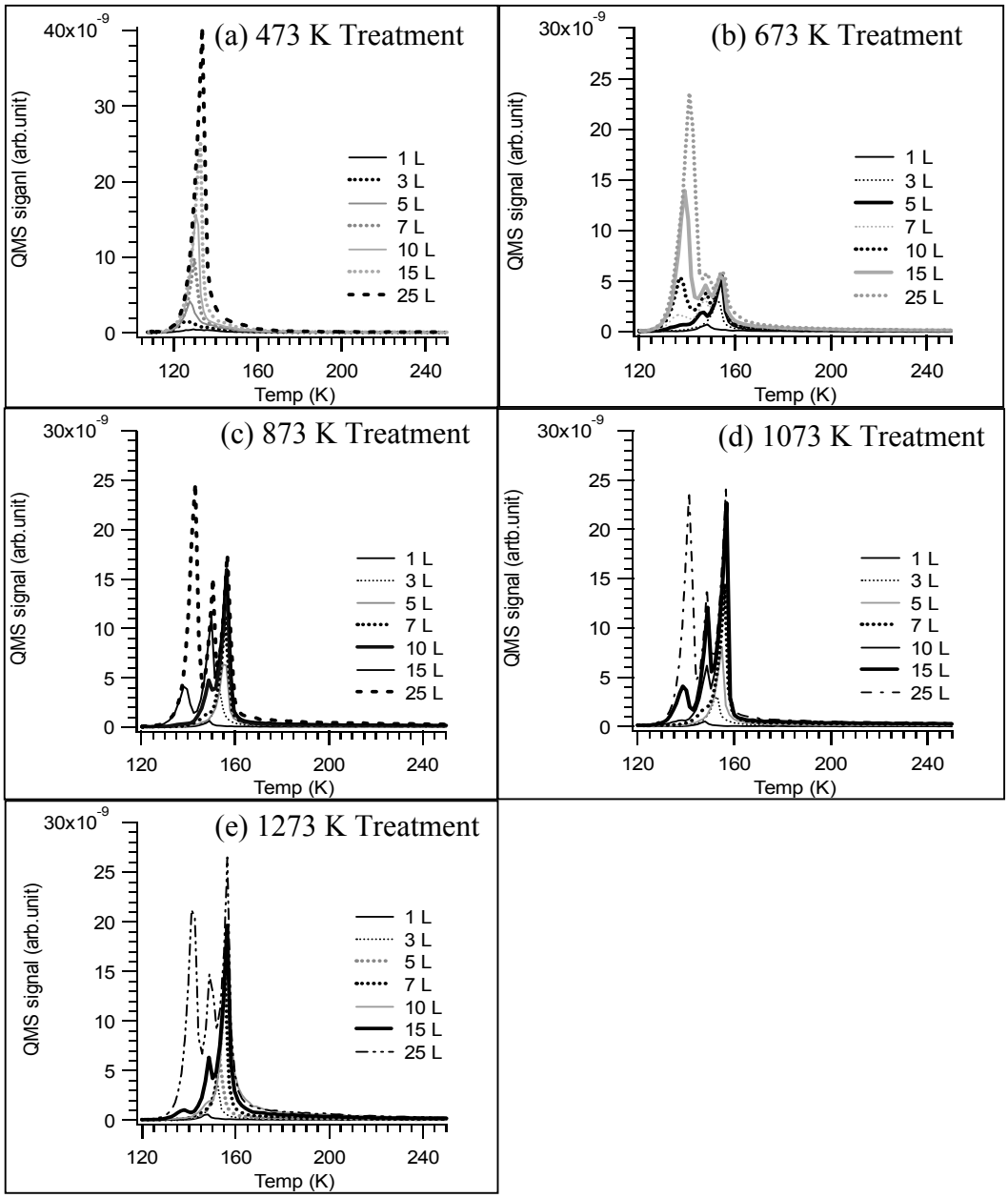

Figure 4-16. TPD spectra of acetone on HOPG after heat treatment at various temperatures. Note that identical vertical scales are used for all figures except for 473 K.

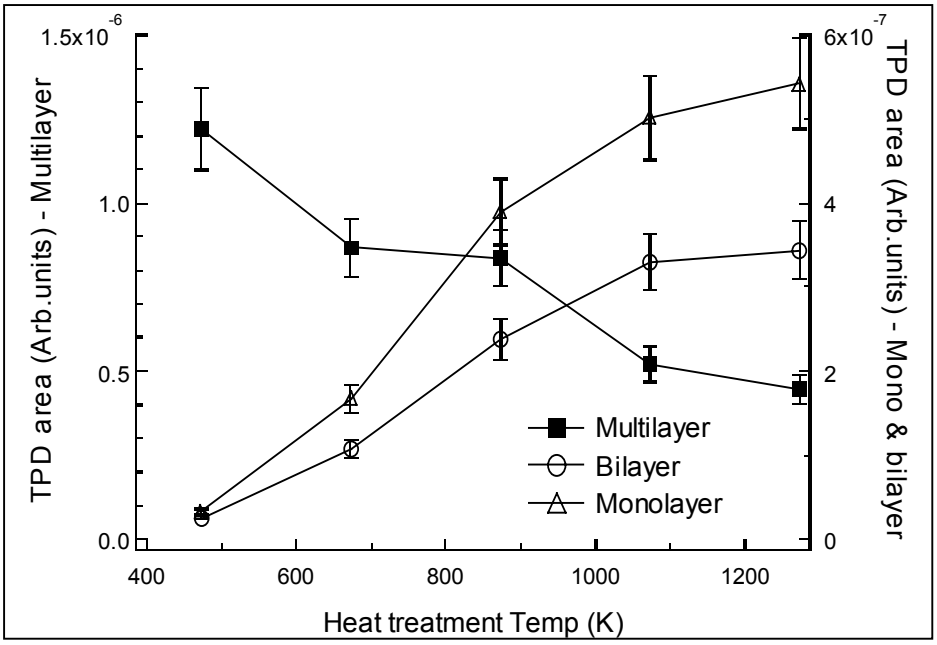

Figure 4-17. Area of each individual TPD peak. Areas were obtained by the deconvolution of TPD spectra for 25 L exposure.

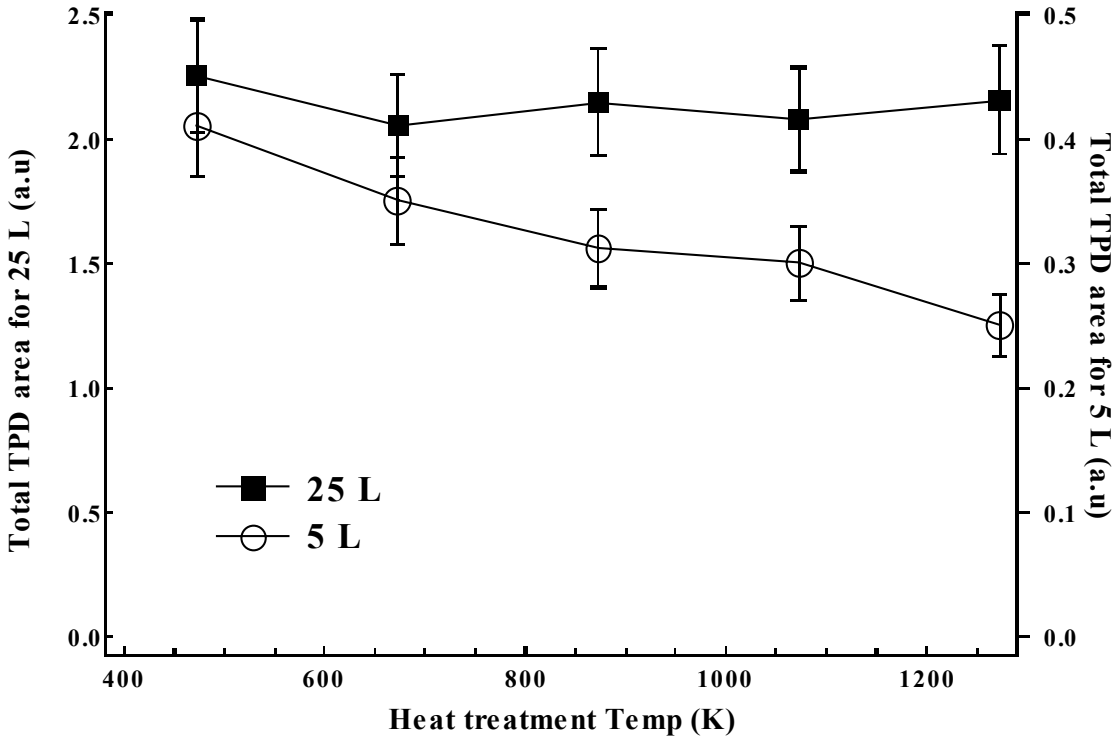

Figure 4-18. Total area of TPD spectra for 25 L and 5 L exposure as a function of heat treatment temperature.

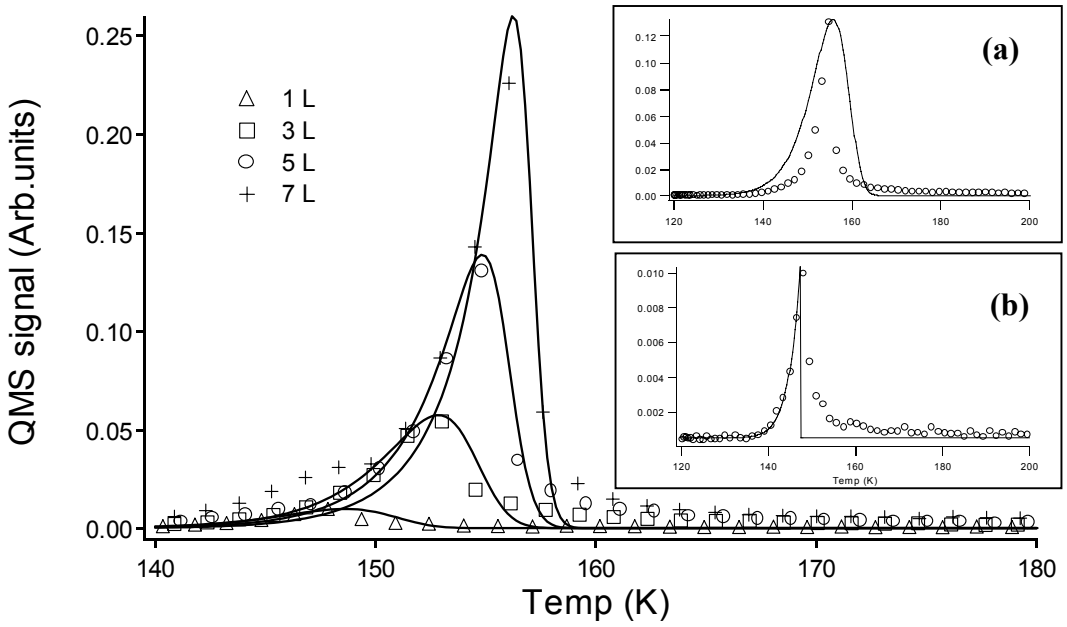

Figure 4-19. Experimental (symbols) and simulated (lines) TPD of acetone monolayer. The insert (a) shows the fitting using conventional pre-exponential factor (10^{13} sec^{-1}) for 7 L exposure and insert (b) shows a fitting trial with zero order for 3 L exposure.

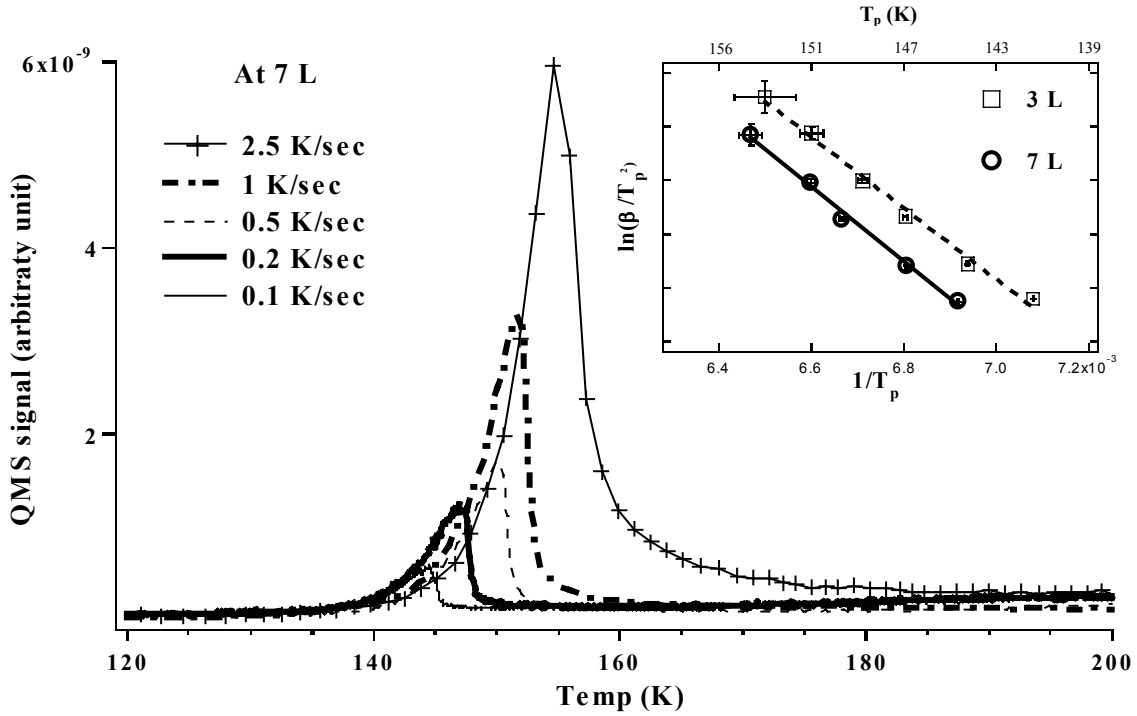

Figure 4-20. Acetone TPD for 7L exposure at different heating rates. The insert shows a graph of $\ln(\beta/Tp^2)$ versus $1/Tp$

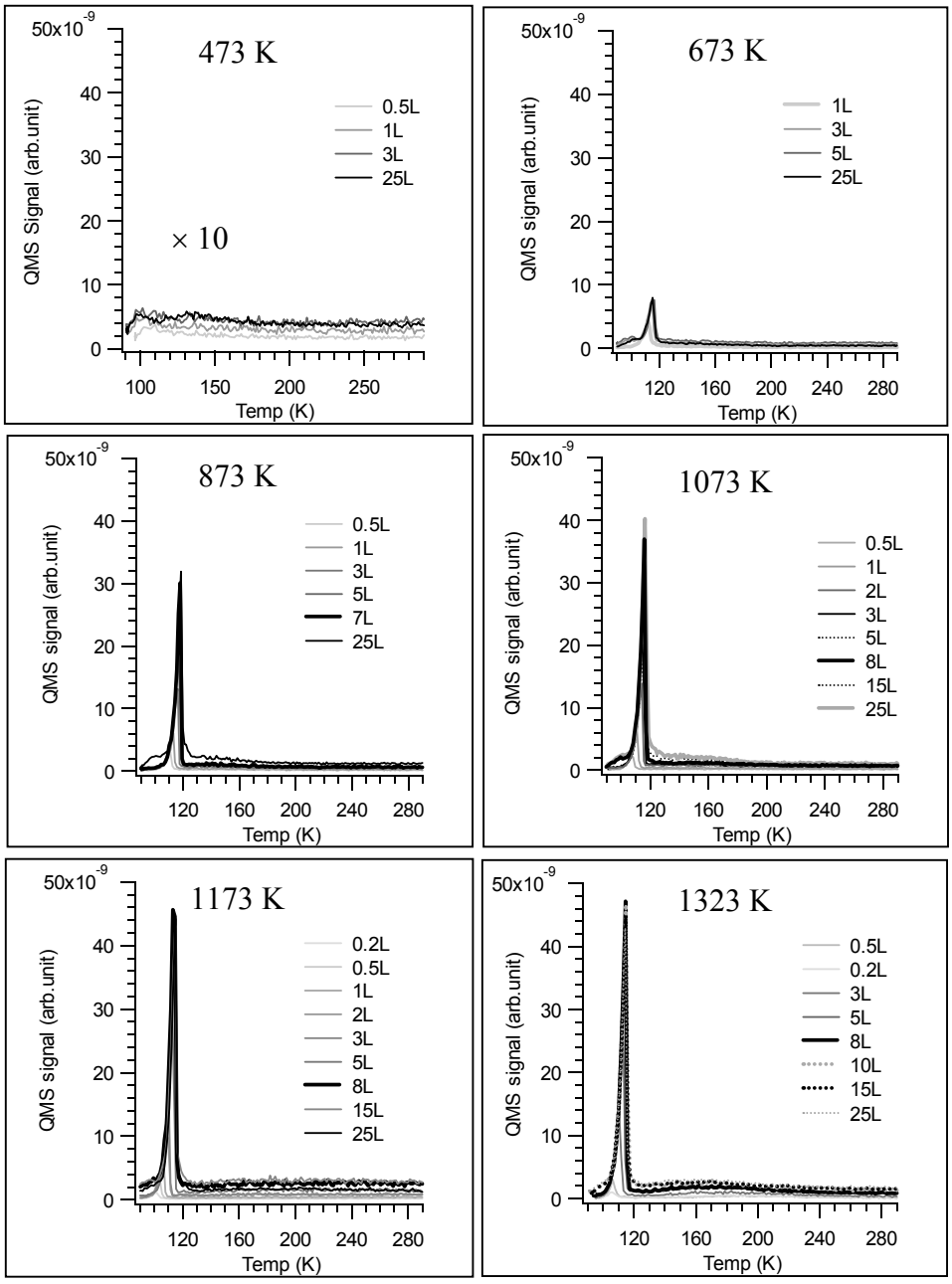

Figure 4-21. TPD spectra at 29 m/e (propane) for air-cleaved HOPG after heat treatment at various temperatures. Note that identical vertical scales are used for all figures. Data for 473 K are multiplied by 10 to aid in viewing.

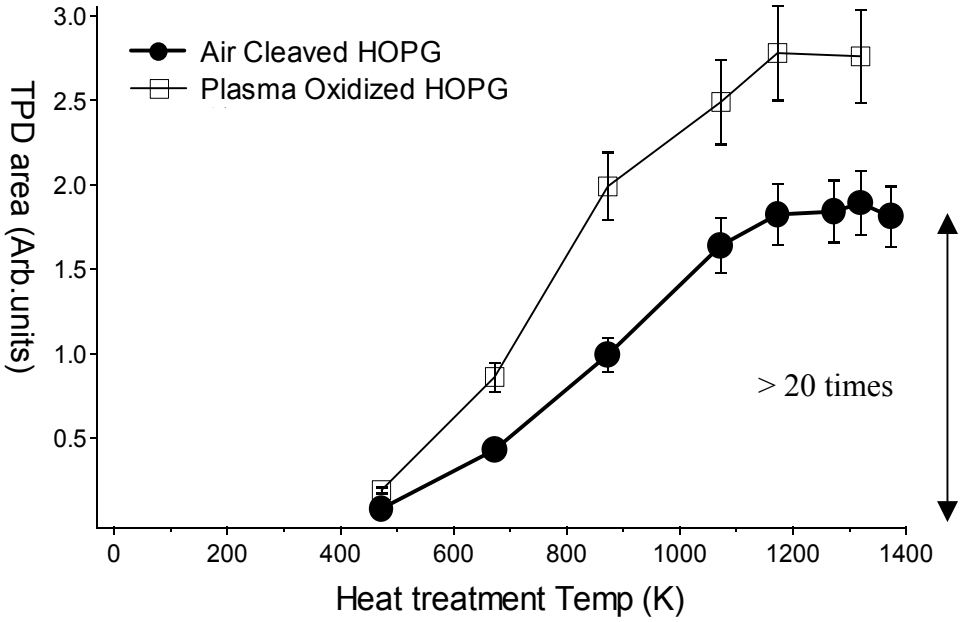

Figure 4-22. TPD areas for propane at 25 L exposure as a function of heat treatment temperature for air-cleaved and plasma-oxidized HOPG.

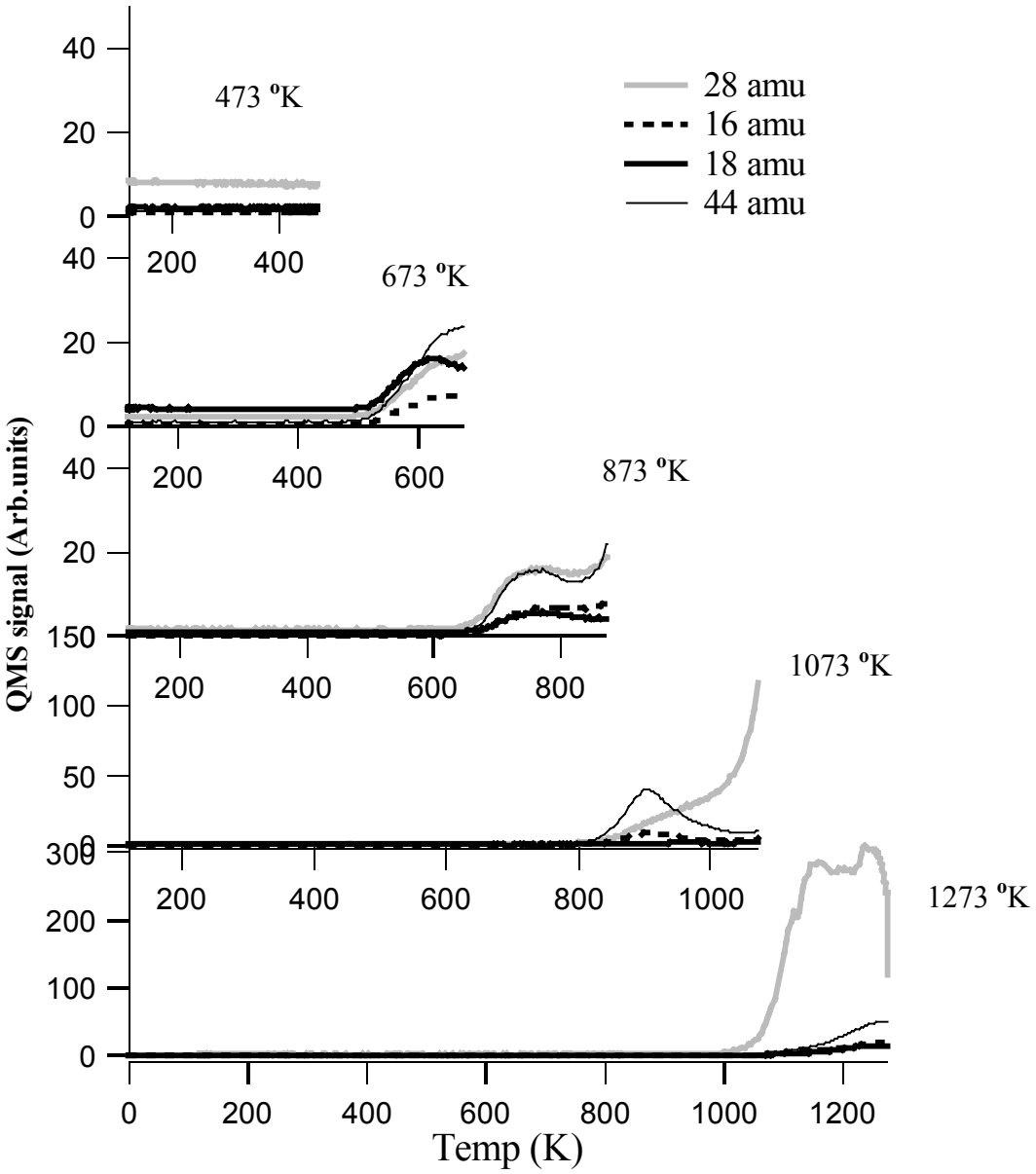

Figure 4-23. Evolution of masses 16, 18, 28 and 44 amu during initial heat treatment of plasma oxidized HOPG to different temperatures. Data for 16, 18 and 44 amu in the 1323 K scan are multiplied by 10 to aid in viewing

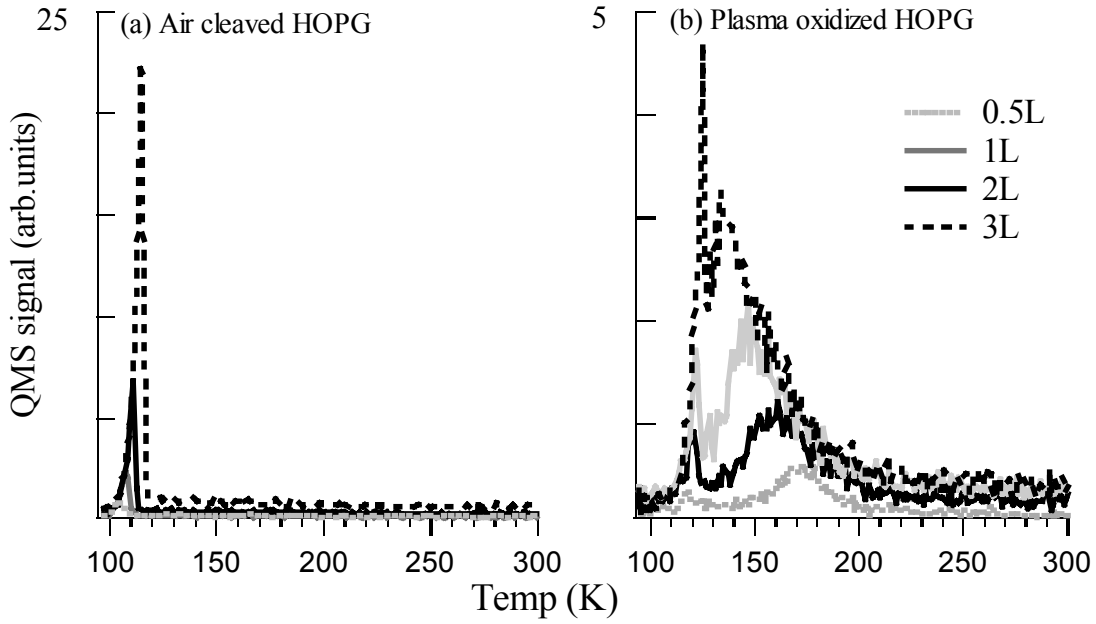

Figure 4-24. TPD spectra for propane after 1173 K heat treatment for (a) air-cleaved HOPG (b) O_2 plasma-oxidized HOPG. The same arbitrary units are used in both figures to facilitate comparison.

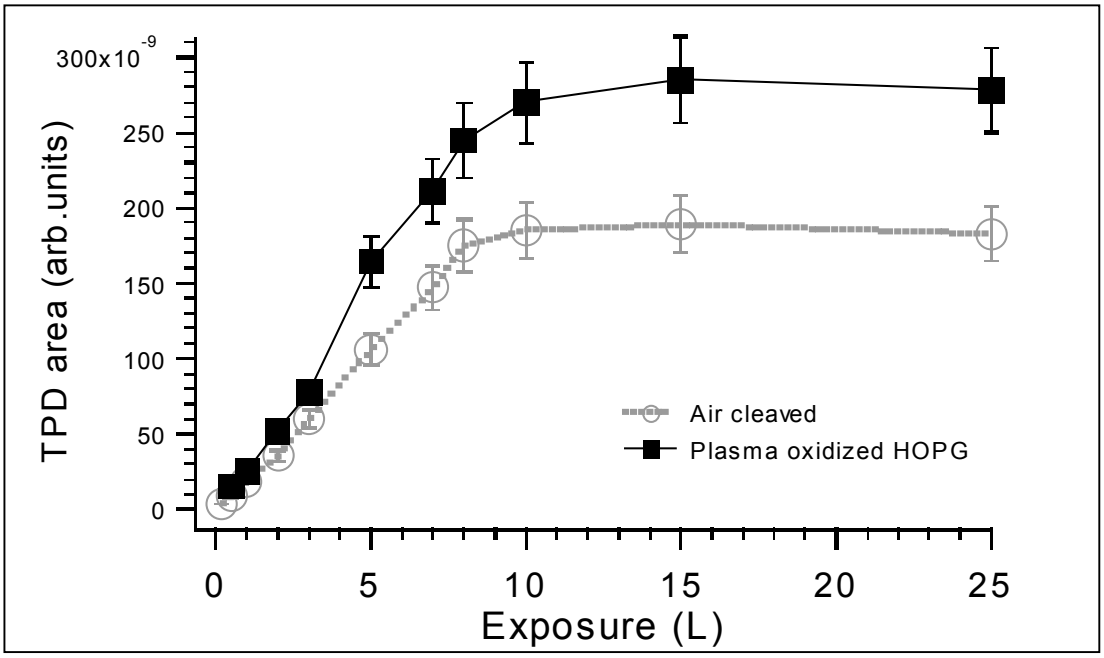

Figure 4-25. TPD area of propane for air-cleaved and plasma-oxidized HOPG after 1173 K heat treatment.

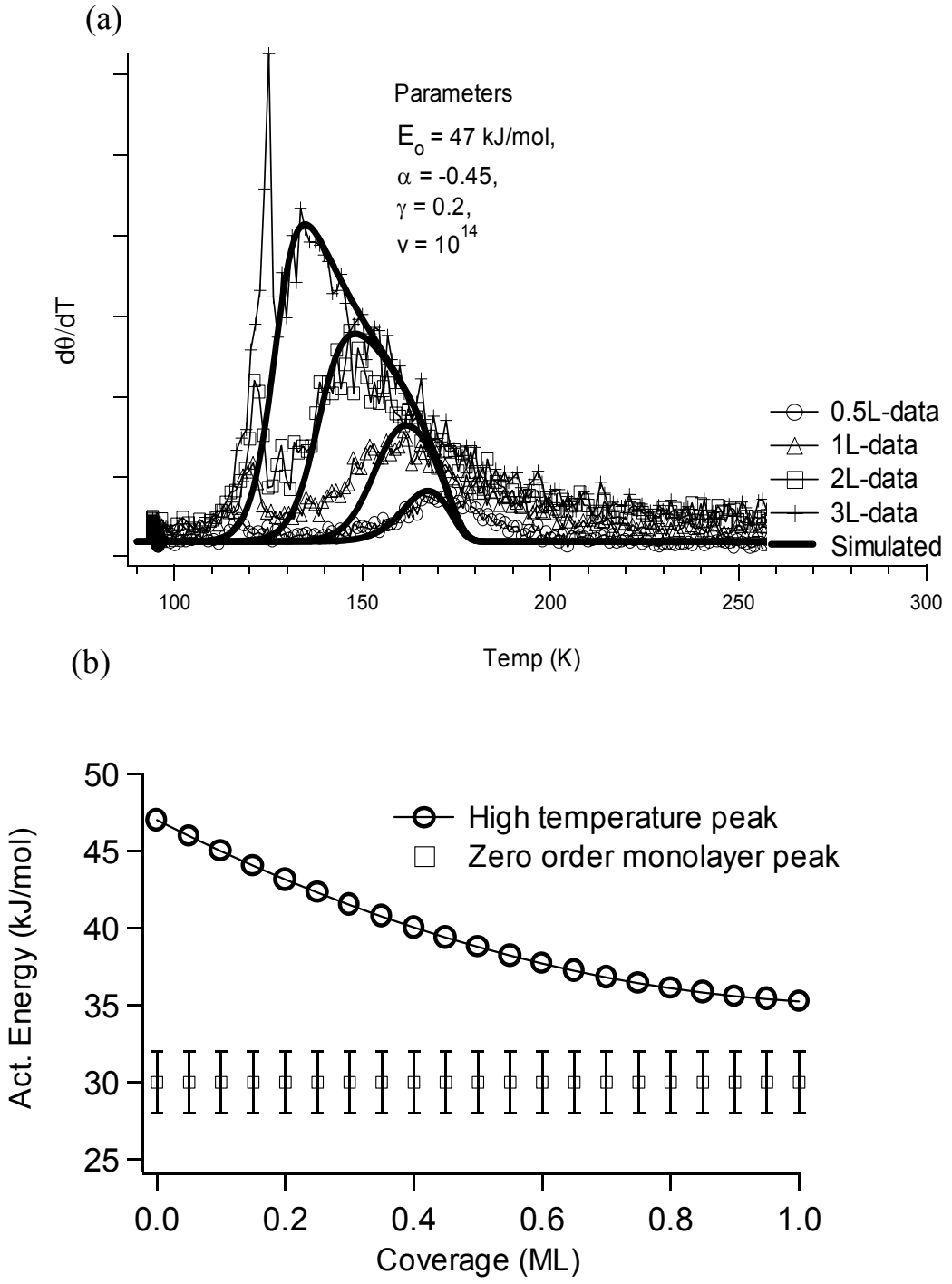

Figure 4-26. Quantitative analysis of high temperature TPD peak of propane from plasma oxidized HOPG. (a) Coverage dependant first order simulation and (b) average heat of adsorption for both low and high temperature peak

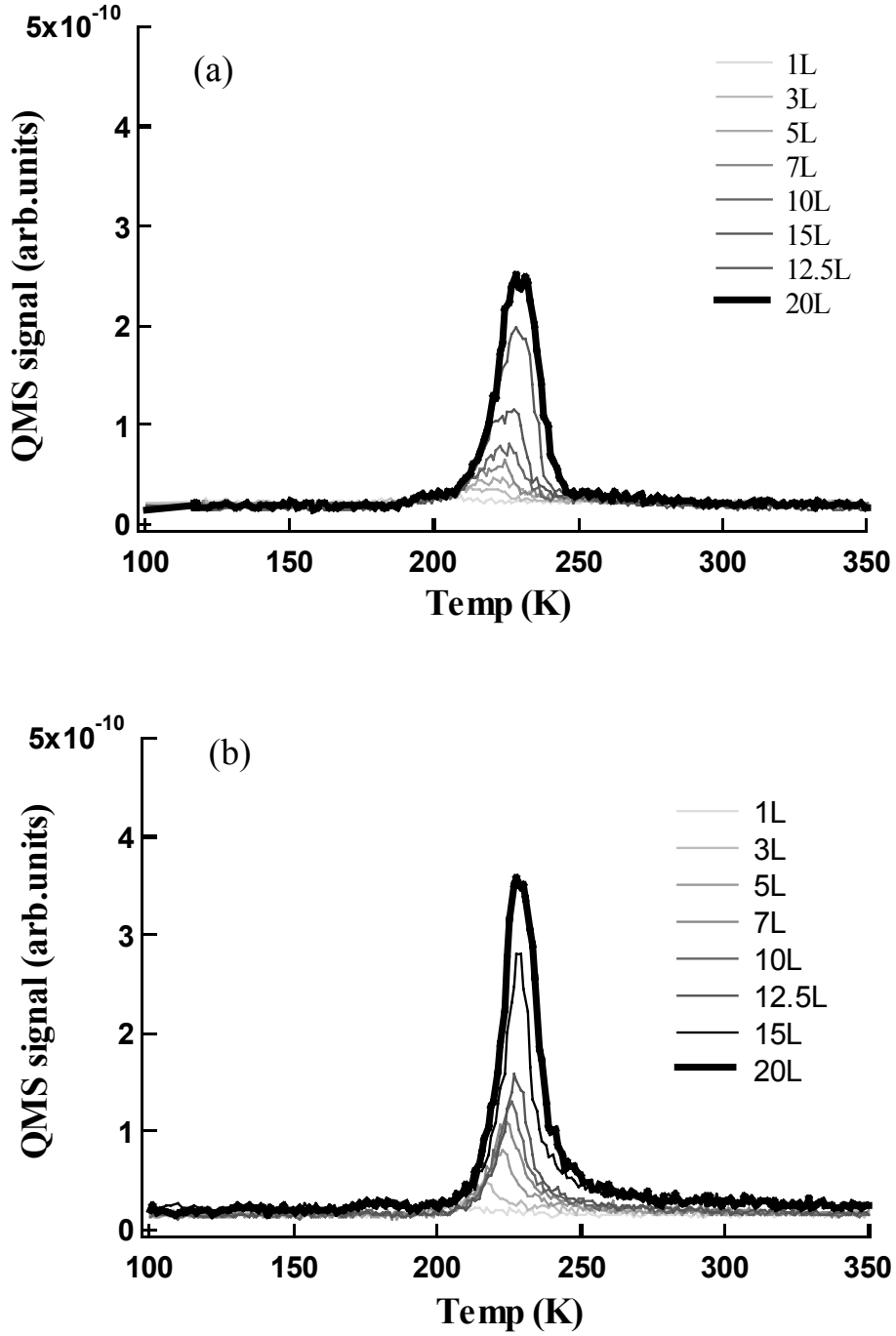

Figure 4-27. TPD spectra of mercury on air cleaved HOPG that was previously heated at (a) 473 K and (b) 1273 K

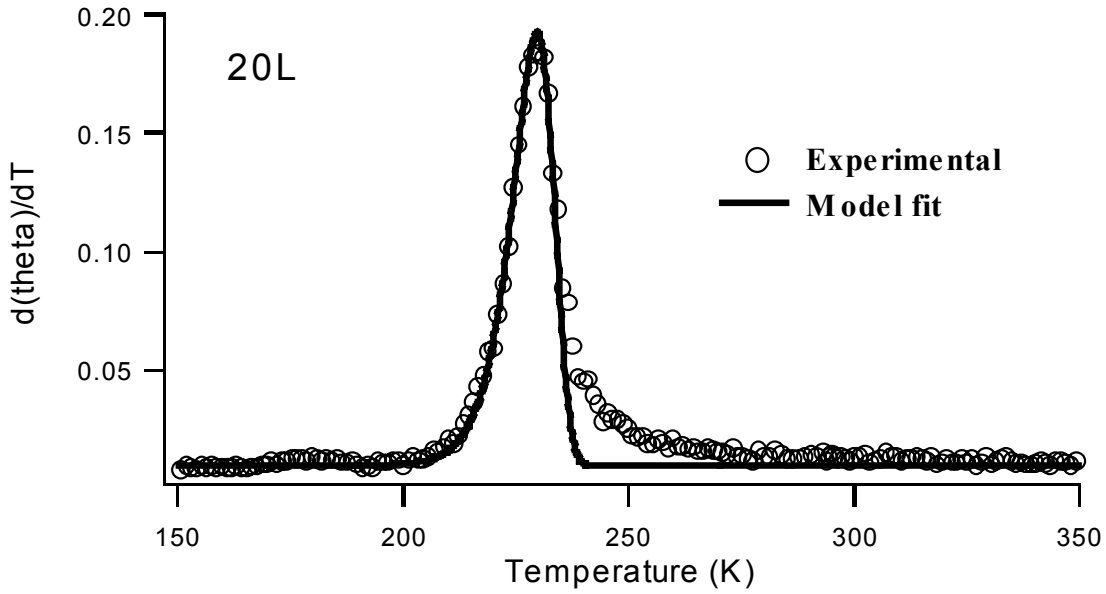

Figure 4-28. Modeling of TPD spectrum of mercury at 20 L exposure using coverage dependent first order desorption kinetics(α=0.003)

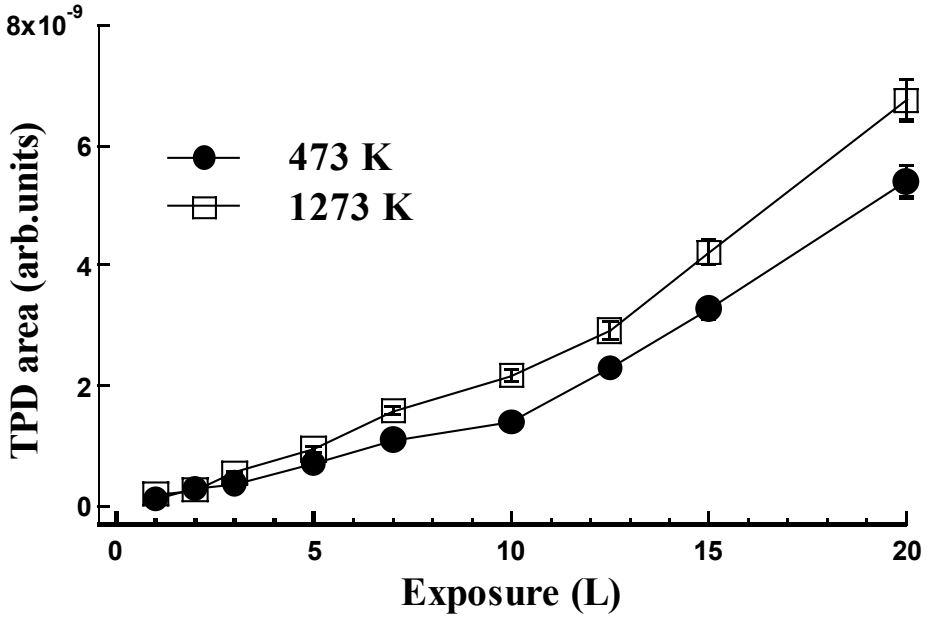

Figure 4-29. TPD area as a function of mercury exposure for air-cleaved HOPG

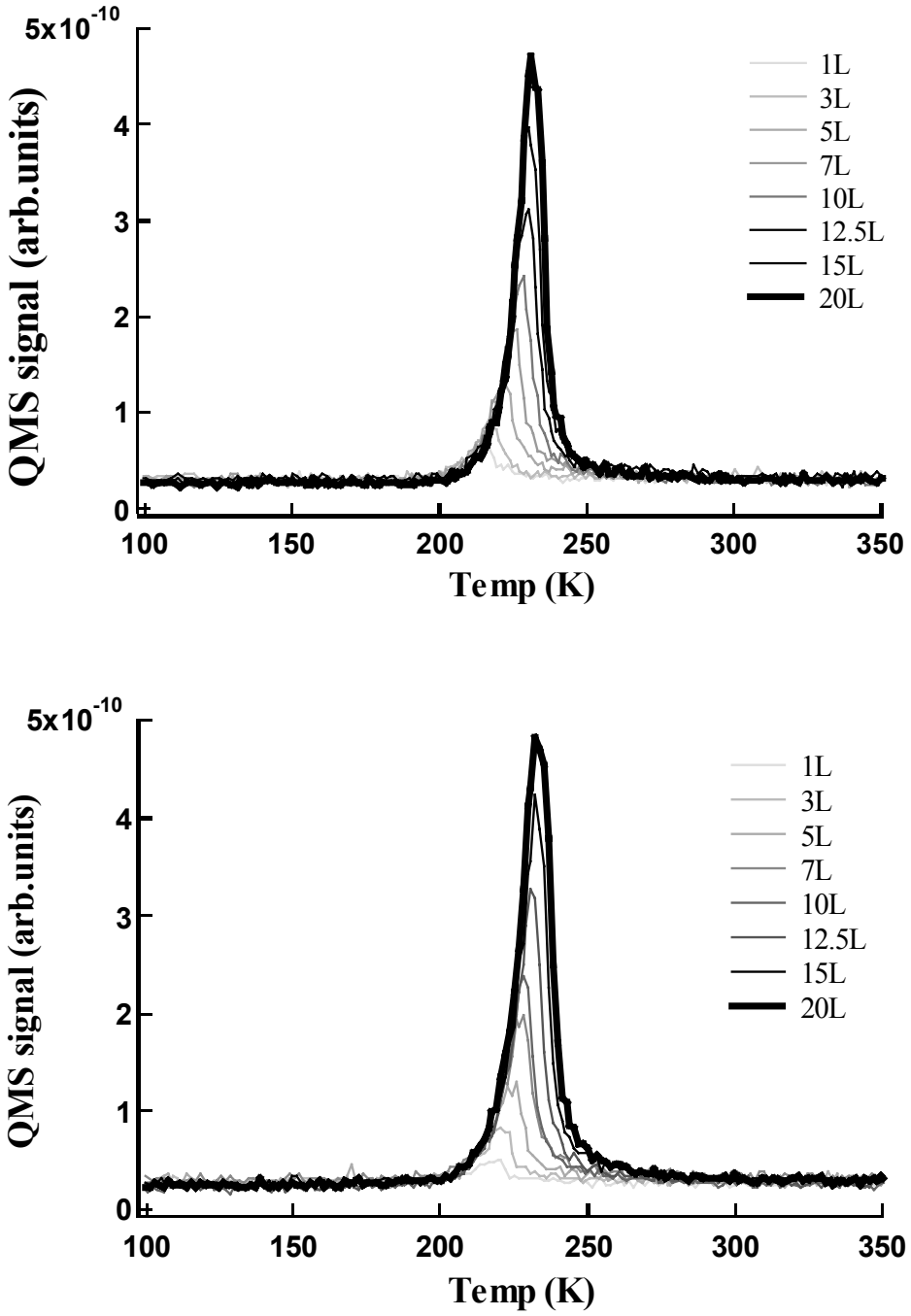

Figure 4-30. TPD spectra of mercury on (a) plasma-oxidized HOPG for 20 min and (b) plasma-oxidized HOPG for 90 min. Note that both HOPG samples were pretreated at 1273 K and that identical scales are used for both figures.

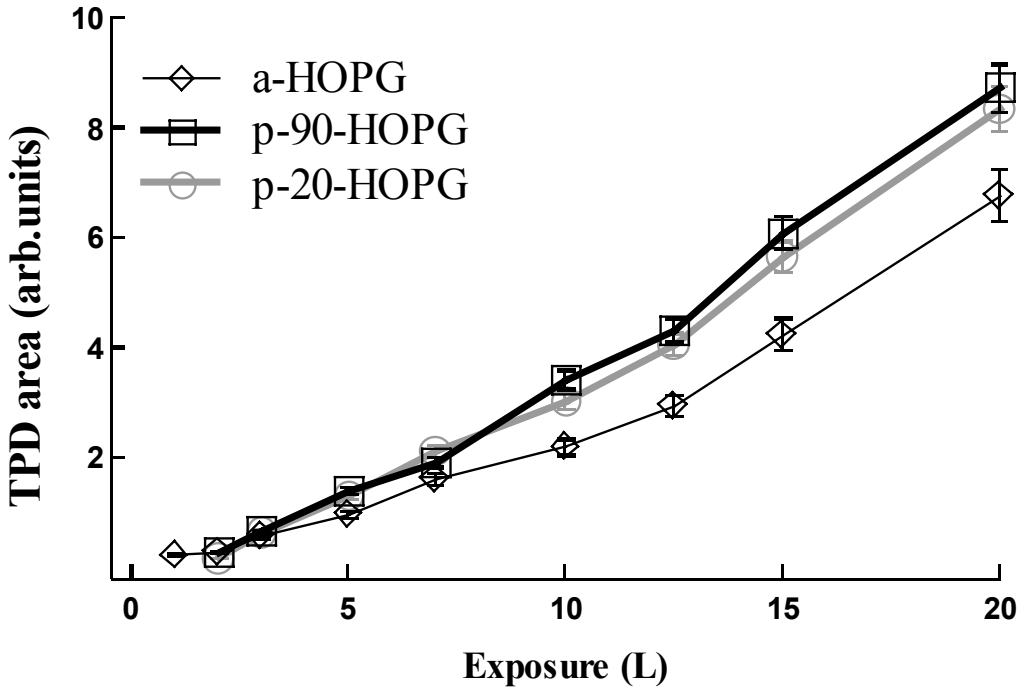

Figure 4-31. TPD area as a function of mercury exposure for air-cleaved and 20 min (p-20-HOPG) and 90 min (p-90-HOPG) sample after 1273 K heat treatment

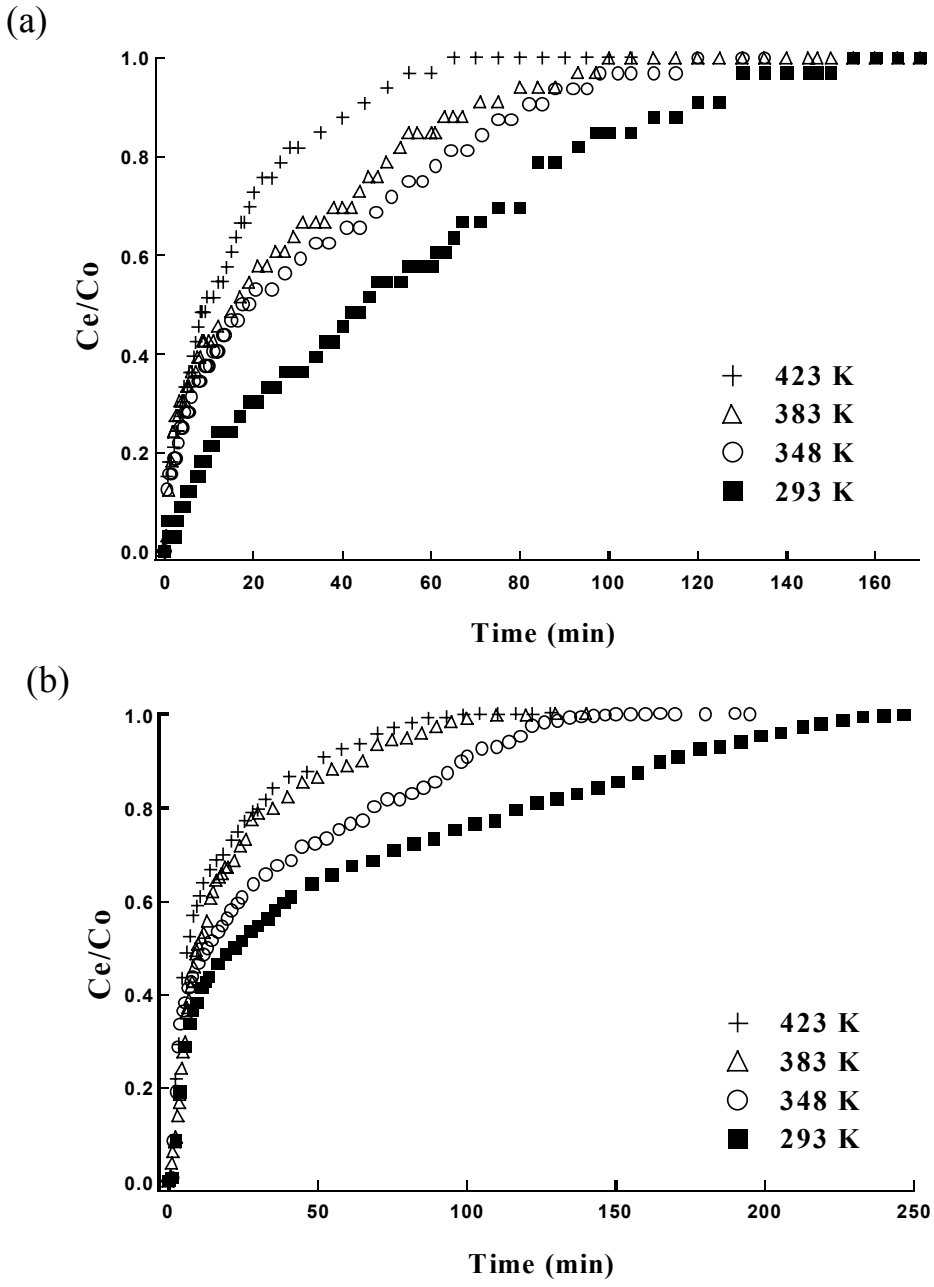

Figure 4-32. Impact of temperature on mercury breakthrough from a fixed bed adsorber at influent mercury concentrations of (a) 70 μg/m^3 and (b) 1120 μg/m^3

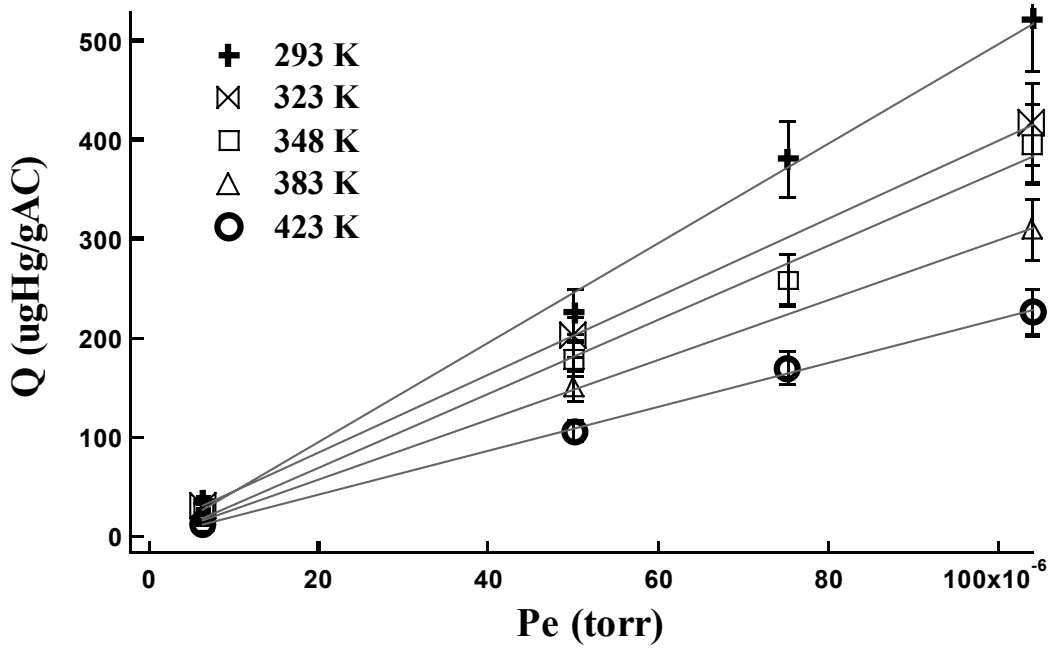

Figure 4-33. Mercury uptake capacity as a function of equilibrium pressure, P_e at different adsorption temperatures (lines represent linear regression fit to experimental data)

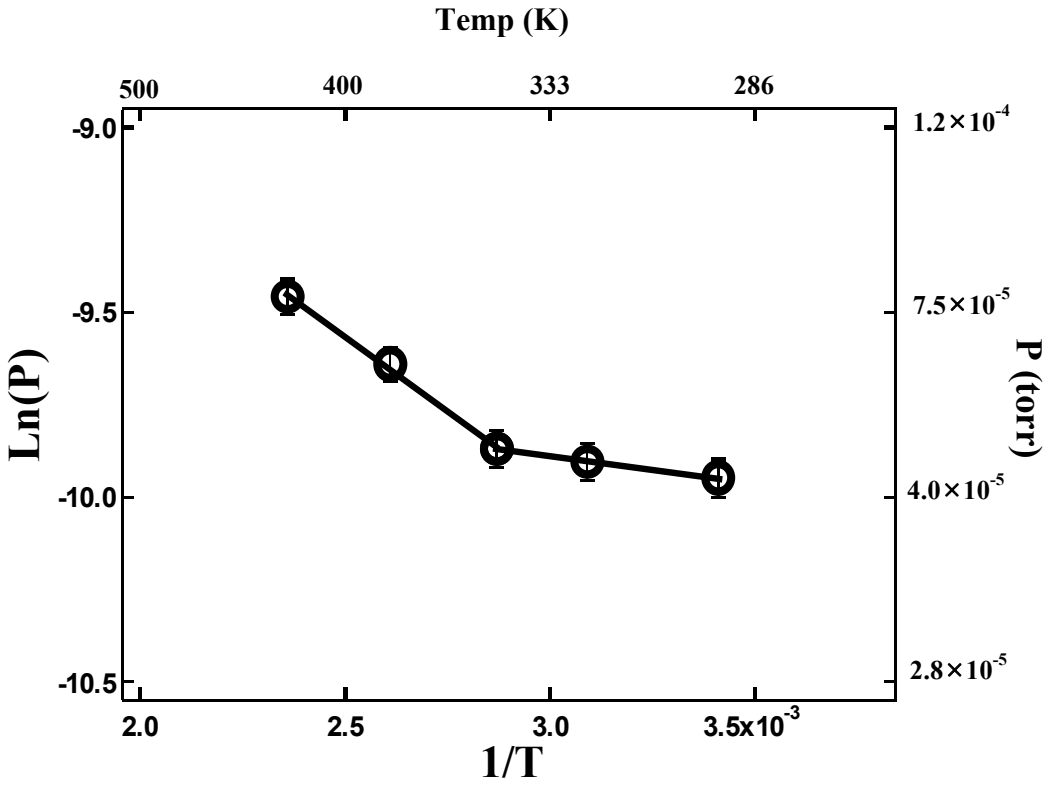

Figure 4-34. Equilibrium pressure at 200 μgHg/gAC as a function of 1/T. Line (a) represents a linear fit to adsorption data collected below 348 K and line (b) is a linear fit to adsorption data collected above 348 K

(a) Adsorption at 293 K

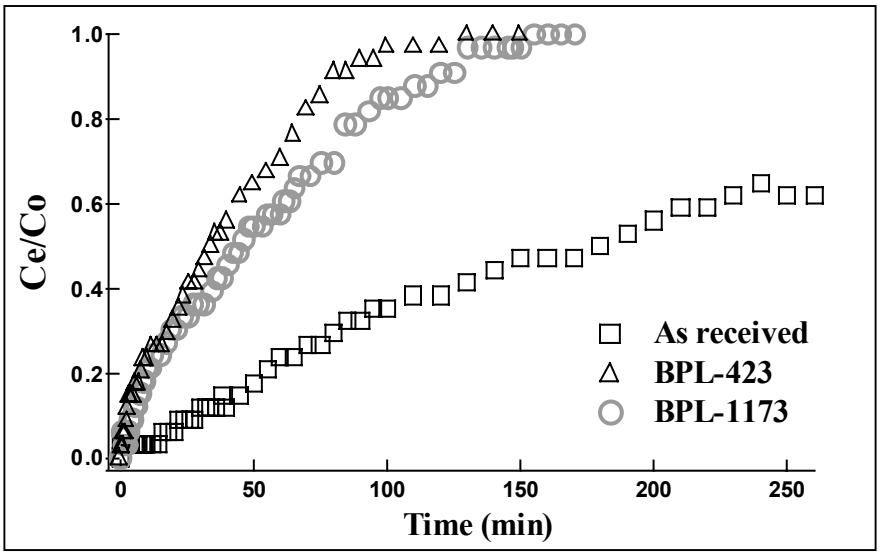

(b) Adsorption at 423 K

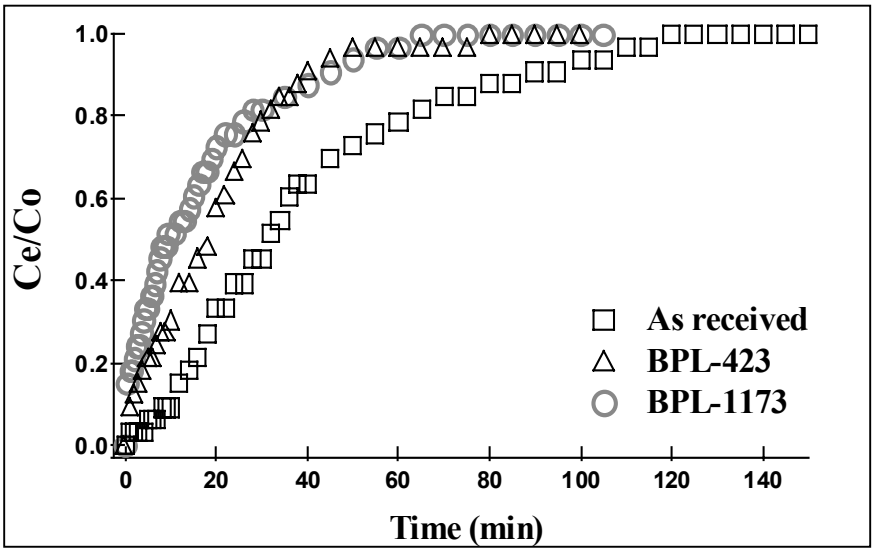

Figure 4-35. Impact of sample pretreatment on elemental mercury breakthrough from a fixed bed adsorber operated at (a) 293 K and (b) 423 K with influent mercury concentration of 70 $\mu g/m^3$